TESIS DE LA UNIVERSIDAD DE ZARAGOZA

2012

87

Jonathan Correa Magdalena

$^{10}B_4C$ Multi-Grid as an alternative to ^{3}He for Large Area Neutron Detectors

Departamento
Física de la Materia Condensada

Director/es
Guerard, Bruno
Campo Ruiz, Jesús Javier

ISSN 2254-7606

Prensas de la Universidad
Universidad Zaragoza

Universidad Zaragoza
1542

Tesis Doctoral

$^{10}B_4C$ MULTI-GRID AS AN ALTERNATIVE TO ^{3}HE FOR LARGE AREA NEUTRON DETECTORS

Autor

Jonathan Correa Magdalena

Director/es

Guerard, Bruno
Campo Ruiz, Jesús Javier

UNIVERSIDAD DE ZARAGOZA

Física de la Materia Condensada

2012

$^{10}B_4C$ Multi-Grid as an Alternative to ^{3}He for Large Area Neutron Detectors

Colección de Estudios de Física
Vol. 31

Esta colección recoge las tesis presentadas en el Departamento de Física de la Materia Condensada de la Universidad de Zaragoza desde su constitución en 1987.

Colección de Estudios de Física Vol. 31

$^{10}B_4C$ Multi-Grid as an Alternative to ^{3}He for Large Area Neutron Detectors.

Jonathan Correa Magdalena

Prensas Universitarias de Zaragoza

A mi familia

Contents

Abbreviations

CoG Centre-of-Gravity

CVD Chemical Vapour Deposition

DAQ Data Acquisition System

ESS European Spallation Source

ERDA Elastic Recoil Detection Analysis

FWHM Full Width Half Maximum

GEM Gas Electron Multiplier

ICND International Collaboration for the development of Neutron Detectors

ILL Institut Laue - Langevin

LAND Large Area Neutron Detector

MC Monte Carlo

MCA Multi-Channel Analyser

MCC Multi-Channel Controller

MWPC Multi-Wire Proportional Chamber

MSGC Micro-Strip Gas Chamber

NSS Neutron Scattering Science

ORNL Oak Ridge National Laboratory

PHS Pulse Height Spectrum

PMMA Poly(Methyl Methacrylate)

PSD Position Sensitive Detector

PMT Photo-Multiplier Tube

PVD Physical Vapour Deposition

RPC Resistive Plate Chamber

ROI Region-of-Interest

SEM Scanning Electron Microscopy

SNS Spallation Neutron Source

ToF Time-of-Flight

ToT Time-over-Threshold

XRR X-Ray Reflectivity

WSF Wavelength-Shifting Fibre

Introduction

The low interaction probability of thermal neutrons with matter together with its relatively low energy (25 meV) make complicated its direct detection. A nuclear reaction is commonly used to create secondary charged particles. ^{3}He is the main neutron converter used. Mainly due to Homeland Security programs in the United States, the accumulated ^{3}He stockpile has dramatically decreased in the last few years. The production no longer meets the demand an a shortage has been produced. The needs of future neutron facilities as for example the European Spallation Source (ESS) together with the instrument suite renovation of present sources such as J-Parc, the Spallation Neutron Source (SNS) and the Institut Laue - Langevin (ILL) will required suitable solutions for Large Area Neutron Detectors (LANDs).

In this context, a study of the causes and consequences of the ^{3}He crisis can be found in Chapter 1. Together with it, the principal requirements for a neutron detector installed in a Time-of-Flight (ToF) instrument are analysed. Three different techniques have been chosen by the scientific community as possible alternatives: BF_3 gas-counters, scintillators coupled to Wavelength-Shifting Fibre (WSF), and boron-lined detectors. The latter one has been adopted for the development of a Position Sensitive Detector (PSD).

Three are the different types of radiation - matter interaction needed to understand the basis of a neutron detector operation: neutrons, charged particles and photons. Firstly, the interaction of neutrons with the converter. Charged particles are subsequently emitted after the neutron capture. For our study, photon - matter interaction is the cause of a major part of the background radiation: the γ-rays. In Chapter 2, the interaction of these three types of radiation is reviewed.

In a gaseous detector, once the neutron capture takes place within the converter, the reaction fragments will start producing ionisation of the gas molecules. This process is followed by charge separation and drift, gas amplification and signal generation. In Chapter 3 these different processes are studied. Together with them the main parameters of gaseous detectors: efficiency, dead

time and operation mode; are examined.

Parameters such as the total number of layers and the individual layer thickness need to be optimised. Others such as the geometry of the detector or the variation on the efficiency as a function of the wavelength of the incoming neutrons need to be studied. The importance of the wall-effect for stopping gas pressures lower than atmospheric is to be analysed. All this is done through a MC simulation which concepts and limitations are explained in Chapter 4.

The Multi-Grid detector concept is explained in Chapter 5. The specifications of the different prototypes used in this study are detailed. The associated electronics needed for the detector to work is presented together with a few ideas about its optimisation.

Requirements of the boron-containing coating are a high concentration in ^{10}B together with a large thickness uniformity over the coated surface. DC magnetron sputtering was the chosen coating technique. It is studied together with the different thin film characterisation techniques. Also neutron techniques such as neutron radiography were used and are studied in Chapter 6.

A complete characterisation of the Multi-Grid prototype was performed as it is presented in Chapter 7. Results on detection efficiency, uniformity, γ-sensitivity, rate capability, ageing and stability, etc; are shown and discussed.

The aim of this thesis is to show the potential of this technique as an alternative to ^{3}He-based PSD for Neutron Scattering Science (NSS) instruments. Relatively high detection efficiency together with large scale production capabilities show its capacity.

Chapter 1

The Problematic

1.1 Introduction

Due to the specific properties of thermal neutrons, to be studied in Chapter 2, their detection generally requires a capture interaction with a neutron absorbing element. Secondary particles emitted during this reaction are used for an indirect detection of the incoming neutron. As it will be seen, the list of potential neutron converters is small. Among them ^{3}He performance has made it the most used converter for neutron detection over the last 30 years.

NSS, as it will be seen in Section 1.2, requires very different types of detection systems adapted to each instrument. The maintenance of these detectors together with the renovation of present instrumentation demands large quantities of neutron converters. In this context, the need of ^{3}He claimed by the different NSS facilities worldwide for the period 2009 - 2015 is presented in Table 1.1.

The present ^{3}He shortage, to be discussed in Section 1.3, makes the construction of new large arrays of PSD impossible. Instruments more affected by the shortage are those covering large active areas (defined as Large Detectors in Table 1.1): powder diffractometers and specially ToF spectrometers. The new ESS, to be built in Sweden, and not yet taken into account in Table 1.1, will require large active areas ≈ 230 m^2.

Three different alternative techniques to ^{3}He have been defined by the scientific community to be developed, evaluated an compared to present detectors: $^{10}BF_3$-filled gas counters, ^{6}Li-ZnS(Ag) and $^{10}B_2O_3$-ZnS(Ag) scintillators coupled to WSFs and ^{10}B-lined gas detectors. These techniques are shortly reviewed in Section 1.4.

Facility	Maintenance	Small Detectors	Large Detectors
ORNL (SNS)	100	1,300	17,100
ORNL (HFIR)	100	1,210	1,060
LANL	100	1,994	12,362
NIST	100	560	-
BNL	100	180	-
FRM II	50	650	4,500
HZB	100	520	7,850
ILL	100	1,000	3,000
JCNS	40	15	7,200
LLB	50	600	600
PSI	50	-	2,000
ISIS	100	400	11,300
J-PARC	100	40	16,100
JRR-3	31	71	-
BNC/KFKI	50	118	500
Total	**1,171**	**8,540**	**83,572**

Table 1.1: Projected demand of ^{3}He for detector in the different neutron scattering facilities in the period 2009-2015 [1].

1.2 Neutron Scattering Science

NSS is a powerful tool that allows to investigate the structure and dynamics of matter. It is complementary to other types of radiation as X-rays, electrons and ions. Reasons for this rely on the peculiarities of thermal neutrons. They are electrically neutral and have low kinetic energy ($\sim$ 25 meV). As a consequence, neutrons can deeply penetrate into matter. Precise information on the magnetic behaviour of materials at atomic level can be collected. Diffusive motion in solids and liquids can be studied. Stresses in materials can be investigated, etc.

Matter is studied through the analysis of the scattering vector $Q = k - k'$, seen in Figure 1.1. k and k' are the wave-vectors of the neutrons before and after the interaction with the atoms that make up the sample. Detectors measure the intensity of the scattered neutrons, I (2θ), as a function of the scattering angle. Information on the momentum transfer, $\hbar Q$, during the interaction is measured. Different techniques are used according to the type of sample and the information to be obtained.

In some cases, energy information can be acquired. A particular case is the ToF spectrometer. The energy transferred during the interaction, $\hbar\omega \propto \mathrm{k}^2$ -

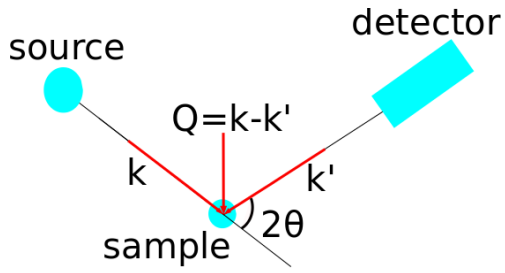

Figure 1.1: Scheme of a NSS experiment. Q is defined as a function of the wave-vectors k and k'.

k'^{2}, or in terms of the neutron velocity $\propto$ v^2 - v'^{2}. The energy transfer can be then accessed by measuring the delay, Δt, between the arrival of the inelastic scattered neutrons compare to the elastic ones. The complete scattering function S (Q, ω) is then obtained through a transformation from the neutron intensity function, I (2θ, Δt).

1.2.1 Detector Requirements

Specifications of a neutron detector vary as a function of the type of instrument and the neutron source which feeds it.

ToF instruments normally require actives areas of tens of square meters. Typical values for the spatial resolution are in the order of 2 cm $\times$ 2 cm. The most important ToF instruments are *AMATERAS* at J-Parc, *CNCS* at SNS, *LET* at ISIS, *TOF-TOF* at FRM II, *NEAT* at HZB and *IN5* at ILL. All of them have similar requirements and shown comparable capacities. IN5 has been chosen as a model for this study.

With an increasing brightness and time structured pulses, new spallation sources are becoming an important part of NSS. Some particularities of these facilities compared to reactor-based ones need to be taken into account for the detector optimisation.

Cold Neutron Spectrometer - IN5

IN5 is a high precision direct geometry ToF spectrometer. It is used to study low-energy transfer processes as a function of the momentum transfer [2]. Typical conditions of measurements are about 1% for the energy resolution (e.g. quasi-elastic scattering in solids, liquids, molecular crystals and inelastic scattering with small energy transfers in the range 10 μeV - 100 meV).

An incoming neutron will lose or gain energy in its interaction with the

atoms of the sample. This energy transfer – although small – can be measured. Neutron energy is related with its velocity and thus with time. Energy information is extracted from the time delay $\Delta t = t - t_0$, of the inelastic scattered neutrons compare to the elastic ones (no energy transferred). Neutron velocities for a wavelength of 1 Å are $\approx$ 1 km/s. For a typical ToF instrument Δt becomes then $\approx$ 10 μs. Initial time t_0, is given by a chopper system shown at the IN5 layout in Figure 1.2. This device allows the energy transfer measurement but decreases the flux.

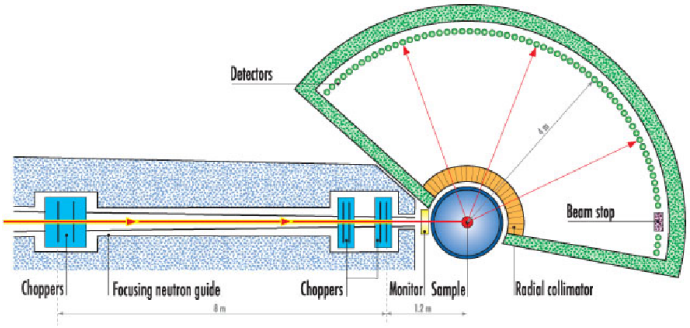

Figure 1.2: Layout of the IN5 instrument. The flight path of the neutron from the sample-position to the detector is 4 meters long. An active area of 30 m^2 is covered in this instrument.

The slit width of the chopper system is the main contribution to the time, and hence energy, uncertainty. To minimise this factor, longer flight times are needed. A large sample-position detector distance is then required. In the case of IN5, this distance is set in 4 meters. This fact, together with a broad angular coverage, explains the large active area required for ToF detectors.

In order to minimise the interaction of scattered neutrons before they reach the PSDs, they are placed in a vacuum chamber. The pressure difference that the detector tubes need to maintain is therefore increased. Thicker walls are needed which implies a higher interaction probability of the neutron within the materials used (stainless-steel in the case of IN5). Lower detection efficiency and higher background are the consequences.

As a part of the ILL Millennium Programme several major improvements were performed in the instrument. These renovations included the complete substitution of the old ^{3}He counters for a new PSDs [2].

As it is shown in Figure 1.3, the ^{3}He-based PSD is located at the back of a 85 m^3 chamber. The made in-house detector by the ILL Detector Group covers a surface 6 times larger than the previous one keeping efficiency (80 % @ 5 Å) in similar values [3].

Figure 1.3: The IN5 PSD can be seen at the back of the 85 m^3 vacuum chamber. It consists in 384 – 3 meters high – ^{3}He tubes.

The PSD is formed by 12 modules each containing 32 cylindrical tubes. Tubes are filled with a ^{3}He-CF_4 mixture (4.75 + 1.25 bar respectively). The centres of the cylindrical tubes are 2.5 cm apart. Such a dense packing allows to significantly reduce the dead zones in the detector (2.5 cm between each module). This arrangement yields a total active surface of 30 m^2. The angular range goes from -12° to +135°.

Localisation is done as follows. One dimension is obtained from the fired tube. The other dimension is measured with a charge division system, to be studied in Section 5.4.2, which gives the position of interaction along the tube length. The obtained pixel size is 2.5 cm × 2.5 cm.

A 10 cm of polyethylene shielding envelope together with a 5 mm B_4C absorber liner gets a flat and homogeneous background with a signal-to-noise ratio of 10^4 for a standard test[1].

A summary of the new IN5 PSD specifications can be found in Table 1.2.

The main requirements for the detector of a ToF neutron spectrometer can be condensed into the three reviewed now:

- To properly match the energy uncertainty produced by the chopper system, long flight paths – several meters long – are needed. This, together

[1] Elastic scattering from a 1 mm thick vanadium sample.

Characteristic	Value
Detector Geometry	Cylindrical Tubes
Sensitive Area [m^2]	30
Flight Path [m]	4
Detection Height [m]	3
Scattering Angular Range	-12° to 135°
Vertical Angular Range	± 20.55°
Solid Angle Covered [sr]	1.8 (0.6 π)
Momentum Transfer Range [$Å^{-1}$]	$0.2/\lambda$ - $11.8/\lambda$
Spatial Resolution [cm^2]	2.5 × 2.5
Angular Resolution	0.37°
Gas Mixture [bars]	4.75 ^3He + 1.25 CF_4
^3He Volume [litres]	3000
Detector Efficiency [%]	≈ 80 @ 5 Å
Dead Time / Tube [μs]	≤ 10
Signal to Noise Ratio	10000/1

Table 1.2: Some of the most important characteristics of the new PSD installed at IN5.

with a broad angular range leads to large active areas: tens of square meters. Spatial resolution required is in the order of 2 cm × 2 cm for both dimensions.

- Detection efficiencies in the same range that ^{3}He-based detectors ($\sim 80\%$ @ $\lambda = 5$ Å) are demanded. A high uniformity of this parameter over the total active area of the detector is required.

- High signal-to-noise ratio. γ-contamination and neutron background are the two main sources of noise. They need to be fully understood and minimised.

1.2.2 Reactor versus Spallation Source

Steady-state neutron sources are based on a fission reaction [4]. The schematic process is shown in Figure 1.4. During this reaction an average of 2.5 neutrons is generated. Some of these neutrons maintain the process ongoing in a chain reaction. The rest of them are thermalised and guided to the different instruments used for NSS. The most important facility is the ILL in Grenoble, where a constant flux of $1.3 \cdot 10^{15}$ cm^{-2} s^{-1} neutrons is produced. Also important are the FRM II in Munich ($8 \cdot 10^{14}$ cm^{-2} s^{-1}) and the HZB in Berlin ($1.2 \cdot 10^{14}$ cm^{-2} s^{-1}) among some others.

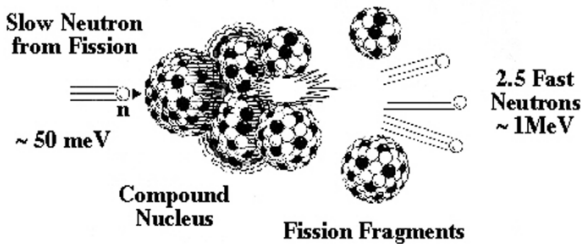

Figure 1.4: Diagram of the fission process used at steady-state sources for neutron production. A heavy nucleus, usually ^{235}U, is fissioned through the collision of slow neutrons [4].

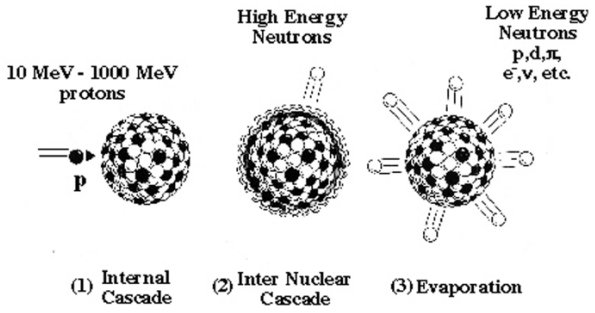

Figure 1.5: Scheme of spallation process for neutron production. A linear accelerator is used to increase the kinetic energy of charged particles which impinge the target formed by heavy nuclei. After the reaction these nuclei become unstable and start emitting different types of particles. [4]

Yet there is a different process to produce neutrons: the spallation. High-energetic particles (e.g. protons) hit a target made of a neutron-rich element. Heavy nuclei reach a highly excited state and start the emission of different fragments including neutrons with a broad energy spectrum. After this, the process is similar to what was seen before for reactor-based sources. A spallation reaction diagram can be seen in Figure 1.5. This process is rather fast ($\sim 10^{-15}$ s), thus the time distribution of spallation neutrons is mainly determined by the time distribution of the driving particle pulse, generally provided by a linear accelerator.

Pulses can go from short ($\approx 10\ \mu$s) to long (a few ms) lengths [5]. ISIS in UK together with J-PARC in Japan and the SNS in the US are the main spallation neutrons sources at present. They are all considered short-pulses sources. With a pulse length of 2.86 ms, and a rate at the peak of the distribution ≈ 30 times higher than at the ILL, the ESS, to be built in Lund (Sweden), will significantly increase the neutron flux available today [6]. Pulse shape and period are shown for several spallation facilities and compared to the ILL in Figure 1.6. For a ToF instrument however, the presence of a chopper system will limit the flux at the sampe position and thus over the active area of the detector.

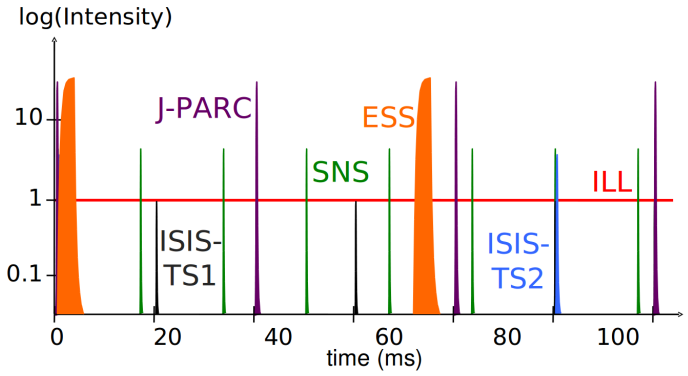

Figure 1.6: Pulse shape and period for several neutron spallation sources. Intensities are compared to the ILL reactor. ESS will be the first long pulse source with 2.86 ms [6].

Together with its brightness, one of the major advantages of spallation sources is the pulsed shape of the neutron flux. It will be used to extract ToF information in all the instrument suite. As seen above, the energy resolution of a ToF instrument is related with the time uncertainty. One of the contributions to this uncertainty, although not the most important, is the time resolution of the detectors. Thinner tubes would help matching this incertitude increasing the energy resolution.

A shorter spectrum in wavelength is expected at the ESS. As it will be

shown in Section 2.2.1, this implies a lower detection efficiency for the most common used converters.

The latest estimation on the required detector active area at ESS is ≈ 230 m^2 (most of it belonging to large detector arrays) [6]. As it will be studied in Section 1.3, with the present availability of ^{3}He the necessary amount of this converter to instrument such a large area ($\geq$ 20,000 litres) will not make possible the construction of the ESS.

1.3 ^{3}He Crisis

^{3}He is a rare isotope of helium with applications in Homeland Security, medicine, industry, and NSS [7, 8, 9, 10]. The main source of ^{3}He on Earth is the decay of tritium, shown in Equation 1.1, which has an average half-life of $\tau = 12.32$ years. Tritium was used to produce nuclear warheads in the United States and Russia until these programs were stopped after the Cold War. For many years the supply of ^{3}He exceeded the demand and a substantial stockpile, shown in Figure 1.7, was accumulated.

$$^3H \longrightarrow {}^3He + e^- + \overline{\nu}. \tag{1.1}$$

The dramatically drop of the stockpile which causes the present shortage is mainly due to two reasons. On one hand the deployment of ^{3}He detectors in the US borders in order to prevent the entry of radiological materials (e.g. plutonium) to be used for terrorism. On the other hand, tens of thousands of litres are being used in large science facilities in the US such as the Oak Ridge National Laboratory (ORNL). An allocation of only 8000 litres per year has been announced until 2015 giving priority to applications without alternative to ^{3}He. This value is to be compared with the needs of the different NSS facilities shown in Table 1.1.

To compare the capabilities of the different alternative techniques chosen by the scientific community are studied now. They are evaluated and compared to the state-of-the-art detector: the ^{3}He tube, which performance is also reviewed.

1.3.1 The ^{3}He-Counter

Widely used for thermal neutron detection, the ^{3}He-counter is based on the capture reaction shown in Table 2.2. The efficiency of a ^{3}He-counter is a function of the factor χ [11]:

$$\chi = P \times d \times \lambda, \tag{1.2}$$

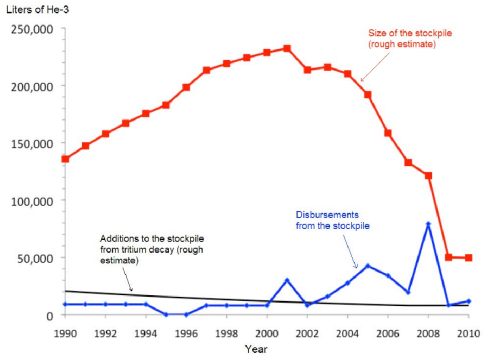

Figure 1.7: The ^{3}He stockpile in the US from 1990 to 2010. Since 2004 the ^{3}He production can no longer meet the demand. This situation provokes the present shortage [7].

where P is the gas pressure [atm], d is the tube diameter [cm] and λ the neutron wavelength [Å]. For a fix λ, higher pressures or thicker tubes are needed to reach higher detection efficiencies. However, as it was said above, thicker tubes will decrease the time resolution of the detector and hence the energy resolution of the instrument. With respect to the pressure, it can go from 0.25 to 15 bar depending on the required efficiency.

A typical PHS is shown in Figure 1.8. The full-energy peak is clearly visible at 764 keV. This value corresponds to the total energy of the neutron capture of ^{3}He to be studied in Table 2.2. When one of the two particles (proton or tritium) reaches the wall of the tube, a part of its energy is not deposit in the gas: this is the wall-effect, further discussed in Section 3.4.2. Lower energy events are accounted giving rise to the distribution shown in Figure 1.8. To decrease th is effect thicker tubes or higher pressures can be used. As it will be seen in Section 3.2.2, a heavier gas is often added to ^{3}He to increase its stopping power.

As it will be discussed in Chapter 2, γ-ray events show a relatively low pulse amplitude. This fact explains the valley found at $\sim$ 100 keV in Figure 1.8 which is often used for γ-discrimination. An energy threshold can be set at the lowest point of the valley to separate neutron events from γ-rays. Low values of γ-sensitivity ($\approx 10^{-7}$) are usually reached with ^{3}He-counters.

1.4 Alternative Neutron Detector Technologies

The development of alternatives for neutron detection has become a priority for all NSS facilities. The scientific community, organised through the Inter-

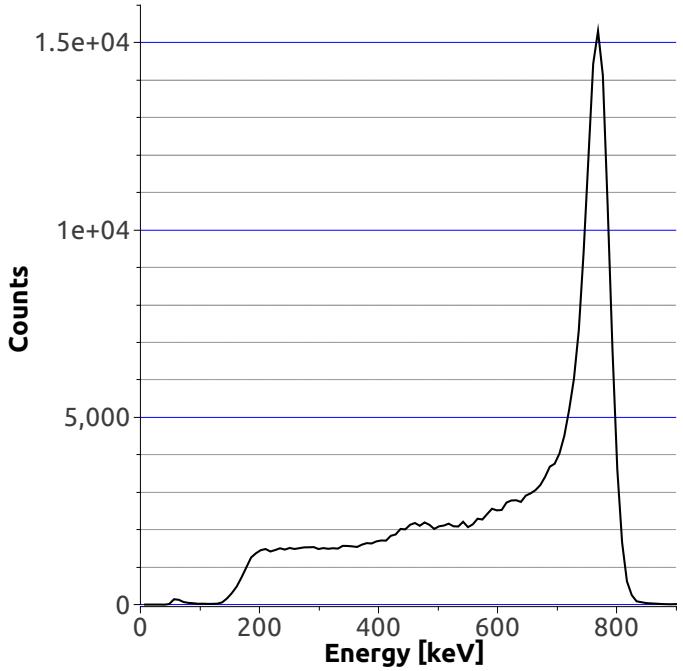

Figure 1.8: A typical PHS of a ^{3}He counter. The full-peak energy is found at 764 keV.

national Collaboration for the development of Neutron Detectors (ICND), has pointed out the three more suitable techniques to replace ^{3}He for LANDs.

1.4.1 $^{10}BF_3$

Already used in the past, the gas proportional counter filled with $^{10}BF_3$ is the best known of the different alternatives that have been proposed. Many obstacles however remain unsolved. As it will be seen in Chapter 2, ^{10}B capture cross section is 72% of ^{3}He. In order to be competitive with ^{3}He detectors either the pressure or the tube diameter has to be increased.

If a thicker tube is used, the time uncertainty of the detector will increase reducing the ToF resolution. Designs using several tubes in depth are being considered to increase the detection efficiency without affecting the ToF resolution [12]. A higher background is therefore expected.

Due to the electro-negativity phenomenon, to be further discussed in Section 3.2.2, if the pressure is raised further than 2 bar, higher applied voltage is needed to compensate the lower pulse amplitude collected.

In Figure 1.9 a comparison between the main gaseous converters used in

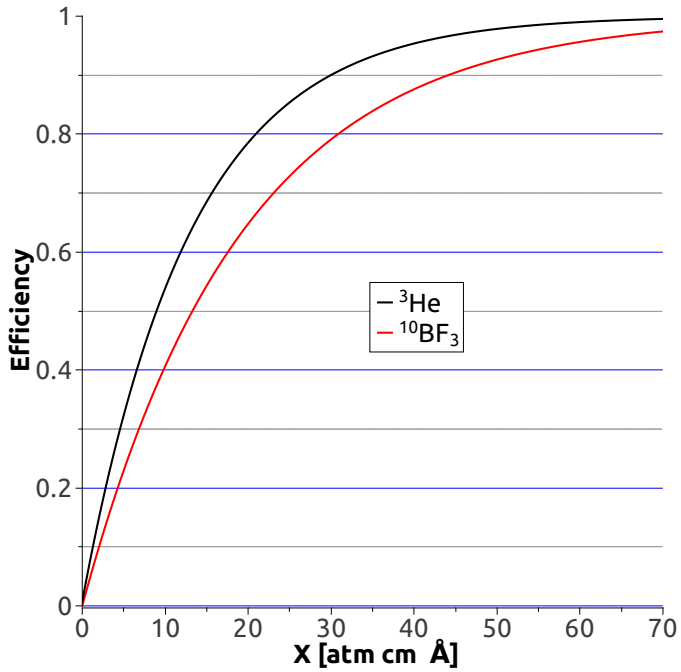

Figure 1.9: Capture efficiency as a function of χ is shown for both ^{3}He and $^{10}BF_3$.

neutron detection as a function of χ is done. Due to its higher capture probability, ^{3}He shows a higher efficiency than $^{10}BF_3$. For ^{3}He, a $\chi = 30$ is needed to reach a 90% detection efficiency. In the case of $^{10}BF_3$ a $\chi = 44.2$ is required.

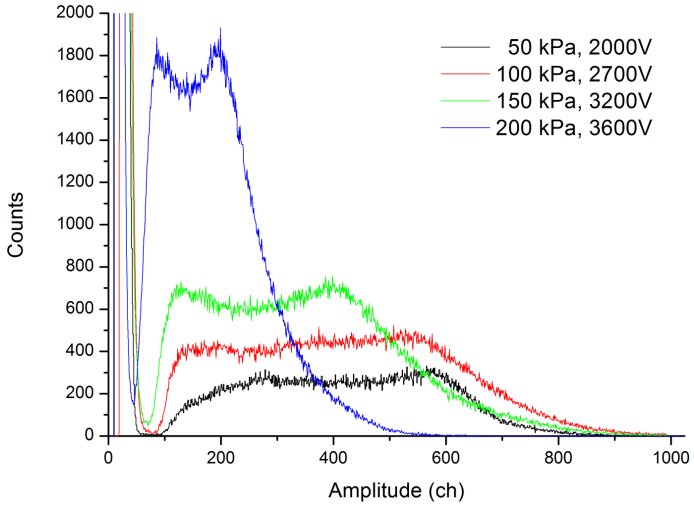

Figure 1.10: PHSs of a $^{10}BF_3$ detector for different gas pressures [12].

Typical BF_3 PHSs are shown in Figure 1.10 as a function of the gas pres-

sure. For this experiment an IN5 tube filled with $^{10}BF_3$ was used. Different pressures were tested. For each value a different applied voltage was needed in order to reach the operational region. In all cases, as for the ^{3}He counter, a valley was found. Due to the higher energy of the reaction fragments a higher γ-discrimination than ^{3}He can be achieved by applying a constant energy threshold.

A dependence with the gas pressure can be seen in Figure 1.10. Different applied voltages were used for the different pressures. For 1.5 and 2 bar higher voltages are needed to have comparable amplitudes. As expected higher efficiency is achieved with higher pressure but a degradation of the PHS is also observed. This phenomena is due to the electro-negativity properties, to be discussed in Section 3.2.2, of BF_3.

BF_3 is extremely toxic and corrosive reasons why its storage and use need to be strictly controlled. This is among all, the main difficulty to overcome with this technique.

1.4.2 Scintillators

A scintillator is a material in which an incident radiation excites a number of electrons to higher energy states. As a consequence, the emission of a light flash of photons in the ultraviolet or visible range is produced.

The ICND has defined ZnS as the scintillator to be used for mainly two reason. On one hand its brightness: each converted neutron is followed by an emission of $\approx 1.5{\cdot}10^5$ photons. On the other hand, the possibility to implement pulse shape analysis to discriminate incoming neutron from γ-events. Other scintillator materials however are being studied and show interesting capabilities [].

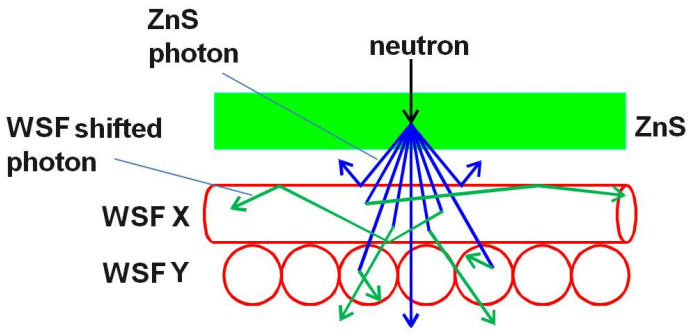

Figure 1.11: A scheme of a neutron PSD using a scintillator as converter and readout with WSFs coupled to PMTs.

ZnS can be doped with two different elements which act as neutron converters: lithium or boron. Typical choices are: $^{10}B_2O_3$-ZnS(Ag) and ^{6}LiF-ZnS(Ag) [13]. Although commercially available, ^{6}LiF-ZnS(Ag) has two main drawbacks to be considered. Firstly, the opaqueness to its own light limits the thickness of material to be used which reduces the detection efficiency. These thin layers however can be an advantage from the time resolution point of view. Also important is the relatively long afterglow ($\approx$ 100 μs) which limits the counting rate capability of the detector [13]. $^{10}B_2O_3$-ZnS(Ag), developed at the J-Parc, shows interesting performances. Specially, relatively high values of detection efficiency (40% @ 1.6 Å) have been reported [14].

WSFs coupled with PMTs are used to readout the scintillator. The main difference between WSF and clear fibres is that, due its light absorption and emission properties, the side of the WSFs can be used as light collector. The light is then tramistted down the leng of the fibre. As it is shown in Figure 1.11, large areas can be covered with a relative low number of WSFs.

Two different solutions can be adopted to couple WSFs to PMTs. On one hand, to increase the rate capability of the detector each WSF is coupled with a single pixel of a PMT. The number of misled events is reduced at the price of increasing the number of PMTs. On the other hand, each PMT pixel can read out more than one WSF. Although a higher probability of misleading and lower rate capability, the number of PMTs can be substantially reduced [].

1.4.3 ^{10}B-lined detectors

As in the case of $^{10}BF_3$, the converter element is ^{10}B. In this case in its solid state, either pure or in a compound as $^{10}B_4C$. After the capture, the fission fragments may reach a gas medium where the ionisation process occur in the same way than in a standard proportional counter.

A typical PHS of a boron-lined detector is shown in Figure 1.12. Due to the use of a solid layer and its radiation self-absorbing properties the energy distribution found does not shown a clear separation from electronic noise and background, as the ones previously seen for ^{3}He and $^{10}BF_3$. Distributions due to the different reaction fragments, shown in Table 2.2, are visible: the α-particle from the higher branch ratio (with an energy maximum at $\approx$ 1470 keV) and the lithium fragment rom the same branch ratio (at a maximum energy of $\approx$ 830 keV). The absence of a valley implies difficulties for the γ-discrimination. Contrary to gaseous converters, when an energy threshold is set neutron events of an energy lower than the threshold will be lost which will decrease the detection efficiency.

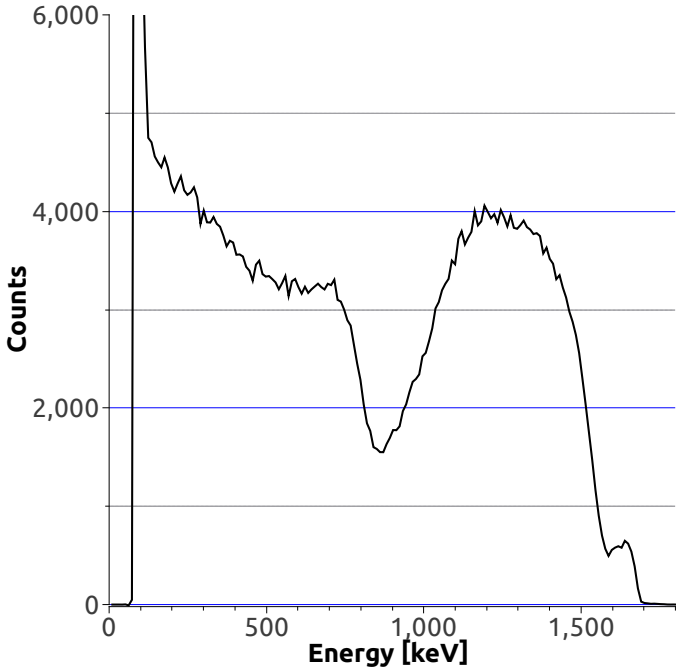

Figure 1.12: PHS of the $^{10}B_4C$-lined detector.

Due to its low efficiency, mono-layer boron-containing detectors have been used for beam-monitoring [15]. In order to reach detection efficiencies comparable to ^{3}He-based detectors a relatively thick layer of a boron-containing material is needed.

Different approaches have been tested by several groups. Two examples are studied here.

The Multi-Blade

This detector is based on the studies made for [16] in which Micro-Strip Gas Chamber (MSGC) filled with ^{3}He were placed surrounding the sample position in order to cover a large solid angle. An scheme of the whole detector is shown in Figure 1.13a.

The Multi-Blade detector uses a similar geometry. However, neutrons are converted in boron-containing films instead of ^{3}He. The main idea is to increase the effective thickness of the boron layer by placing the layers at relatively low angles (5° - 10°). Relatively high detection efficiencies $\approx 40\%$ can be reached with only a bilayer configuration. A scheme of one a Multi-Blade detector is shown in Figure 1.13b.

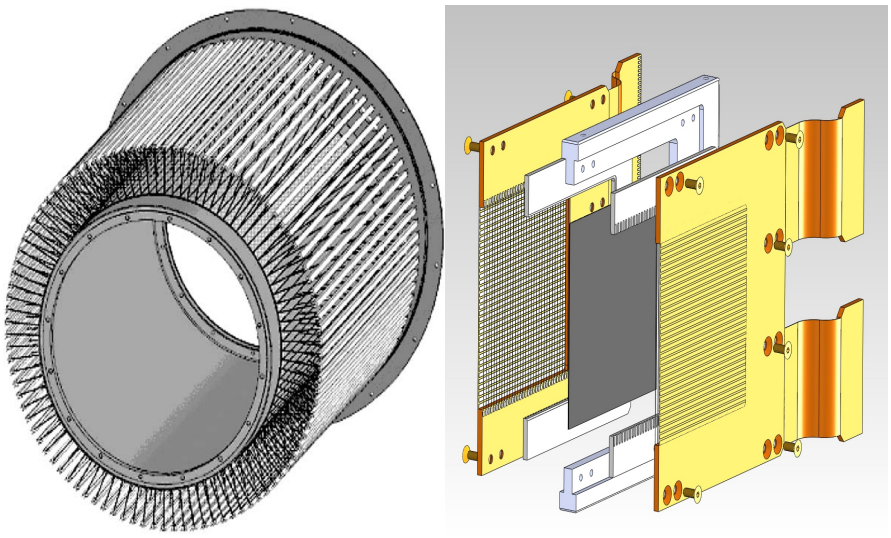

(a) (b)

Figure 1.13: **(a)** The original Multi-Blade using MSGC filled with ^{3}He [16] **(b)** The new Multi-Blade in which the neutron capture takes placed in the boron layer.

A boron-containing layer is placed in the middle of a Multi-Wire Proportional Chamber (MWPC). Reaction fragments able to escape the layer after a capture reaction will ionise the gas. A plane of wires is situated close to the boron layer and permit the gas amplification. Induction signals are read out through the wires. The use of some kind of localisation algorithm will increase the position resolution of the detector making it suitable for Neutron Reflectrometry.

^{10}B-based Straw Detector

Made by Proportional Technologies, straws tubes are built with an inner coating of $^{10}B_4C$ [17]. The scheme of how they are arranged is shown in Figure 1.14.

A 1 μm-thick $^{10}B_4C$ coating is deposited onto either copper or aluminium foils (which also acts as a cathode). These foils are thereafter rolled forming straws of several diameters, being the most common the 4 mm one. Anode wires are placed in the middle of the straws. This way a gas proportional counter is built. To increase the detection efficiency straws are densely packed forming large detectors.

Special attention needs to be paid to the front-end electronics used (and scheme is shown in Figure 1.15). To determine the position along the straw, the same system than previously mentioned for IN5 is used: the charge division.

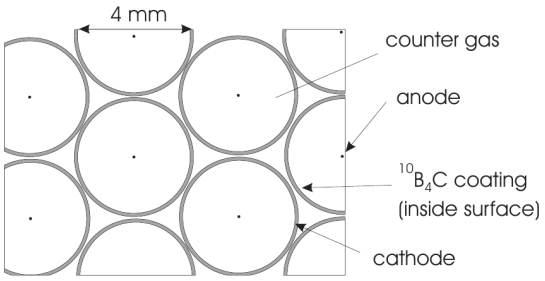

Figure 1.14: Scheme of a neutron detector formed by straw tubes built by Proportional Technologies [17].

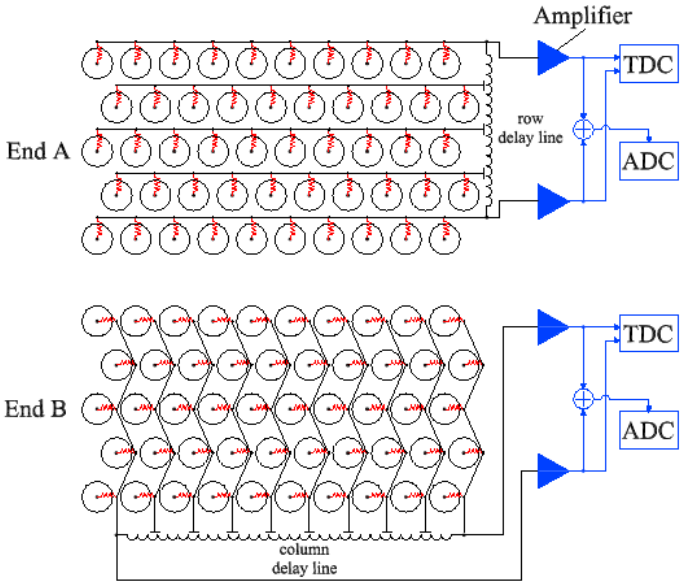

Figure 1.15: Scheme of the straw detector readout system [18].

A delay line between different straws depending on their position within the detector permits to decrease the number of readout channels needed.

Although several tests have been made for NSS their main purpose is the development of portal monitors able to fulfil the requirements of Homeland Security [19] in the US.

1.4.4 Summary

Main advantages and disadvantages of the mentioned alternatives to ^{3}He are summarised and can be found in Table 1.3.

The effort of the development has been split into the different NSS facilities.

	Advantages	**Disadvantages**
Scintillators	• Time Resolution	• Counting Rate • γ-Discrimination • Detection Efficiency
$^{10}BF_3$	• Fast Implementation • γ-Discrimination	• High Pressure & Voltage • Toxicity & Corrosion • Detection Efficiency
^{10}B-lined	• Counting Rate	• γ-Discrimination • Detection Efficiency

Table 1.3: Summary of the advantages and disadvantages of the alternatives mentioned.

A validation process of each one of these alternatives needs to be established. The use of one or other technique will depend on several variables such as the specific requirements of the instrument, the type of neutron source feeding the instrument, etc. A compromise between the technique performance and its availability is to be found. In this context, the detector for the NEAT instrument in HZB, initially designed to be ^{3}He-based, will use a $^{10}BF_3$ solution.

In the frame of the CRISP project [20] a collaboration between the ILL and the ESS has been established. The ^{10}B-lined technology has been chosen for the construction of a new LAND prototype suitable for a ToF instrument: the Multi-Grid detector.

1.5 Conclusion

The need of neutron detectors in NSS was introduced. Special attention was paid to a specific scattering technique: ToF, which requires LANDs. Together with large active areas other requirements are demanded: detection efficiency, high uniformity, long-term stability, time resolution and high signal-to-noise ratio. As a benchmark, the cold neutron spectrometer IN5 at the ILL was chosen.

The type of neutron source feeding the scattering instrument is also important for the detector design. Main differences between steady-state reactors and the new spallation sources were discussed.

Causes and consequences of the present ^{3}He shortage were discussed. The three alternatives selected by the scientific community were introduced and analysed: $^{10}BF_3$ gas counters, scintillators coupled to WSFs and ^{10}B-lined proportional counters. The latter was chosen for the development of a new LAND.

Chapter 2

Interaction Radiation - Matter

2.1 Introduction

Two are the main contributions which decrease the signal to noise ratio in a NSS instrument: the neutron background and the γ-contamination. In the first case, the cause is mainly the scattering interaction of thermal neutrons with the elements forming the detector itself. This interaction needs to be minimised reason why it is studied in Section 2.2.2.

The γ-contribution to the noise in the detector comes from the environment of the instruments in NSS facilities which, in some cases, can be relatively important. γ-insensitive neutron detectors are therefore preferred. The study of the γ response of the Multi-Grid detector in Chapter 7 will require basic concepts on photon - matter interaction. Some notions can be found in Section 2.4.

The interaction of two other types of radiation with matter is useful for this study: neutrons and ions. Incoming neutrons do not carry electric charge and therefore they do not interact with matter through the Coulomb force. In particular, thermal neutrons mainly interact with the nuclei of the medium. This interaction is studied in Section 2.2. In the case of the subsequent particles of a neutron capture reaction, energy values are in the MeV range for typical converters. These reaction fragments carry electric charge and their interactions will principally be with electrons of the converter elements as it will be seen in Section 2.3.

2.2 Interaction Neutron - Matter

The neutron is an elementary particle that naturally occurs in the nuclei of the atoms. It is formed by three quarks, two *down* and one *up*. However, at the energy range treated in this study, neutrons can be considered as point-like particles without any internal structure. Its mass has a value of $m = 1.68 \cdot 10^{-27}$ kg.

Free neutrons undergo a beta-decay reaction after an average lifetime of $\approx$ 881.5 seconds:

$$n \longrightarrow p + e^{-} + \overline{\nu}. \tag{2.1}$$

The energy of a neutron E, can be defined as a function of its wavelength λ, through the De Broglie relation [11]:

$$\lambda = \frac{\hbar}{mv} \tag{2.2}$$

where $\hbar$ is the reduced Planck constant, m is the neutron mass and v its velocity. The kinetic energy of the neutron becomes:

$$E = \frac{1}{2}mv^2 = \frac{\hbar^2}{2m\lambda^2}. \tag{2.3}$$

A classification of the neutron according to its energy, wavelength or velocity can be found in Table 2.1.

Label	**Energy [eV]**	**Wavelength [Å]**	**Velocity [km/s]**
Cold	0.05 - $5{\cdot}10^{-3}$	1025 - 4.045	$(3.86 - 978){\cdot}10^{-3}$
Thermal	0.005 - 0.5	4.045 - 0.405	0.978 - 9.77
Epithermal	0.5 - 1000	0.405 - 0.009	9.77 - 439.6
Intermediate	$(1 - 100){\cdot}10^{3}$	$(9.05 - 0.905){\cdot}10^{-3}$	$(4.40 - 43.71){\cdot}10^{2}$
Hot	$(0.1 - 10){\cdot}10^{6}$	$(9.05 - 0.905){\cdot}10^{-4}$	$(4.37 - 43.71){\cdot}10^{3}$

Table 2.1: Neutron classification. As a function of its energy – or equivalently wavelength or velocity – neutrons can adopt different names.

For a ToF instrument such as IN5, studied in Section 1.2.1, the velocity of the neutron is related with the energy resolution of the instrument as it will be studied in Chapter 7.

Independently of the incident radiation, the normalised probability for an interaction to take place is defined by its cross section, σ, usually measured in barn (1 b = 10^{-28} m^2). Each radiation will have a number of energy-dependent partial cross sections which correspond to the different types of interactions.

In most cases, the total cross section is defined as the algebraic sum of the partial ones.

$$\sigma_{tot} = \Sigma_i \sigma_i. \tag{2.4}$$

When a neutron crosses a medium it mainly interacts with the nuclei. Depending on the energy of the incident neutron and the nature of the medium, two main types of interaction are possible: *scattering* and *capture*.

In the first case, the neutron is deflected by a nucleus. This interaction is described by the neutron scattering cross section, σ_{scat}, and it can be split into two different processes depending on the energy conservation: elastic and inelastic.

During a capture interaction, the incident neutron is absorbed by a nucleus and secondary radiation is emitted. This interaction is described by the neutron capture cross section, σ_{capt}.

As seen in Equation 2.4, the total cross section is defined as the sum of the partial cross sections:

$$\sigma_{tot} = \sigma_{scat} + \sigma_{capt}. \tag{2.5}$$

The macroscopic cross section, Σ, with units of inverse length, is defined as $\Sigma = n\sigma$, where n is the atomic density of the medium. Consequently from Equation 2.5:

$$\Sigma_{tot} = \Sigma_{scat} + \Sigma_{capt}. \tag{2.6}$$

When a neutron beam, I_0, impinges into a medium it suffers an attenuation process that will exponentially decrease the number of neutrons along depth, x:

$$I\ (x) = I_0\ e^{-(\Sigma_{tot}\ x)}. \tag{2.7}$$

An important parameter to be used by the MC simulation in Chapter 4 is the average distance travelled by a neutron between collisions (or the mean free path, l). It can be defined as the inverse of the total macroscopic cross section:

$$l = \frac{1}{\Sigma_{tot}}. \tag{2.8}$$

The low energy transfer during thermal neutron scattering ($\leq$ meV) prevents this phenomenon to be used for neutron detection. Neutron capture offers access to secondary radiation in the form of charged particles with higher energies ($\sim$ MeV) making possible the detection.

2.2.1 Neutron Capture

Preferred elements for neutron detection show a high σ_{capt} together with the subsequent emission – in a short time interval ($\approx 10^{-15}$ s) – of secondary particles with energies in the MeV range. This secondary radiation, with higher energy that the incident neutron and electrically charged is used for the detection. The elements most common used as converters can be found, together with theirs capture reactions, in Table 2.2.

^{3}He + n	$\longrightarrow$	^{3}H + p + 0.77 MeV
^{6}Li + n	$\longrightarrow$	^{3}H + α + 4.79 MeV
^{10}B + n	$\longrightarrow$	(94%) ^{7}Li* + α + γ (0.48 MeV)+ 2.30 MeV
		(6%) ^{7}Li + α + 2.79 MeV
^{157}Gd + n	$\longrightarrow$	^{158}Gd* + e^{-} ($\leq$ 0.182 keV)
^{235}U + n	$\longrightarrow$	$H_{fis.}$ + $L_{fis.}$ + $\sim$ 180 MeV + 2.5 n

Table 2.2: The principal neutron converters used for thermal neutron detection are shown. Reaction fragments together with Q-values can also be found.

Despite their relatively large σ_{capt} for thermal neutrons ($2.59 \cdot 10^{5}$ and 680 barns respectively), ^{157}Gd and ^{235}U are not widely used for detection applications. In the case of ^{157}Gd, the relatively low energy ($\leq$ 0.182 keV) of the e^{-} spectra produced by the neutron capture prevents its use. In many cases these low energy particles will not be distinguishable from the γ-background. Some applications have however been found [21]. For the ^{235}U, energies of the reaction fragments are much higher ($\approx$ 180 MeV). However, the high density of the element ($\rho_U > 19$ g/cm^3) prevents the reaction fragments emitted deep in the converter to escape the medium. This make difficult to achieve efficiencies comparable to other converters. For other applications, such as beam-monitoring, fission chambers coupled to uranium converters are used [22, 23].

Other elements such as ^{113}Cd have a large σ_{capt} but secondary radiation emitted is normally formed by a broad range of γ-rays. Some applications however have been reported [24].

The energy-dependence of σ_{capt} for the three first elements in Table 2.2 can be found in Figure 2.1. A similar behaviour is found for the three of them for a wide energy range. This includes the energies of thermal neutrons used in NSS, already studied in Chapter 1. For E = 25 meV, or alternatively $\lambda = 1.8$ Å, the capture cross section for ^{3}He is $\sigma_{capt}^{^{3}He} = 5333$. In the case of ^{10}B and ^{6}Li they are found to be $\sigma_{capt}^{^{10}B} = 3835$ and $\sigma_{capt}^{^{6}Li} = 940$. This means 71.9% and 17.6% of ^{3}He respectively.

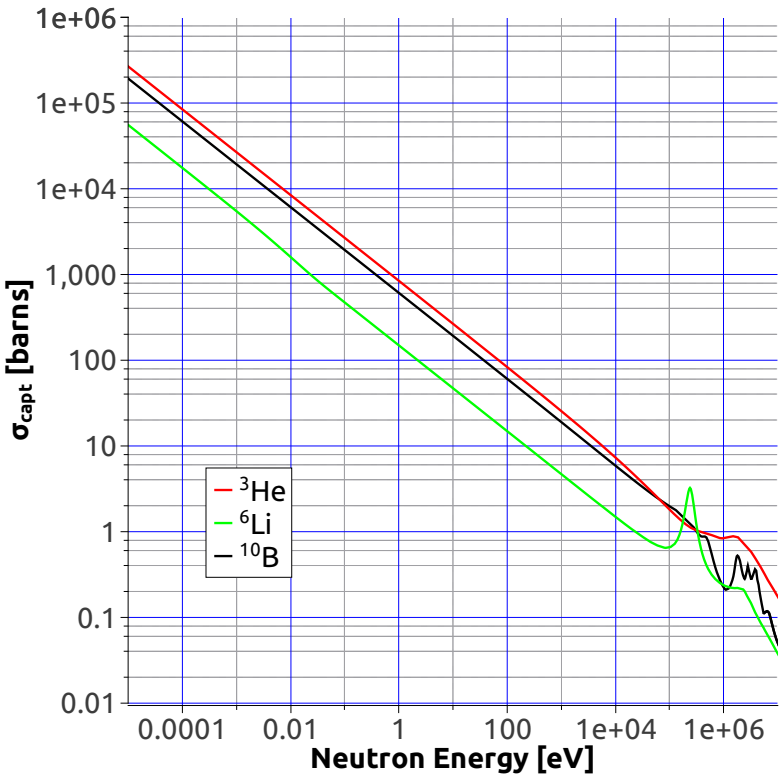

Figure 2.1: Energy dependence of the neutron σ_{capt} for the three elements more used in neutron detection [25].

2.2.2 Neutron Scattering

As seen above, the main process used for neutron detection is the neutron capture. However, neutron scattering plays also an important role. For thermal neutrons the three elements seen in Figure 2.1 shown a relatively high ratio $\sigma_{capt}/\sigma_{scat}$ (e.g., $\sim 10^3$ for ^{10}B). This does not apply for other elements present in a neutron detector such as aluminium where scattering dominates over other processes.

Due to scattering in aluminium, incident neutrons can be deflected in the window and other components of the detector. When the total aluminium thickness is relatively thick, scattering could induce a high neutron background and therefore a reduction in the detector performance. The use of aluminium needs to be minimised.

Both, σ_{tot} and σ_{capt} of ^{27}Al are shown in Figure 2.2 as a function of the neutron energy. While $\sigma_{capt}^{^{27}Al}$ increases over a wide range of energy, $\sigma_{tot}^{^{27}Al}$ becomes flat for energies between 0.01 - 10^4 eV. Note the three orders of magnitude

difference between $\sigma_{tot}^{^{27}Al}$ and $\sigma_{capt}^{^{10}B}$ previously seen in Figure 2.1.

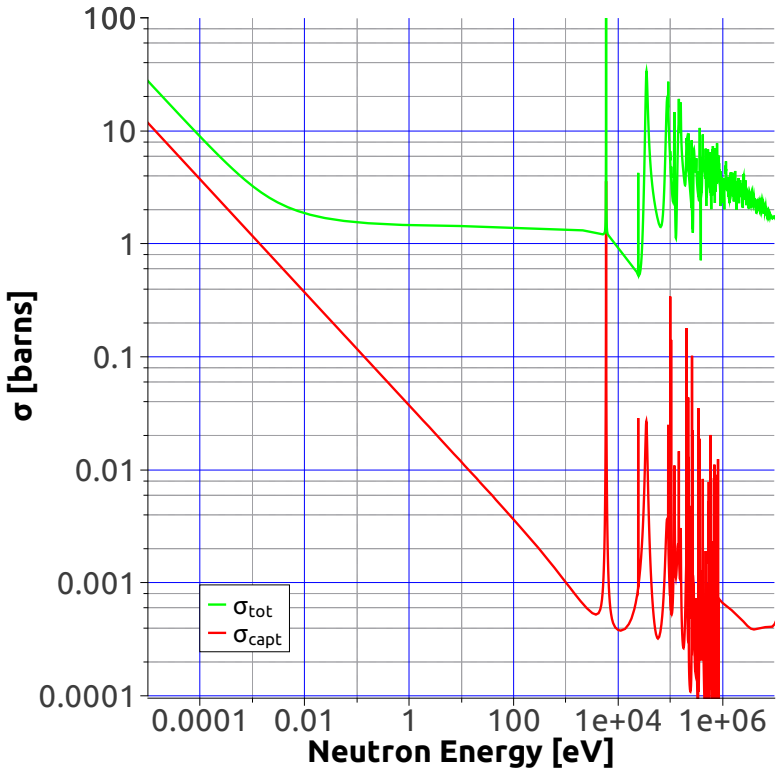

Figure 2.2: Total and capture cross sections for ^{27}Al as a function of the neutron energy. Note the change in the scale for σ compare with Figure 2.1 [25].

2.3 Interaction Ion - Matter

Ions emitted in the most common neutron capture reactions were shown in Equation 2.2. Interactions between these ions and the nuclei of the converter are possible but rare and therefore the main contribution to the stopping of the fragment comes from the electronic clouds [26].

Due to the large mass difference between ions and electrons the energy transfer per collision is small. A large number of interactions is needed to stop the fragment. The net interaction can be seen as a continuous slowing down process. As a result of these interactions excitation and ionisation of the medium atoms occur. During the first process, already mentioned in Section 1.4.2, the incident ion excites electrons of the atoms to a higher energy level. Light is emitted during the de-excitation and it constitutes the base of scintillation detectors. In the second case, positive ions and free electrons

are formed. These secondary particles are prevented to recombine by the application of an electric field. They are drifted and finally collected, as it will be studied in Section 3.2. Ionisation is the principal mechanism by which charged particles in the MeV range are slowed down in a medium. Therefore it constitutes one of the most important methods in radiation detection.

The *linear Stopping Power*[1], S, is defined as the differential energy loss of a charged particle within a medium divided by the corresponding differential path length:

$$S = -\frac{dE}{dx}. \tag{2.9}$$

The classical expression for the stopping power was firstly introduced by Bethe [27] and can be written as:

$$-\frac{dE}{dx} = \frac{4\pi e^4 z^2}{m_0 v^2}\, nB \tag{2.10}$$

where

$$B \equiv Z\left[ln\left(\frac{2m_0v^2}{I}\right) - ln\left(1 - \frac{v^2}{c^2}\right) - \frac{v^2}{c^2}\right]. \tag{2.11}$$

The quantities v and ze are the velocity and charge of the incident ion. n and Z are respectively, the atomic density and atomic number of the medium. m_0 is the electron rest-mass and e the elementary charge. I is known as the *average excitation energy* of the medium and is normally treated as an experimental parameter. Its value is proportional to Z.

For non-relativistic ions the Equation 2.11 becomes:

$$B \approx Z\ ln\left(\frac{2m_0v^2}{I}\right). \tag{2.12}$$

After the approximation, the Bethe Equation can be written as:

$$-\frac{dE}{dx} \approx \frac{nZz^2B(v)}{v^2}. \tag{2.13}$$

The term $B(v)$ slowly varies with the velocity of the incident particle. Equation 2.13 would then inversely vary with $1/v^2$ or the ion energy. This can be understood as follows. The energy transfer depends on the time that the ion remains in the vicinity of the electron which will be longer for slower ions. Consequently, the lower the energy of the ions the larger the stopping power. When the velocity of the incident ions, v, becomes comparable with c, the two last terms in B cannot be neglected and S slowly rises again.

[1] Also known as *specific energy loss* or *rate of energy loss*.

An analysis can also be done regarding the charge of the incident particle. In Equation 2.13, S increases with z^2. An α-particle ($z = 2$) has a larger stopping power than a proton of the same energy. Stopping power increases with the charge of the ion.

For the medium the dependence varies as nZ. This term represents the electron density. Therefore, high atomic number and dense materials show a large stopping power.

Let us study now the range of validity of the Bethe Equation. For a low velocity ion, Equation 2.12 becomes negative for $m_0 v^2 < I/2$. When the velocity of the ion is lower than $(I/m_0)^{1/2}$, that can be seen as the orbit velocity of the electrons, the Bethe Equation does not hold. In this situation charge exchange between the ion and the medium becomes important. The ion will pick-up electrons from the medium. Its charge will be reduced along the track which will decrease its stopping power. By the end of the track the ion has captured Z electrons and becomes a neutral atom.

A useful way to study the stopping power of a charged particle is to plot it along the track length. This is known as the *Bragg Curve*. An example of an α-particle travelling through CO_2 is shown in Figure 2.3.

The initial energy of the particle is E = 2 MeV. During most of the track the charge is equal to two electronic charges. The stopping power increases as predicted by Equation 2.13, 1/E. At x $\approx$ 10 mm an electron is captured and the curve falls off.

A new magnitude called *range* can be introduced. It is defined as the average distance that ions of certain energy can travel into a medium. In the specific case of Figure 2.3 this value is $r = 15.1$ mm. Due to the random track that each ion undergoes within the medium, the energy loss is a stochastic process. This results in a spread in energy which can also be seen as a range *straggle*.

2.4 Interaction Photon - Matter

As it will be shown in Chapter 7, γ-sensitivity constitutes an important property of the Multi-Grid detector to be tested. The understanding of this phenomenon requires a brief introduction to the most relevant photon - matter interactions.

There are three processes by which γ-ray photon-energy is converted into electron-energy: *photoelectric absorption*, *Compton scattering* and *pair production*. During these processes photons abruptly change their energy and

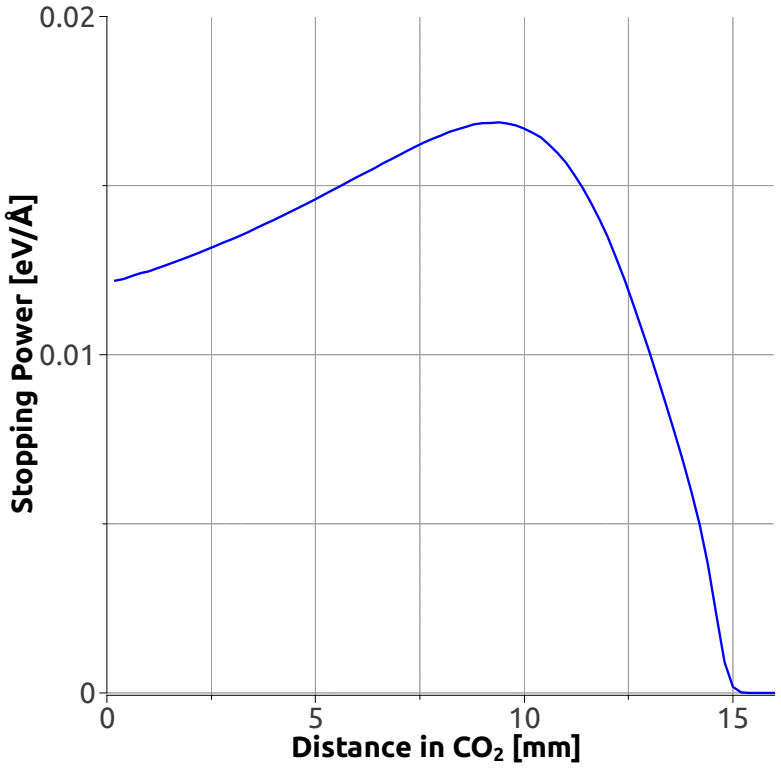

Figure 2.3: Bragg Curve. The stopping power, S, along the track length. The incident ion is an α particle with an initial energy of E = 2 MeV in CO_2 @ 1 bar. The curve follows the Bethe Equation described in Equation 2.13 until an electron is capture at x $\approx$ 10 mm.

direction. In a similar way to what was studied for neutrons in Section 2.2, the total γ cross section can be defined as:

$$\sigma_{tot}^{\gamma} = \sigma_{photo} + \sigma_{Compton} + \sigma_{pair} \tag{2.14}$$

where each energy-dependent partial cross section refers to the different processes mentioned above.

For a γ-ray, the linear attenuation coefficient, μ, can be defined as a function of σ_{tot}^{γ}:

$$\mu = \frac{\sigma_{tot}^{\gamma}\ N_A}{A}\rho, \tag{2.15}$$

where N_A is the Avogadro's number, A the atomic weight of the absorber medium and ρ its density.

The interaction probability of the different processes is a function of two parameters: the energy of the incident photon and the atomic number of the

absorber. This is shown in Figure 2.4.

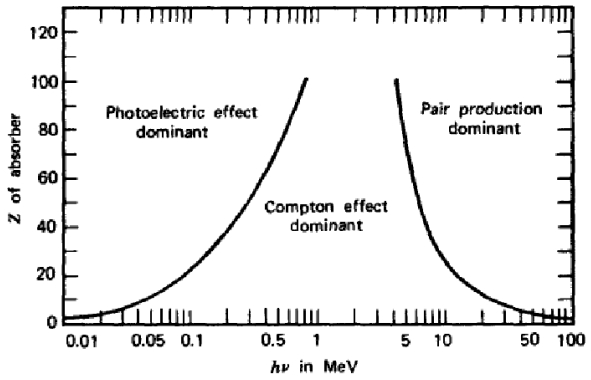

Figure 2.4: The relative importance of the three types of photon - matter interaction as a function of the energy of the incident γ-ray and the atomic number of the absorber material, Z [26].

To reduce the γ-sensitivity μ needs to be minimised. The interaction probability as a function of the γ-ray energy is shown in Figure 2.5 for the two main elements of the Multi-Grid detector despite the neutron converter itself: aluminium (used to fabricate the different mechanical pieces) and a typical quenching gas, CF_4.

The interaction probability is calculated by the software XCOM [28] using the aluminium and CF_4 thickness's that a γ-ray might cross inside a voxel of the Multi-Grid detector (to be defined in Section 5.2). The higher probability for the aluminium is due to its higher density compare to CF_4.

As seen in Table 2.2, the γ-ray generated in the neutron capture of ^{10}B has a energy of 482 keV. For this specific energy, interaction probabilities of $3.5 \cdot 10^{-5}$ and $1.1 \cdot 10^{-7}$ are found for aluminium and CF_4 respectively.

In the case of aluminium and as is shown in Figure 2.7, the electrons range is much shorter than for the quenching gas. As a result, when a photo-electron is created after a γ-conversion within the aluminium, it might not reach the gas and therefore will not generate a detection event.

For the energy range of typical γ-background in a NSS facility (from a few tens of keV to the 482 keV of the γ-ray mentioned above) only the photoelectric absorption and the Compton scattering are relevant.

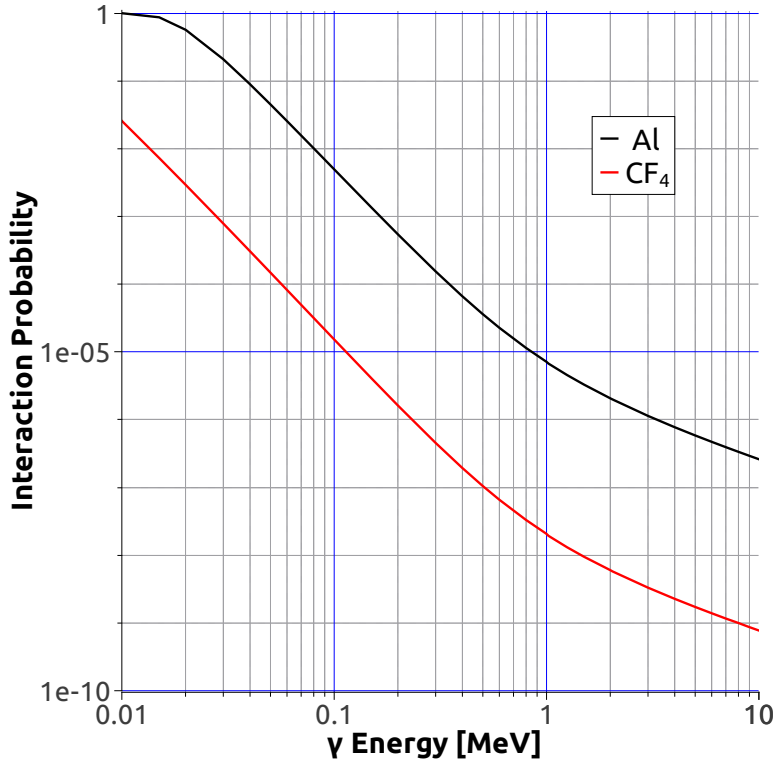

Figure 2.5: Interaction probability of a γ-ray for the two main materials of the Multi-Grid detector. Note the high values found for low γ energies [28].

2.4.1 Photoelectric Absorption

In this process the incident photon is completely absorbed by a target atom. An energetic *photo-electron* from one of the atom bound shells is ejected. The energy of this photo-electron is given by:

$$E_{e^-} = h\nu - E_b, \tag{2.16}$$

where E_b is the energy of the electron in the bound shell and $h\nu$ the energy of the incident photon. When $h\nu$ is higher than a few hundred keV, the ejected electron is likely to belong to an inner – most tightly – shell. In this case, most of the energy goes to the photo-electron. The vacancy created in the electronic structure of the atom is replaced by either free electrons of the medium or electrons from a different shell. This results in the emission of secondary radiation in the form of X-rays which are normally re-absorbed by another photoelectric process close to the original interaction point.

As it is shown in Figure 2.4, this is the principal interaction for elements

with a high Z at relatively low γ-energies.

2.4.2 Compton Scattering

When the energy of the γ-ray is much higher than the bounding energy of the electrons in the medium ($E_b \ll h\nu$), the interaction takes place between the photon and an essentially free electron of the medium.

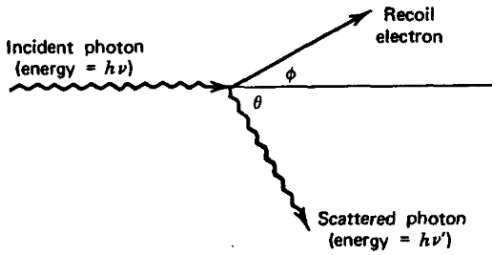

Figure 2.6: Diagram of the Compton scattering. The variation of the angle θ leads to a large energy spread [26].

The incident photon is deflected through an angle, θ, with respect to its original direction shown in Figure 2.6. The transmitted energy to the electron is function of θ. Since all angles are allowed, transmitted energy can vary from zero to a large portion of the original energy. The expression that relates these two parameters can be written as:

$$h\nu' = \frac{h\nu}{1 + (h\nu/m_0c^2)(1 - cos\theta)}, \tag{2.17}$$

where m_0c^2 is the rest-mass of the electron (0.511 MeV). The probability of Compton scattering per atom of the absorber medium depends on the number of electrons available and therefore increases with Z. The dependence with the energy of the γ-ray was shown in Figure 2.4, generally falls off with increasing energy.

2.4.3 Electron Interactions

As mentioned above, as a result of the photon-matter interaction a free electron is emitted. The study of its interaction is therefore needed for a complete analysis of the γ-sensitivity.

Single electrons are much more penetrating than heavy ions of the same energy. High energetic electrons follow paths in matter that are similar to what was seen for ions. For energies lower than 1 MeV however, important deviations

in the path of the electrons occur. These interactions with either nuclei or orbital electrons cause considerable energy transfers and large deflections. As a consequence, the tracks of the electrons are tortuous and a definition of range differs to what was shown in Section 2.3.

A qualitatively analysis can be done on the electron track within a neutron detector. The tortuous track is calculated with the software ESTAR [29]. If this track is unfolded it can be plotted as a function of the electron energy for aluminium and CF_4, as it is shown in Figure 2.7.

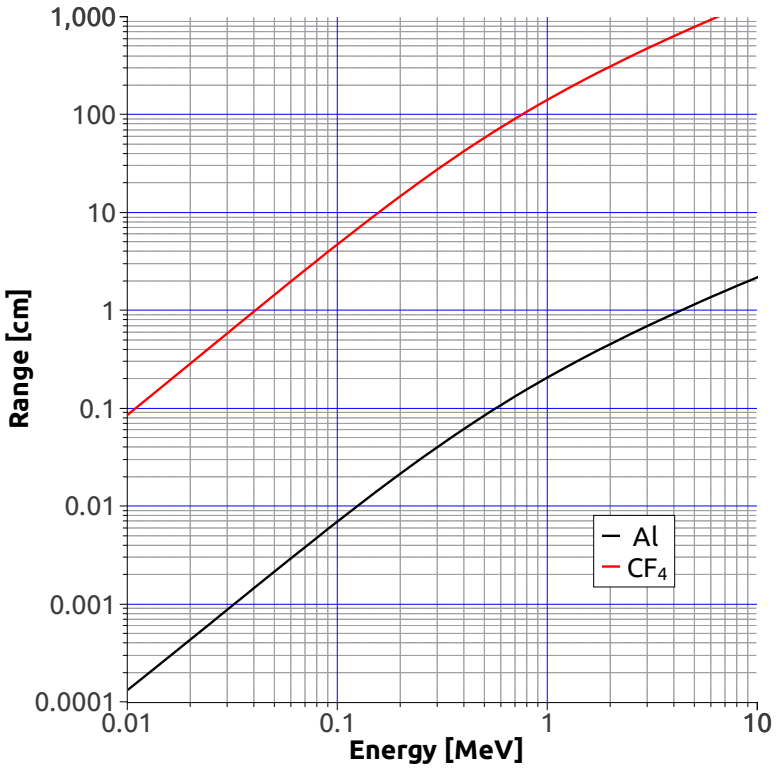

Figure 2.7: The unfolded track of an electron travelling in both aluminium and CF_4 as a function of its energy. A three orders of magnitude difference is found between them due to a large density difference [29].

Due to the much lower density of the gas, unfolded tracks are 3 order of magnitudes longer in the CF_4 than in aluminium. For the photo-electron created in the neutron capture of ^{10}B and with an energy of 482 keV the unfolded tracks are: 0.08 and 53 cm long respectively. The latter value is much longer than the voxel dimensions of the Multi-Grid detector (studied in Section 5.2). This implies that only a small fraction of the energy carried by the photo-electron is deposited in the gas. Low energy events are then expected

for γ-contamination processes.

2.5 Conclusion

The different interaction processes of neutron in matter were analysed. Due to the small energy transfer involved, scattering is not often used for detection purposes. The neutron capture of some elements however offers access to secondary radiation often composed of charged particles in the MeV range. This phenomenon is used in most thermal neutron detectors. Energy dependence and capture reactions of the most efficient converters were studied. Different detection techniques using these converters were already discussed in Section 1.3.

The interaction of subsequent charged particles with matter is studied. The stopping power of ions in matter was defined through the Bethe Equation. Its relation with some properties such as the charge of the incoming particle and its energy, the electron density of the medium, etc. were addressed. Useful parameters such as range or Bragg curve were also defined.

In order to analyse the γ-contamination to be discussed in Chapter 7, a study of the photon-matter interaction was made. For the γ-energy values commonly found in NSS facilities only the photoelectric absorption and the Compton scattering are relevant. The interaction probability within the Multi-Grid detector as a function of the γ-energy was analysed. Photo-electron unfolded ranges were studied. Low energy events are expected from γ interaction of a broad range of energies.

Chapter 3

Basics of Gaseous Neutron Detectors

3.1 Introduction

After the neutron capture interaction studied in Chapter 2, the subsequently reaction fragments which have escaped the boron-containing converter reach the stopping gas. Due to the Coulomb interaction, when particles pass through a gas they deposit their energy in the medium and create a certain charge, Q. It is the so-called gas ionisation. This phenomenon constitutes one of the most common methods used for radiation detection.

To prevent recombination an electric field is created within the gas volume. Charges drift from the point where they are produced – along the track of the reaction fragments – towards the electrodes according to their sign. The movement of these charges inside the electric field induce electric signals used to detect particles. An analysis of how signals are induced in the detector is given in Section 3.3. For special geometries, the electric field can produce gas amplification. This phenomenon is studied in Section 3.2.1. The most common criteria to select an appropriate stopping gas are reviewed in Section 3.2.2. According to this analysis, two gas species were chosen for the operation of the Multi-Grid detector. Results with each of these gases are studied in Chapter 7.

In Section 3.4, some general properties of radiation detectors are reviewed. Two different operation modes: current and pulse, are studied. Its implementation is chosen as a function of several parameters such as the expected rate and the type of information to be acquired.

Detection efficiency is defined. This parameter is used in Chapter 4 to evaluate different results obtain by the MC simulation. Some of its most

important reducing factors are reviewed.

The two different behaviours of a radiation detector with respect to the dead time are studied. Expressions to estimate the detector dead time are obtained for both behaviours will be implemented in Chapter 7.

3.2 Gas Ionisation

When a charged particle passes through a gas medium it losses its energy creating both excited and ionised molecules along its path. After a molecule is ionised the resulting positive ion and free electron are called an *ion pair*. Free electrons may have enough energy to create further ions. These high energetic electrons are called *delta rays*. Since their range is much shorter than the primary particle, in most cases no difference between ionisation created by the incoming particle or by the delta rays can be measured.

The energy needed to ionise a gas molecule – or its ionisation potential, I_0 – is some 10-25 eV. However since there is other non-ionising processes in the gas, the average energy lost per ion pair, known as W, (which takes all processes into account) is more often used. Its value is not strongly dependent on the gas species, the type of incident particle or its energy. These parameters are shown for several gases in Table 3.1.

Gas	**Z** [a.m.u.]	**I_0 [eV]**	**W [eV]**	**Range [mm]**
Ar	18	15.8	26.4	11.2
CO_2	22	13.7	33.0	6.64
N_2	28	15.5	34.8	10.2
O_2	32	12.2	30.8	9.92
CF_4	42	15.9	54	4.32
Xe	54	12.1	22.1	6.15

Table 3.1: The ionisation potential, I_0, and the average energy lost W, are shown for several commonly used gases in particle physics. Note the short extent of values for I_0. Ranges are calculated for an α-particle of E = 2 MeV and gas pressures of 1 atm. [30]

Once the charges have been created in the gas, the natural tendency of ions to recombine and form neutral atoms is prevented by the application of an electric field. This field causes the electrons and ions to drift towards opposite sides of the detector where the electrodes – biased at a certain applied voltage – are placed.

As a function of the applied electric field several regions of operations can be

defined. In one of them, the *proportional region*, a multiplication in the number of charges is produced. The total number is however kept proportional to the primary charge.

3.2.1 Proportional Counter

Proportional counters rely on the phenomenon of *gas multiplication*. During the drift towards the electrodes both positive ions and free electrons created by the primary ionisation suffer many collisions with neutral molecules. At high values of the applied electric field electrons may reach kinetic energies higher than the ionisation potential of the gas molecules shown in Table 3.1. The generation of secondary ion pairs is produced.

The free electrons created after this secondary ionisation will also be accelerated by the electric field. They will undergo further collisions with neutral molecules which can produce further ionisation. The gas multiplication takes the form of a cascade also known as the *Townsend avalanche*. The increment in the number of electrons per unit path length is given by the Townsend equation:

$$\frac{dn}{n} = \alpha \, dx, \tag{3.1}$$

where α is the first Townsend coefficient. When integrating Equation 3.1 for a parallel-plate geometry, as it is described in Equation 3.3, the increment on the electron density can be calculated:

$$M = \frac{n(x)}{n(0)} = e^{\alpha \cdot x}, \tag{3.2}$$

where n(x) is the density of electrons after a path length x and M is the multiplication factor or gas gain. The avalanche ends when all free electrons reach the electrode. Heaviar positive ions show a lower mobility. They cannot reach a kinetic energy enough to ionise gas molecules. Gas amplification is only caused by electrons.

In order to create an electric field high enough to start an avalanche an important parameter to adjust is the geometry of the detector. Starting with the simple case of the parallel plates, the electric field is given by:

$$E = -\frac{V}{d} \tag{3.3}$$

where V is the applied voltage and the d the distance between the plates. The negative sign is due to the repulsion between charges of the same polarity. To create high electric fields under this configuration high voltages or small

distances between the plates are needed. An example of this are the Resistive Plate Chambers (RPCs) described in [31].

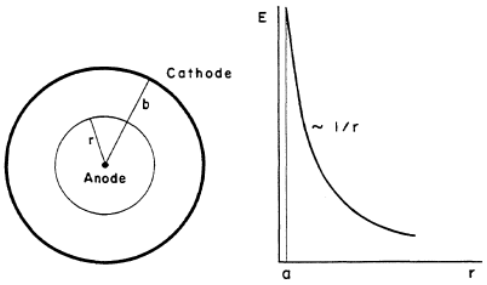

Figure 3.1: Scheme of a cylindrical shape proportional counter where a is the anode wire radius. The electric field as a function of the distance from the wire is shown. [30]

The use of a cylindrical geometry is shown in Figure 3.1. A wire acting as the anode is placed in the middle of a cylindrical tube which serves as the cathode. The electric field created at a radius r is given by:

$$E\ (r) = -\frac{V}{r\ ln(b/a)}, \tag{3.4}$$

where a is the wire radius and b is the cathode inner radius. High electric fields can be created by using thin wires: standard radii for wires used in proportional counters are in the order of few tens of μm. In this case the Townsend coefficient varies along the path length, $\alpha(x)$, so a steeper behaviour than for a parallel-plate geometry is found. The minimum electric field need for avalanche formation is only reached at distances from the surface of anode comparable to the radius of the wire.

Under certain conditions secondary ionisation can be kept proportional to the number of primary ions pairs formed. The total number of ions can be however, multiplied by a factor of many thousands (the previously defined as M). In fact, gaseous detectors have several regions of operation which are shown in Figure 3.2.

At very low values of applied voltage the electric field cannot prevent recombination of original ions pairs. The collected charge is less that the originally deposited by primary ionisation. As the voltage is raised the ion saturation region is reached. Recombination processes can be considered negligible and all ion pairs created by primary ionisation are collected. Further increases in the electric field do not yield higher signals because the charge have already been collected. This is the typical operation mode of ion chambers [32]. When the electric field reaches the minimum value for gas multiplication the collected

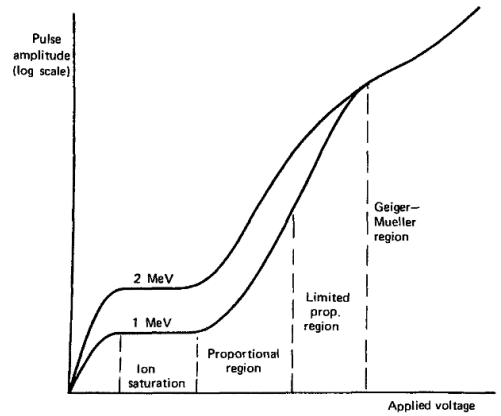

Figure 3.2: The different regions of operation of a proportional counter are shown for events deposing two different amounts of energy. [26]

charges multiply: the pulse amplitude increases. Over some region of the applied electric field the gas multiplication is linear and collected charge will be proportional to the primary charge created in the gas. This is the region where proportional counters operate. Some non-linearities can be found at the edge of this region due to the *space-charge effect*. Positive ions created during the avalanche drift a long path (from the avalanche region to the cathode) at a relatively low speed. If the concentration of this ion cloud is high enough the electric field can be modified. If the voltage is further increased this effect becomes dominant. Multiplication takes places until a certain number of positive ions is created. The minimum electric field is not reached any more and the avalanche is stopped. The output amplitude have the same value and it no longer depends on the primary charge, or equivalently the energy. This zone is known as the *Geiger-Mueller* region.

Although for some applications detectors working in the ion saturation regions have been reported [], the proportional region is more commonly used. Discrimination of other types of incoming radiation, specially γ-rays, needs of a energy studied of the output signals which is not be possible for a detector working in the Geiger-Mueller region. Single proportional counters are used for many applications in NSS. This system has been chosen for the Multi-Grid detector as it will be shown in Chapter 5.

3.2.2 Choice of the Filling Gas

Four features of gaseous detectors have been chosen to show the importance of the filling gas. Parameters such as the average energy lost of the gas molecules

or the drift velocity are strongly related with detector characteristics as the signal-to-noise ratio or the rate capability.

Signal-to-Noise Ratio

In order to properly distinguish events from background noise the factor signal-to-noise ratio needs to be maximised. Several parameters of the filling gas can be tuned.

- As seen above, the *average energy lost, W* is defined as the average amount of energy required to ionise a gas molecule. It takes into account all the other non-ionising processes reason why its value is larger than the ionisation potential, I_0. Its value it is not strongly dependent on the gas species, or the incoming particle type or energy. The lower the W the larger number of primary ion pairs created in the gas for the same incoming particle.

- Gases showing a higher *M* or *gas gain* generate a larger number of secondary ion pairs during the gas multiplication. This fact implies higher amplitude signals generated.

- The *electro-negativity* is a property of some gases (mainly oxygen and water) to create negative ions by the attachment of a free electron. These negative ions can recombine with positive ions and a net loss in the collected charge is produced. The contamination of the gas mixture with a low percent of the mentioned gases could induce an important reduction of the signals amplitude, as high as 30% in some cases [30].

- The *gas amplification threshold* is defined as the electric field value by which the gas multiplication starts. The lower the electric fields the lower the bias voltage applied to the detector. For practical reasons gases with a low threshold value are preferred.

Rate Capability

In order to evaluated the rate capability of a detector as a function of the gas species the *drift velocity* is studied. A higher drift velocity – for both free electrons and positive ions – implies a shorter dead time of the detector. The whole signal generation process ends faster and, for the same recovery conditions, the detector is ready for a new interaction.

Long Lifetime

Long time operation of the detectors requires both good *stability* and reduced *ageing*. As it will be seen below, the use of polyatomic gases (eg. CF_4) as quenchers results, for high rates, in the deposit of polymers in the anode. This polymerisation causes the ageing of the detector or a reduction of its lifetime.

Spatial Resolution

Two are the gas parameters related with the spatial resolution to be studied.

- The stopping power, was already studied in Chapter 2. For the same gas pressure, the length of the track within the gas volume will be mainly a function of the electron number of the gas molecule. In this sense, gases formed by heavy molecules will reduce the track length of the reaction fragments and therefore allow a better spatial resolution.

- Also important is the *electron diffusion*. If the primary electrons drifting towards the anode spread over a large area a degradation on the spatial resolution would be produced.

Another important characteristic for the study of filling gases is the *quenching*. For some gases, ionisation is not the only energy deposit mode when a charged particle travels through it. Radiative de-excitations are possible. Photons generated during this process give raise to photo-electrons and some distance of the original track. Delayed spurious avalanches are generated and can rapidly start a discharge regime. A way to avoid this effect is adding a small amount of a polyatomic gas or *quencher*. They show several modes of non-ionising energy dissipation (mainly through vibration and rotation of the molecule) which can absorb the photon-radiation without any radiative emission. Typical compounds used for this purpose are hydrocarbon and alcohol families together with CO_2 or CF_4 among others.

The polyatomic gas CF_4 was chosen as a filling gas for the Multi-Grid detector. As seen in Table 3.1, its average energy lost is relatively high. Its scintillation properties have been used for a new kind of gas scintillator neutron detectors [33]. Moreover, as it will be shown in Figure 3.4 is a fast gas. As a drawback, ageing problems have been reported []. A second filling gas, Ar-CO_2 (90-10%) with a better stability and lower gas amplification threshold has also been used and compared to CF_4. Different experiments were performed using both gases. Results are presented in Chapter 7.

3.3 Signal Generation

After the ionisation process, the charge drift and the gas amplification the signal generation is now studied. The movement of charged particles inside an electric field produces a signal induction in the electrodes of the detector. Three are the factors to be studied in order to understand how signals are formed in a proportional counter: the electric field, the charge mobility and the induction phenomenon.

3.3.1 The Electric Field

The electric field, E, produced inside the detector volume when the bias voltage is applied can be defined through the electric potential, φ:

$$E = -\nabla\varphi. \tag{3.5}$$

The electric field close to the wire is expected to be similar to what was seen for a cylindrical geometry. As it will be shown in Chapter 5, the geometry of the Multi-Grid proportional counter is based on rectangular tubes (20 mm $\times$ 10 mm). Lower field regions are expected at the corners of the voxel. E was simulated with the Garfield suite [34] and it is shown in Figure 3.3 for the Multi-Grid standard voxel.

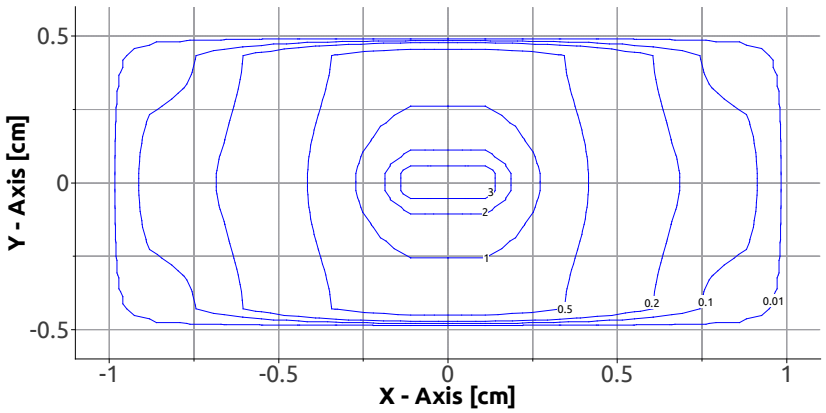

Figure 3.3: The electric field for the Multi-Grid tube was calculated with Garfield [34]. Lines show the shape of the electric field in kV/cm.

As expected E shows high values around the anode wire (which is placed in the middle of the voxel). From there it decreases towards the biased walls. Lower field zones are found at the corners of the rectangular tubes. Primary charges created in these zones will take a longer time to be collected. This

increment of the detector collection time, t_c – to be defined in Section 3.4.1 – might induce loses in the collected charge. It is the so-called ballistic deficit. To study this effect, fine scans were performed along the longest side of the voxels. Results will be shown in Section 7.2.3.

3.3.2 Charge Mobility

Due to the applied electric field the generated ion pairs will be forced to move away from the interaction point. With a mobility $\sim 10^3$ lower than free electrons positive ions are negligible for this part of the study. The net motion for free electrons is a superposition of random thermal velocity together with the drift induced by the field. The drift velocity can be defined as:

$$\nu^- = \frac{\mu^- E}{P} \tag{3.6}$$

where E is the electric field strength, P the gas pressure and μ^- the free electron mobility.

The electron drift velocity, ν^-, as a function of the electric field is shown in Figure 3.4 for the two quenching gases used in the Multi-Grid detector at atmospheric pressure.

ν^- is found to be approximately a factor of ten higher for CF_4 than for Ar-CO_2 (90-10 %) for a large range of electric field values found within the Multi-Grid voxel. This parameter defines the starting time of the avalanche: after the first ion pairs have been created, free electrons travel towards the anode at this velocity. For the same electric field and same track, free electrons generated in CF_4 will reach the high field region around the wire faster than in the case of Ar-CO_2.

3.3.3 Signal Induction

Due to the short distance from their emission to the wire and their higher mobility free electrons created in the avalanche process will rapidly reach the anode. For this reason their contribution is small ($\sim 1\%$). The much heavier positive ions will move towards the cathode at a lower velocity. It is this movement which creates a measurable induction current in both the anode and cathode electrodes. This idea was first introduced by Shockley and Ramo [35, 36] and can be found in Equation 3.7 in its simpler expression.

$$i = q\overrightarrow{v} \cdot \overrightarrow{E}_0 \tag{3.7}$$

where q is the charge of the ion, $\overrightarrow{v}$ its velocity and $\overrightarrow{E}_0$ the weighting electric field.

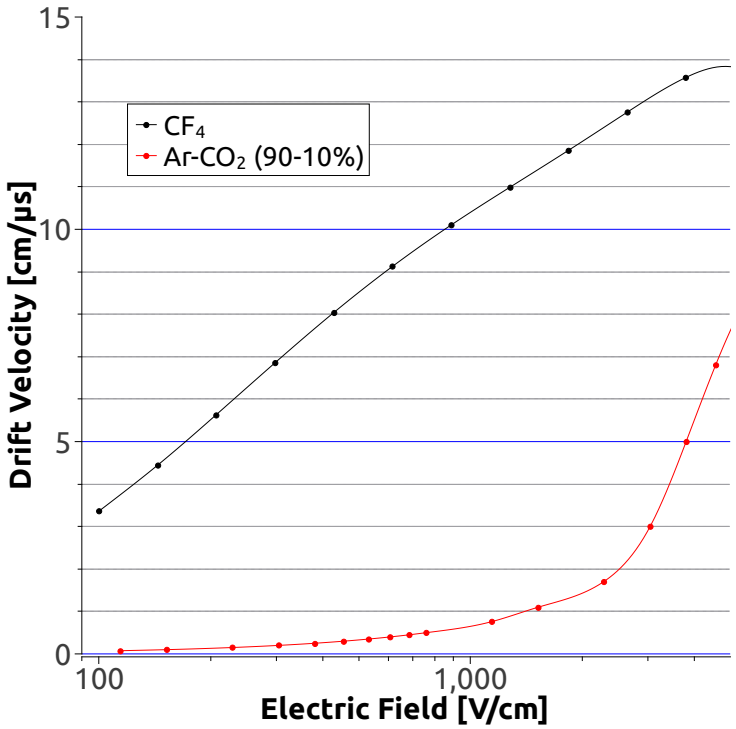

Figure 3.4: Electron drift velocity ν^{-}, as a function of the electric field, E, for gases @ 1 bar.

Ions created during the avalanche drift towards the cathode which implies that, for the anode wire, $\overrightarrow{v}$ is negative. The vectorial product in Equation 3.7 is then negative. As a result, negative-polarity-induced signals are measured in the anode wire.

For the cathode a similar explanation can be given. In this case positive ions drift towards the cathode: $\overrightarrow{v}$ is positive. The vectorial product becomes positive. Positive signals are measured in the cathode electrodes.

3.4 General Properties of Radiation Detectors

Three properties to be study in the characterisation of the Multi-Grid in Chapter 7 detector are defined now.

- The *operation mode*: two different modes are described. The front-end electronics circuits connected to the detector and the various range of application for each of them are analysed.

- The *dead time* or the time needed for the detector to recover after an event is examined. It plays an important role under high counting rates.
- The *detection efficiency* or the number of recorded events divided by the total number of incoming particles is studied.

3.4.1 Mode of Operation

When the energy deposited by an incoming particle in a radiation detector is to be registered the *pulse mode* is used. Energy is related to the total charge collected in the detector for each event, Q. However, at very high rates the pulse mode becomes impractical. Successive events overlap and the time between pulses do not allow an adequate counting. In this context the current mode can be used: the detector reacts to variations in a time average rather than individual events.

The equivalent front-end circuits for both modes are shown: current mode in Figure 3.5a and pulse mode in Figure 3.5b.

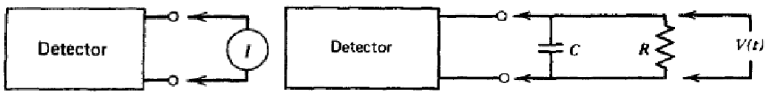

(a) (b)

Figure 3.5: **(a)** Front-end circuit of a radiation detector working in current mode. The current is measured as a function of time through an ammeter. **(b)** Equivalently, the front-end circuit of a detector operating in pulse mode: varying RC two different modes of operation can be implemented [26].

Current Mode

As it was shown in Figure 3.5a, current variations are measured with an ammeter plugged to the output of the detector. Assuming that it has a fixed response time, T, the time-dependent recorded current will be given by:

$$I(t) = \frac{1}{T}\int_{t-T}^{t} i(t')dt'. \tag{3.8}$$

T is usually chosen to be long compared with the average time between individual current pulses. The average current, I(t) – a function of the interaction rate and the charge per interaction – is recorded. A scheme of this parameter is shown in Figure 3.6.

A statistical uncertainty in the signal due to the random fluctuation of the incoming radiation is measured at any instant of time. This effect can be minimised by increasing T. However, the response to rapid changes in the rate will be slowed down.

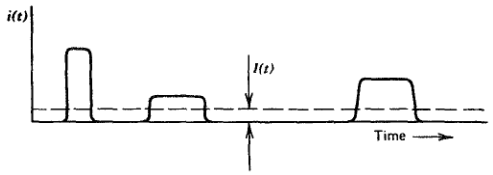

Figure 3.6: The current mode works time-averaging the current output of a radiation detector. Fluctuations in I(t) are minimised if T is large compare to the average time between pulses [26].

This type of operation mode is mainly used when the counting rate is too high for a proper analysis of individual pulses. At high rates time between pulses is reduced and overlaps between consecutive events become important. The use of an average current minimises these effects. Fission ionisation chambers used as neutron monitors in irradiating environments usually operate in this mode [37].

Pulse Mode

The charge deposited in the detector is read through the RC front-end circuit shown in Figure 3.5b. R is the input resistance of the circuit and C the equivalent capacitance of both the detector itself and the load circuit. The nature of the pulse produced from a single event largely depends on the characteristics of this circuit.

Two separated operation modes can be defined as a function of the time constant of the load circuit, $\tau = RC$, and how it compares with the charge collection time of the detector, t_c:

- In the first case τ is kept small compared to t_c. The current flowing through the resistance R is equal to the instantaneous value of the current flowing in the detector, $i(t)$.
- If RC is large, t_c is short compare to τ. Current flowing through R is very low and it will be momentary integrated on the capacitance. If we assume large intervals between pulses, the capacitance will discharge through the resistance returning the voltage $V(t)$ to zero. This second case is widely used in radiation detectors. The rising time of the pulse is

only determined by the t_c. The decay time of the pulse is only determined by τ. The maximum amplitude V_{max}, is directly proportional to the corresponding charge deposited within the detector:

$$V_{max} = \frac{Q}{C}. \tag{3.9}$$

As said above, under high rates some information might get lost. The most common reason is the pile-up effect.

Pile-Up effect When working in the pulse mode there is a potential risk of information lost. At high rates a situation in which two consecutive pulses partially superpose becomes non negligible. This would induce a shift towards low energies in the PHS when and undershoot is produced. Alternatively, if after the first pulse a relatively long tail is generated the PHS would show a shift towards high energies. In some cases, two events can completely overlap and only one (with double amplitude) will be recorded. These effects can be reduced by using front-end electronics with shorter τ. The decay time of the pulse will be shortened. As it was seen above, a limit in the reduction of τ is given by the condition: $\tau \gg t_c$.

The pulse mode was chosen over the current mode for this project due to the need of individual event information to be recorded. Two are the main advantages for boron-lined neutron proportional counters in NSS instruments using the pulse mode:

- As seen in Section 1.4.3, γ-sensitivity is a potential problem to be studied. Typical methods to overcome it are either an energy threshold or a pulse shape discrimination. An individual treatment of each event is a priori necessary to implement the γ-separation.
- The time resolution of the detector is an essential requirement in the case of ToF instruments, as seen in Section 1.2.1. The time average – based in the relatively long time response, T – used in the current mode does not allow to achieve the required time resolution.

3.4.2 Detector Efficiency

The efficiency of a neutron detector, ϵ, can be defined as the product of the neutron capture efficiency by the converter multiplied by the detection efficiency of the subsequent reaction fragments emitted after the capture:

$$\epsilon = \xi \left(1 - e^{-(\Sigma_{capt} \cdot d)}\right). \tag{3.10}$$

Σ_{capt} and d are the macroscopic capture cross section and the thickness of the converter respectively. While the so-called capture efficiency is into parenthesis in Equation 3.10, ξ has been defined as the detection efficiency of the subsequent reaction fragments of the capture interaction. It is a function of different factors. For detectors in which the neutron converter medium is a gas, such as ^{3}He or BF_3, ξ is ≈ 1.

In order to discriminate neutron interactions from other kind of radiation, such as γ-rays or electronic background, an *energy threshold* is usually set. Pulses with amplitudes higher than the threshold value are accounted. In some cases events will not reach the threshold value and the interaction is not recorded. ξ is therefore reduced. Some of the factors decreasing it are enumerate now.

- When reaction fragments produced in a neutron capture interaction hit the wall which contains the gas volume a part of its energy is not deposit in the gas. This phenomenon is known as *wall-effect*. Consequently, a lower amplitude is measured in pulses produced by events in which the wall is hit. If this amplitude does not reaches the previously seen energy threshold, the event will not be accounted.

- Other *non-ionising processes* such as Bremsstrahlung, Čerenkov or excitation take place in the gas. As mentioned in Section 1.4.2, the latter interaction is the energy deposit process used in scintillator detectors.

To the mentioned effects another one is to be added if the converter is solid. In that case, the radiation self-absorbing properties of the converter medium will decrease the energy of the reaction fragments when they pass through it. In some cases the emitted fragments will not leave the converter and the gas amplification will not take place. Fission fragments which can escape the converter will in any case show a lower energy which might not be enough to reach the threshold value and therefore to trigger a detection acquisition.

Until now ϵ has not taken into account any geometrical effect besides the wall-effect. It is the so-called *intrinsic* efficiency. However, a radiation detector does not provide a constant efficiency over the whole active area. Taking the IN5 PSD seen in Section 1.2.1 as an example, the capture efficiency – defined into parenthesis in Equation 3.10 – will depend on the interaction point of the incoming neutron along the diameter of the tube. This dependence comes from the factor d, or the thickness of the converter medium, which is not constant for a detector formed by round tubes. The detection efficiency calculated over the whole active are is *absolute efficiency* [26]. The difference between intrinsic and absolute efficiency can be seen in Figure 3.7.

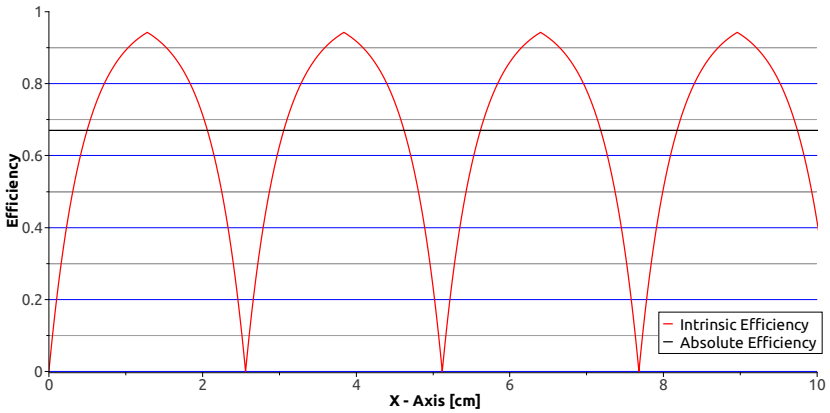

Figure 3.7: Calculated capture efficiency for the IN5 PSD. Operation values for the ^{3}He pressure and neutron wavelength that the real instrument are used (P = 4.75 bar and λ = 4.5 Å). As expected, the maxima of the distributions are placed at the centre of the cylindrical tubes. Then it decreases towards zero when approaching the edge of the tube. If an integration over the whole length is done the absolute efficiency found is 67.02 %.

Calculated efficiency is shown along the X-axis for the PSD of IN5. Typical conditions were used (λ = 4.5 Å, P = 4.75 bar ^{3}He). Although the intrinsic efficiency for the IN5 PSD at the centre of the tube reaches the 94.26%, if an integration is done over the whole length the *absolute efficiency* is found to be 67.02%.

Moreover, regions within the active area but not covered – the so-called dead zones – can be important in some PSDs. For IN5, a dead zone corresponding to the diameter of a tube and place between the different modules was previously mentioned. If an integration over the whole active area is performed the resulting absolute efficiency will be lower. Geometries which reduce the dead zones of the PSDs and also push the absolute efficiency closer to the intrinsic one can be advantageous. The rectangular tube geometry proposed for the Multi-Grid prototype, to be studied in Chapter 5, is a further step in this direction.

3.4.3 Dead Time

For detection systems working in pulse mode there is a minimum time needed to properly separate between two pulses, to be recorded as two different events. This is usually called *dead time*. The losses due to this effect can be important under high rates. Corrections need to be implemented to minimise them.

If we define τ to be the detector dead time, n the true rate and m the recorded rate, two types of detector behaviour can be defined as a function of how they can be affected by the dead time [26]:

- **Paralysable** When an event occurs during the dead time of the detector, it is not accounted but it increases the dead time by another period τ. A relation between the real rate and the recorded one can be established:

$$m = ne^{-n\tau} \tag{3.11}$$

- **Non-paralysable** In this case, if an events occurs during the period τ it is still not accounted but it does not increases the dead time. The equivalent relation can be defined:

$$n = \frac{m}{1 - m\tau} \tag{3.12}$$

In many cases, the dead time mode varies as a function of the processing electronics. For the Multi-Grid thermal neutron detector different associated electronics show different behaviours: Both modes are therefore used. Expressions obtained will be used to estimate the dead time in Chapter 7.

3.5 Conclusion

Processes involved in gaseous detector were studied: gas ionisation, charge drift, gas amplification and signal generation. Differences between detectors working in the ion saturation, the proportional or the Geiger-Muller zone were discussed. Due to the high signal-to-noise required to discriminate γ-events, a solution based on proportional counters was chosen for the Multi-Grid detector.

The electric field E, was calculated for the Multi-Grid voxel. Significant low-field regions were found at the tube corners. Longer collection time t_c, is expected for charge created in these regions. One-dimension scans to be shown in Section 7.2.3 will not only study the wall-effect problem close to the corner of the tube but also these low-field regions.

Different stopping gases properties were studied. The electron drift velocity was compared. CF_4 is $\sim$ 10 times faster gas than Ar-CO_2. This latter gas shows a lower gas amplification threshold value. Reported ageing problems of CF_4 adds a disadvantage to its use. Both gases were tested in the Multi-Grid detector and will be studied in Chapter 7.

The main properties of radiation detectors were studied. The two main operation modes were reviewed: current and pulse mode. Detectors requirements of ToF instruments in NSS: good γ-discrimination and high time resolution, prevents the use of the current mode. The pulse one was therefore chosen.

Detection efficiency was defined. As it was seen in Chapter 1 is one of the major detector properties used to compare between different detector technologies. The definition given is used in Chapter 4 to evaluate the different MC simulations. Reducing factors of the detection efficiency such as the wall-effect and non-ionising processes were addressed. The distinction between intrinsic and absolute efficiency is made.

Dead time, related with the count rate capability, was also defined. Expressions to estimate it were obtained for both behaviours: paralysable and non-paralysable. The two behaviours can be found for the Multi-Grid detector depend on the processing electronics used.

Chapter 4

Detector Simulation

4.1 Introduction

Under perpendicular incidence of a collimated neutron beam, I_0, onto a boron-containing layer, the number of remaining neutrons at a depth x, from the converter surface follows the attenuation law seen in Equation 2.7. According to that equation, 42 μm of B_4C are needed to stop 90% of the incident neutron beam. However, the energy deposit process of the reaction fragments in the converter provoke a self-absorption phenomenon. Neutrons captured deeper than the range of the fragments will not be able to escape the layer and therefore will not be detected. The efficiency of a single mono-layer of solid converter is then limited to a few percent as it will be seen in Section 4.3.6.

In order to reach high detection performances, the boron-containing converter has to be sliced-off into thin layers. The detection process including gas ionisation and amplification and signal collection (already studied in Chapter 3) needs to be performed between the different layers. A MC simulation has been used to optimise the individual thickness of these layers in order to maximise the detection efficiency. Parameters such as the neutron wavelength, absorption in the substrate, energy deposit in the gas, the voxel geometry and the gas pressure are studied in this chapter.

A compromise between the detection efficiency and the number of layers used is needed to minimise the number of readout channels and the detector complexity. Results of the MC simulation will be used to improve the design of the Multi-Grid detector to be studied in Chapter 5.

4.2 Basics of the MC simulation

The neutron wavelength used for the MC simulation was the same that for the characterisation measurements of the detector, $\lambda = 2.5$ Å. The capture cross section becomes then $\sigma_{capt}^{^{10}B} = 5326$ barn. For the B_4C used in the Multi-Grid prototype, which will be further studied in Chapter 6, the ^{10}B atomic density was found to be $n_{^{10}B} = 1.04 \cdot 10^{23}$ cm^{-3}, which leads to a macroscopic capture cross section of $\Sigma_{capt}^{^{10}B} = n_{^{10}B} \cdot \sigma_{capt} = 5.53 \cdot 10^{-2}$ μm^{-1}.

The capture depth can be written as:

$$x = -\frac{1}{\Sigma_{capt}^{^{10}B}} \, ln\,(n_u)\,, \tag{4.1}$$

where the factor n_u is generated as a uniformly distributed number $\in$ [0,1]. x, calculated per each incident neutron, will follow an exponential attenuation as a function of the layer properties contained in $\Sigma_{capt}^{^{10}B}$. For a given set of input parameters (number of layers, individual thickness of the layers, neutron wavelength, etc.) the distance between x and the closest point to the interface converter-gas, d, is found. This is shown in Figure 4.1.

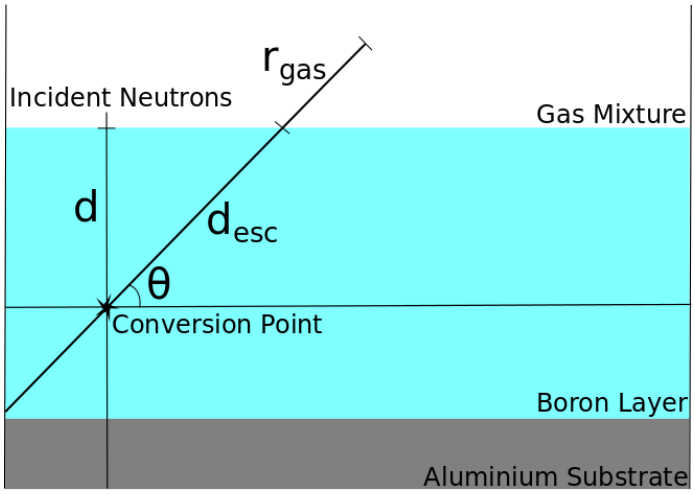

Figure 4.1: Scheme of a capture process in the MC simulation. The available energy of the reaction fragment when escapes the converter is estimated through the distance travelled in the layer, d_{esc}.

Two more random numbers are generated: θ ($\in [0, \pi]$) is the angle subtended by the reaction fragments to the layer plane and Ξ which defines the reaction branch seen in Table 2.2. Once set x and θ, the path of the fragment from the conversion point until it reaches the interface, the *escape distance*

d_{esc}, is calculated:

$$d_{esc} = \frac{d}{cos(\theta)} \tag{4.2}$$

In the thermal neutron capture reaction of ^{10}B the two subsequent fragments are emitted in opposite directions. This fact together with the multilayer structure used in the detector provokes that only one fragment per capture can be detected at most.

For the studied compound, the stopping power S (defined in Section 2.3) of the four different reaction fragments is calculated through the SRIM software [27]. The corresponding Bragg curves can be found in Figure 4.2a. For the same layer composition, S is a function of the ion energy and charge. These parameters lead to different distribution for α-particles and lithium ions.

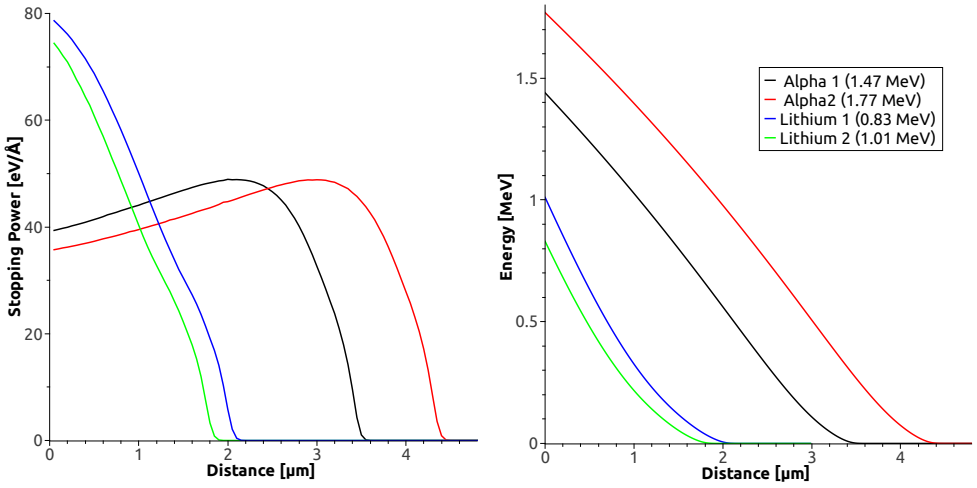

(a) (b)

Figure 4.2: **(a)** Bragg curve: the stopping power, S, as a function of the travelled distance in B_4C for the four different reaction fragments. **(b)** The available energy of the fragments as a function of the distance travelled in the layer. Maximum distances reached by each ion were defined as *range*.

The available energy of each fragment can be calculated as a function of the distance travelled in the layer and it is shown in Figure 4.2b. The maximum distance that an ion can travel was previously defined as range, r. Similar analyses have been performed for several neutron converters in [38].

During experimental tests, and to discriminate against the electronic noise, an energy threshold is usually applied. For the MC simulation this is equivalent to use shorter effective ranges. Both full and effective ranges, for an

energy threshold set at 100 keV, of the four reaction fragments can be found in Table 2.3. The choice of the energy threshold will be study in Section 4.3.5.

Particle	**Energy [MeV]**	**r$_{B_4C}$ [μm]**	**Effective-r$_{B_4C}$ [μm]**
α	1.47	3.35	3.10
	1.78	4.25	3.95
^7Li	0.84	1.70	1.35
	1.02	1.90	1.55

Table 4.1: Ranges in the layer are calculated for the four different fragments. To apply an energy threshold is equivalent to decrease the ranges. Effective ranges calculated for the threshold set at 100 keV are also shown.

The MC simulation uses the escape distance, d_{esc}, previously calculated per each capture event and computes the remaining energy at the converter-gas interface using the information shown in Figure 4.2b. The available energy per each fragment is found.

As seen in Chapter 2, the principal process by which the energy of the reaction fragments is deposited in the gas is the ionisation. This ion-matter interaction can also be simulated with SRIM. The stopping power of the most energetic fragments of the neutron capture reaction in the gas are shown in Figure 4.3a. Alternatively their available energy as a function of the travelled distance can be found in Figure 4.3b. The much lower density of the gas mixture (CF_4 @ 1 bar) compare to B_4C, explains the much longer ranges found in this case. For both ions, they are shown in Table 4.2.

Particle	**Energy [MeV]**	**r_{gas} [mm]**	**Effective-r_{gas} [mm]**
α	1.78	3.92	3.77
^7Li	1.02	2.03	1.55

Table 4.2: For the most energetic fragments ranges in the gas are shown for CF_4 @ 1 bar. As seen before, to apply an energy threshold is equivalent to use a shorter effective range.

Three important parameters can be accessed with the MC simulation:

- The **Conversion Efficiency** is defined as the number of capture interactions within the Multi-Grid detector divided by the total number of incident neutrons. It can be directly calculated from the attenuation law.
- The **Detection Efficiency**, already studied in Section 3.4, is defined as the number of reaction fragments that deposit in the gas an energy higher than the threshold divided by the total number of incident neutrons.

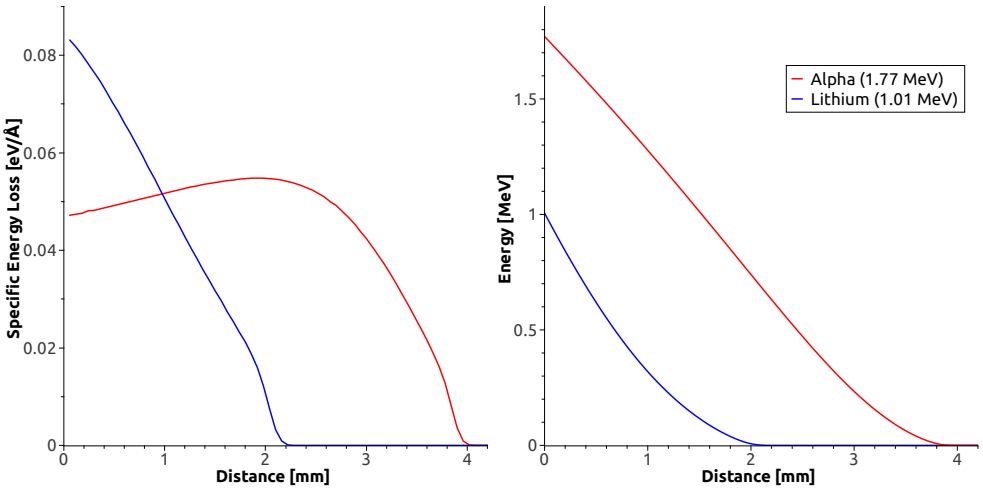

(a) (b)

Figure 4.3: **(a)** Bragg curves: S, for the most energetic fragments (lithium 1.01 MeV and α-particle 1.77 MeV) along their track in CF_4 @ 1 bar. **(b)** The available energy of the fragments as a function of the travelled distance in the gas.

- The **Escape Efficiency** is defined as the number of reaction fragments able to escape the converter over the total number of incoming neutrons.

4.2.1 Limits of the Simulation

The MC simulation previously described is a useful tool used to optimise several parameters of the Multi-Grid design. However, it is not a complete representation of a real detector. Its limitations need to be known and understood.

- **2D Simulation** Although the neutron capture process and the subsequently tracks of the reaction fragments are three-dimensional processes, in the MC simulation a simplified geometry was chosen. The track of the fragments is calculated in 2D using the angle θ.
- **Dead Zones** The detection efficiency values calculated in almost all the results of the MC simulation are intrinsic [26]: they are estimated at the middle of a voxel. In the case of the wall-effect several points along one axis are studied. Finally, when studying the effect of the gas pressure in the detection efficiency (in Figure 4.16) an integration along the length of the voxel is done.
- **Scattering in Aluminium** Due to the low neutron σ_{scat} of ^{10}B compared to σ_{capt} ($\sigma_{capt}^{^{10}B}/\sigma_{scat}^{^{10}B} > 10^3$), this interaction was ignored. Capture

and scattering processes occurring in aluminium were however, taken into account. The entrance window and the substrates, used to support the boron coating, constitute a non-negligible contribution to the attenuation within the Multi-Grid detector ($\sim 6\%$ drop at the maximum of the detection efficiency for a 30-layer detector as it will be shown in Section 4.3.3).

Neutrons interacting in aluminium, either scattered or captured, are considered to be lost for the efficiency calculations. Scattered neutrons however have a chance to be detected elsewhere in the detector increasing the neutron background.

- **Aluminium Impurities** The interactions with other elements present in the aluminium alloy used (AL5083) could be important. High concentration (4 - 4.9%) of manganese together with its relatively high σ_{tot} for thermal neutrons (two times larger than $\sigma_{tot}^{^{27}Al}$) might induce a non-negligible effect.

4.2.2 The Mono-Layer Approach

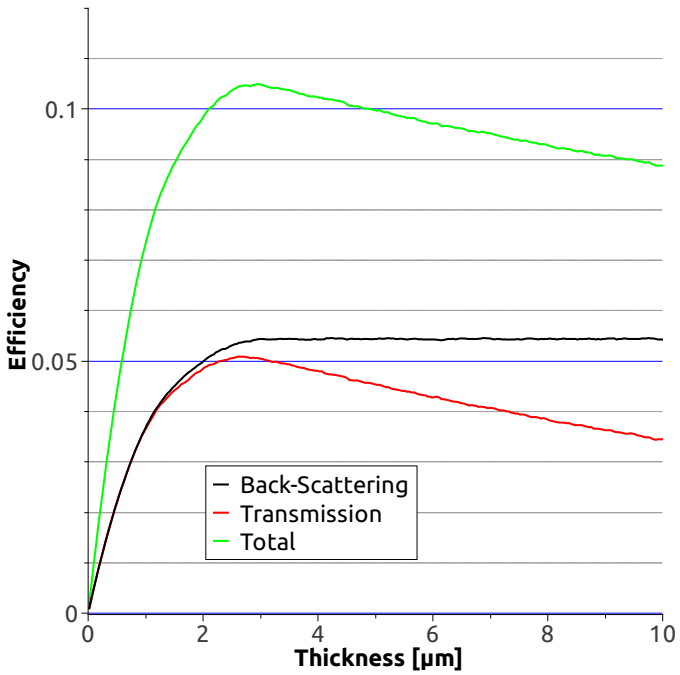

Figure 4.4: Detection efficiency for a mono-layer as a function of the layer thickness. Two different modes can be defined according to the side of the converter from which reaction fragments escape: transmission and back-scattering.

As previously said, if only one single layer is used a relatively low detection efficiency is reached. This is illustrated in Figure 4.4. Detection efficiencies are shown for a mono-layer detector as a function of its thickness. Usual simulation parameters are used: $\lambda = 2.5$ Å and 100 keV energy threshold.

Two different modes can be defined: transmission or back-scattering [11]. In the transmission mode, the escaping fragment leaves the coating on the opposite side that the incoming neutron, as is shown in Figure 4.5a. The optimisation of the thickness takes into account the number of neutrons converted in the layer too deep for the reaction fragments to escape. An optimum value is found at d ≈ 2.70 μm. Beyond that value the efficiency slowly decreases. A larger number of neutron is captured but reaction fragments are created further from the surface and have therefore a lower escape probability.

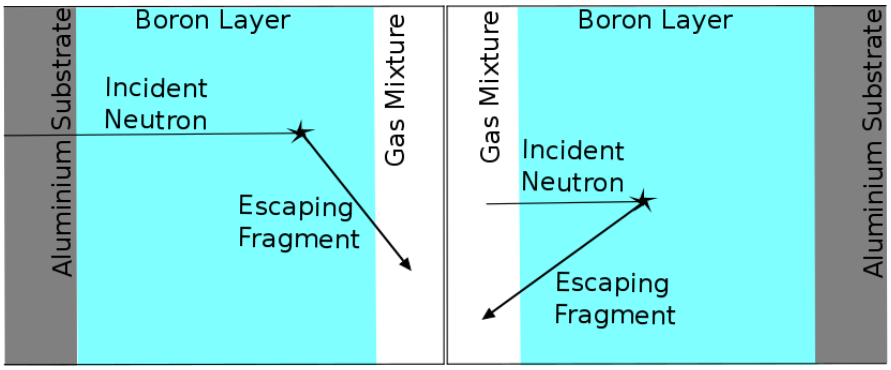

Figure 4.5: **(a)** Scheme of a mono-layer detector in transmission mode. Reaction fragments escape the converter on the opposite side of the incoming neutron. **(b)** In the back-scattering mode, reaction fragments leave the converter on the same side that incoming neutrons.

In the back-scattering mode, the reaction fragment escapes the layer from the same side that the incoming neutron as shown in Figure 4.5b. In this case a saturation region is reached at d ≈ 3.10 μm and beyond that point it remains stable. This is explain as follows. For a thin layer almost every neutron captured creates a reaction fragment that reaches the stopping gas. The number of capture events is however small. When the thickness is increased more neutrons are converted. Some fragments will not reach the gas because they were created too deep in the converter. If the layer thickness is further increased more neutrons will be converted deeper in the layer but they will not reach the gas. No further increment in the detection efficiency is produced.

4.3 The Boron Converters

A thin film characterisation, to be discussed in Chapter 6, was performed on the boron layers. Three are the main properties to be used as input parameters for the MC simulation:

- The film mass density, $\rho_{film} = 2.242$ g/cm^3.
- The ^{10}B atomic density $n_{^{10}B} = 1.04 \cdot 10^{23}$ cm^{-3}.
- The atomic concentration of each element present in the film (shown in Table 6.1).

4.3.1 Number of Layers

For the specific film composition, detection efficiency is shown as a function of the number of boron layers in Figure 4.6. d_{opt} is defined as the layer thickness that optimises the detection efficiency for a given number of layers. For $\lambda = 2.5$ Å, d_{opt} varies from 2.70 μm for a mono-layer detector in transmission mode to 0.69 μm for a 100-layer detector.

The detection efficiency rapidly increases with the number of layers. 30 are needed for a 53.47% efficiency. Above 50 layers the increment slows down and a 69.96% efficiency is reached for 100 layers. As a compromise between detection efficiency and complexity for a practical mechanical construction a design with 30 layers was chosen. The corresponding d_{opt} was found to be $\approx$ 1.0 μm.

A detection profile for a 30-layer detector (all with the same thickness, 1 μm) was simulated and it is shown in Figure 4.7a. The exponential attenuation of the neutron flux is found.

A possible improvement consists on varying the individual thickness of the coating depending on its position within the detector. This is done as follows. The thickness of the last layer is arbitrary fixed in a relatively thick value (10 μm). Since it is a layer working in the back-scattering mode only, the maximum efficiency is reached at 3.10 μm as seen above. However a thicker value was chosen to stop neutrons not converted in the rest of the detector. Another layer is added before the last one. Its thickness is calculated by iteration until a maximum in the total detection efficiency is found. With the thickness of these two layers fixed the process is repeated for every layer optimising the efficiency at each step. This results in a configuration with thinner layers at the front of the detector and thicker layers at the back. The structure of this detector is shown in Figure 4.7b. The detection profile in this case follows a linear

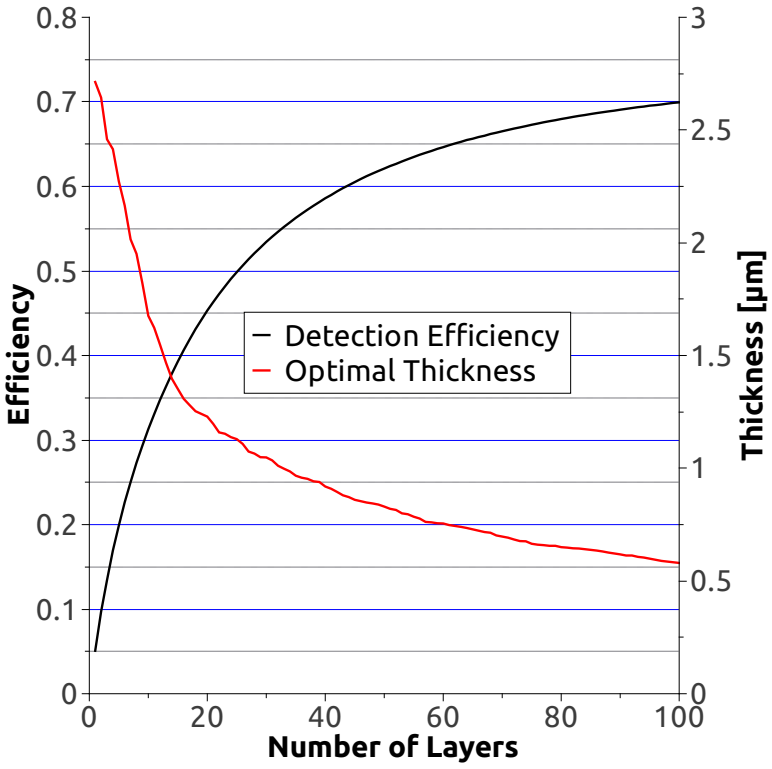

Figure 4.6: Detection efficiency as a function of the number of layers for $\lambda = 2.5$ Å. d_{opt} was calculated and the detection efficiency optimised per each number of layers. For 30 layers an efficiency of 53.47% is reached. At this value d_{opt} was found to be ≈ 1 μm.

relation with the detector depth. The detection efficiency calculated applying this design was found to be 1.51% higher than in the previous configuration (54.98% for 30-layer detector at $\lambda = 2.5$ Å). Its implementation however would increase the complexity of the coating and mounting.

4.3.2 Neutron Wavelength

The dependence of $\sigma_{capt}^{^{10}B}$ and $\sigma_{tot}^{^{27}Al}$ with the energy of the incoming neutrons was shown in Figures 2.1 and 2.2 respectively. This variation is applied to the MC simulation when working at different wavelengths. Previous results were calculated for a neutron wavelength of $\lambda = 2.5$ Å. However, different optimisation values for the detection efficiency and optimal layer thickness are found for different wavelengths. This is shown in Figure 4.8 where only the number of layers, N = 30, and the energy threshold, set at 100 keV, were fixed.

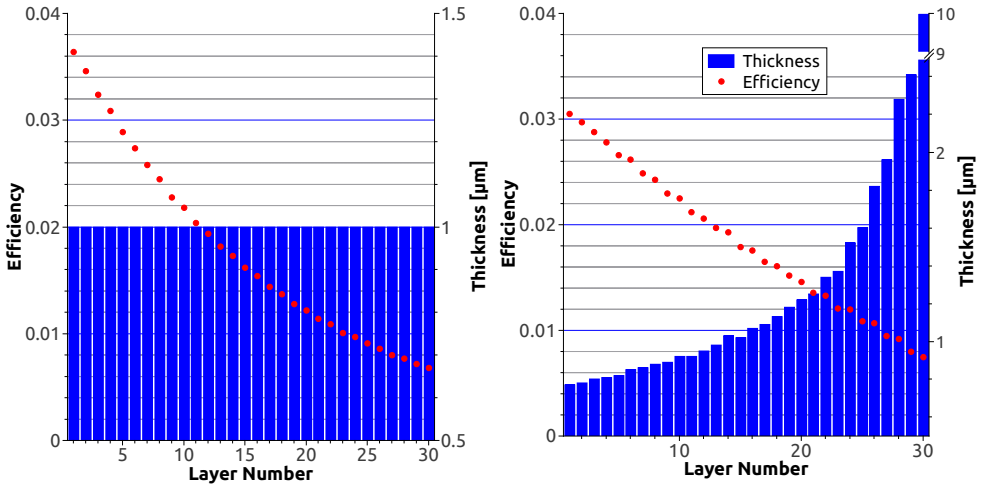

(a) (b)

Figure 4.7: **(a)** The individual layer thickness, 1 μm, and the detection profile simulated for a 30-layer detector. **(b)** When an optimisation is performed in the layer thickness as a function of its position in the detector a slightly higher efficiency (+ 1.51%) is reached.

A longer wavelength implies higher chances of interaction. In the case of the aluminium, the greater lost is mainly localised in the frontal window. As a result of this interaction, the detection efficiency slowly decreases for large values of λ. A stable behaviour is found between λ = 6.6 and 16.3 Å where the detection efficiency is found to be 68.25% $\pm$ 1%.

4.3.3 Thickness of the Layer

For a fixed number of layers, N = 30, and incoming neutron wavelength, λ = 2.5 Å, the conversion efficiency is shown as a function of the individual thickness of the boron layers in Figure 4.9. Together with it, the detection efficiency is calculated for a energy threshold set at 100 keV.

Detection efficiency shows a well defined maximum. The optimal value is found at 1.0 μm. Small variations around the optimal value of the thickness lead to a drop in the total detection efficiency. Thickness deviations in a range going from 0.7 to 1.5 μm would induce a maximum drop in the detection efficiency of 3.5%. For this range however, an efficiency higher than 50% is always reached.

The previously defined escape efficiency is also calculated. For thin layers it reaches high values. As an example, the value at 1.0 μm was found to be

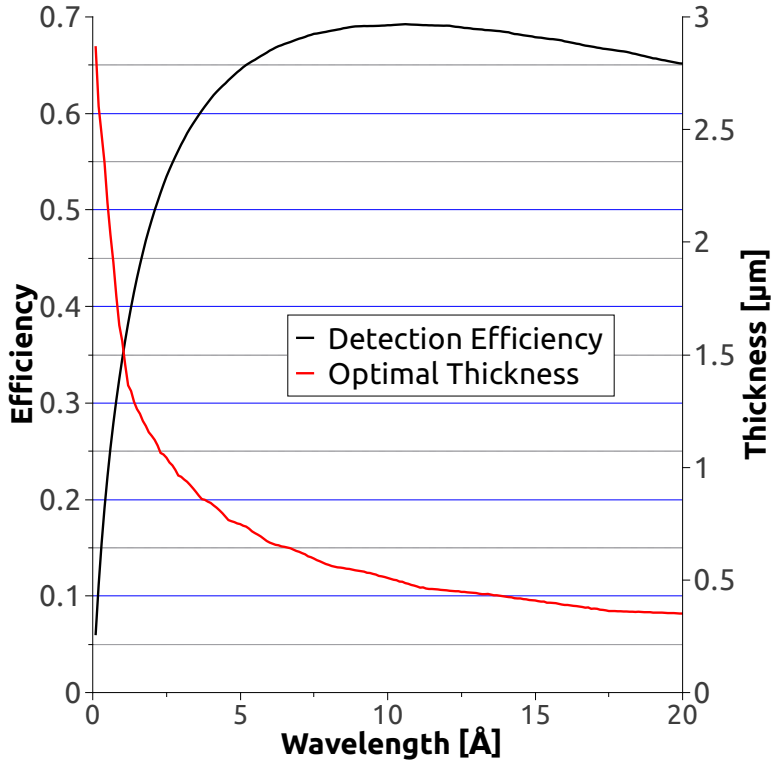

Figure 4.8: Detection efficiency and optimal layer thickness as a function of the neutron wavelength. N = 30 layers and the energy threshold was set in 100 keV. For these range of values, $\sigma_{capt}^{^{10}B}$ linearly increases with λ.

71%. When thicker layers are used the number of reaction fragments escaping the layer decreases. This effect provokes a continuous reduction of the escape efficiency.

The relatively high mass density of the aluminium: $\rho_{Al} = 2.7$ g/cm^3, together with the thickness of the entrance window (≈ 6 mm) and the different substrates (16×0.5 mm $= 8$ mm) contributes to the neutron beam attenuation. In order to show its importance, the detection efficiency is shown for a MC simulation in which neutron interaction with aluminium is ignored. The total detection efficiency found for a 30-layer detector at the optimal thickness rises from 53.5% to 59.2%. For this value of the neutron wavelength, the ratio between capture and total interaction in aluminium is calculated: $\sigma_{capt}^{^{27}Al}/\sigma_{tot}^{^{27}Al}$ $\sim 9\%$. The major part of the interaction is thus scattering.

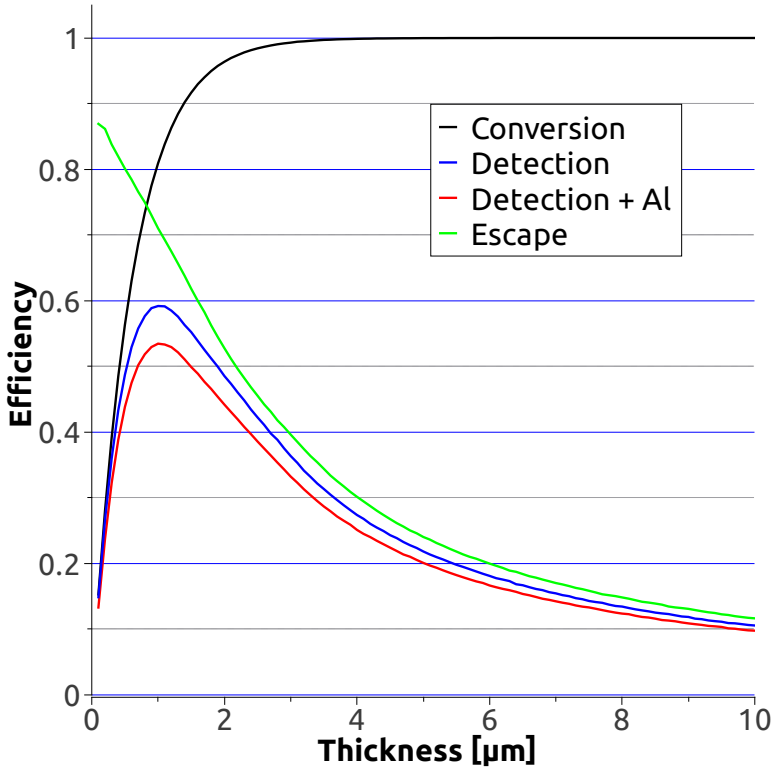

Figure 4.9: Conversion efficiency as a function of the layer thickness for a 30-layer detector. Detection efficiency, for an energy threshold of 100 keV is also shown. Escape efficiency and detection efficiency without the contribution of aluminium are also shown.

4.3.4 Pulse Height Spectra

To study the effect of the energy loss within the converter the PHS can be simulated. The number of boron-containing layers was set in N = 30 and the wavelength is $\lambda = 2.5$ Å. Different layer thickness's were studied. Results are shown in Figure 4.10.

The available energy of the reaction fragments depends on their initial energies, seen in Table 2.3, and the distance that they have travelled in the conversion layer, d_{esc}. This latter factor is a function of both d and θ. Varying the layer thickness yields different PHS. For thin layers, e.g. 0.1 μm, a small amount of energy is lost in the converter. The distributions of the four different fragments are visible. A more convenient γ-discrimination could be set due to a clear energy separation. When increasing the thickness, to 1.0 μm for instance, the energy loss within the layer become important. A significant

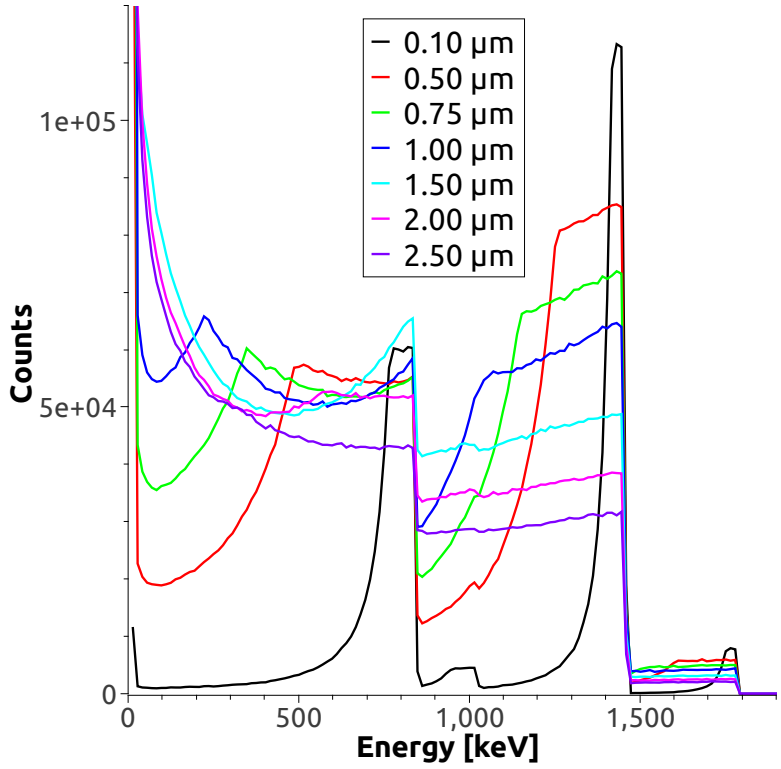

Figure 4.10: PHSs for a 30-layer detector using different thickness's. An important spread in energy is found for thick layers.

spread on the energy distribution is found due to the longer tracks that the reaction fragments have to travel inside the coating. The maximum value for each distribution remain at the same energy corresponding with the most energetic of the 4 fragments (α-particle of 1.78 MeV) and emitted directly on the interface converter-gas. A higher number of neutrons is converted and can escape the layer: we are placed at the maximum of the efficiency distribution seen in Figure 4.9. When a thicker layer is used ($\geq$ 1.5 μm), the ratio between events produced deep in the layer to those produced close to the surface gets higher and the energy distribution is further spread. For these values of the layer thickness, the detection efficiency, defined here as the integral under the curves, is already lower than for 1 μm.

4.3.5 Threshold Cut-Off

As seen in Section 4.3.4, due to the self-absorbing phenomenon in the film the escaping reaction fragments show a continuous distribution in energy. If a high

γ-rejection is to be set, a lower efficiency is expected. This drop in efficiency depends on the threshold value. This effect was simulated and it is shown in Figure 4.11 for a 30-layer detector and $\lambda = 2.5$ Å.

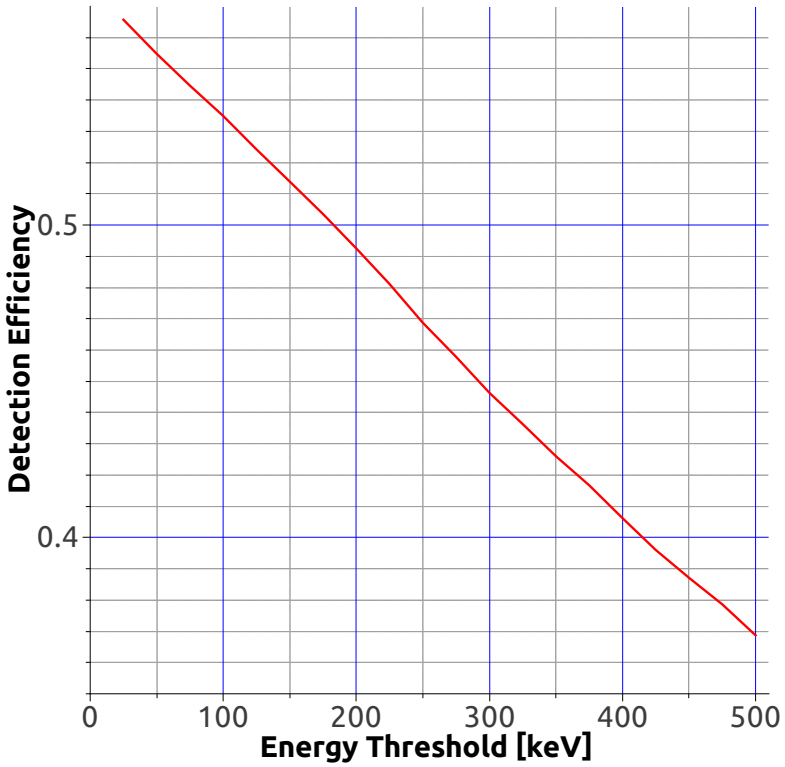

Figure 4.11: Detection efficiency vs. energy threshold for a 30-layers detector.

An almost linear behaviour of the detection efficiency as a function of the threshold value was found for an energy range of 10 - 500 keV. The 50% efficiency was crossed for a threshold value of 175 keV. As previously said, the chosen value for the energy threshold was set at 100 keV. This value corresponds to 1.5 times the electronic peak level for a standard detection efficiency measurement, to be discussed in Section 7.3. When compared to a PHS, as the one seen in Section 1.4.3, the cut-off was found to be at 100 keV.

4.3.6 Other Converters

Two other solid converters were studied and compared to ^{10}B. The same MC simulation was used. Densities and capture cross sections of new converters were introduced as inputs. SRIM values on the linear stopping power were calculated for the new materials: lithium and uranium.

Lithium One of the most common lithium-containing compounds used in neutron detection is the Lithium Fluoride which has a mass density of $\rho = 2.635$ g/cm^3, 5 times higher than pure lithium. A 100% isotopic enrichment in ^{6}Li was considered.

The efficiency of a multi-layer detector as a function of the number of layers is shown in Figure 4.12. In the same way that for boron, the optimal thickness used to calculate the efficiency at each step is also shown. Wavelength used was $\lambda = 2.5$ Å.

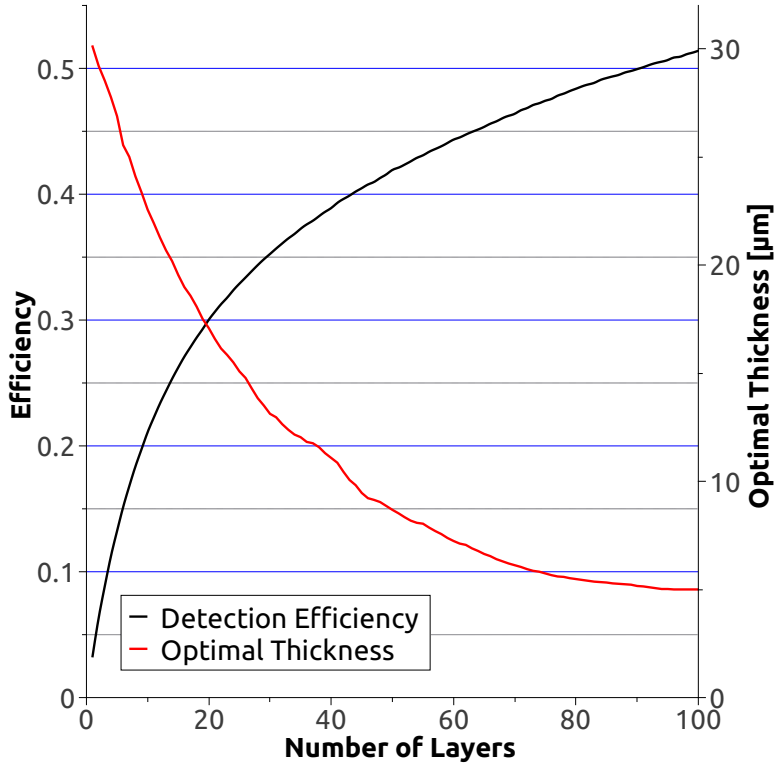

Figure 4.12: The detection efficiency of a lithium-based multi-layer detector is shown. d_{opt}, calculated for each number of layers, is also plotted.

Detection efficiency shows a similar behaviour than for a boron-based converter. For a 30-layer detector the value was found to be 35.25% which is 34.01% lower than B_4C. For $\lambda = 2.5$ Å, 91 layers are needed to reach a 50% efficiency.

Optimal values of the individual layer thickness are thicker than in the previous case. 13.12 μm and 5.0 μm layer thickness optimise the efficiency for a 30 and 100-layer detector respectively.

Detectors made of thin foils of pure lithium have been already used in a MWPC showing a relatively high efficiency [39]. However, problems handing this element prevents its use for LANDs.

Uranium In this case, a typical uranium-containing compound was used as the converter: UO_2. As input parameters a 100% isotopic enrichment and $\rho = 10.97$ g/cm^3 for the mass density were considered. The two fission fragments used were Barium (79 MeV) and Krypton (111 MeV). Results can be found in Figure 4.13.

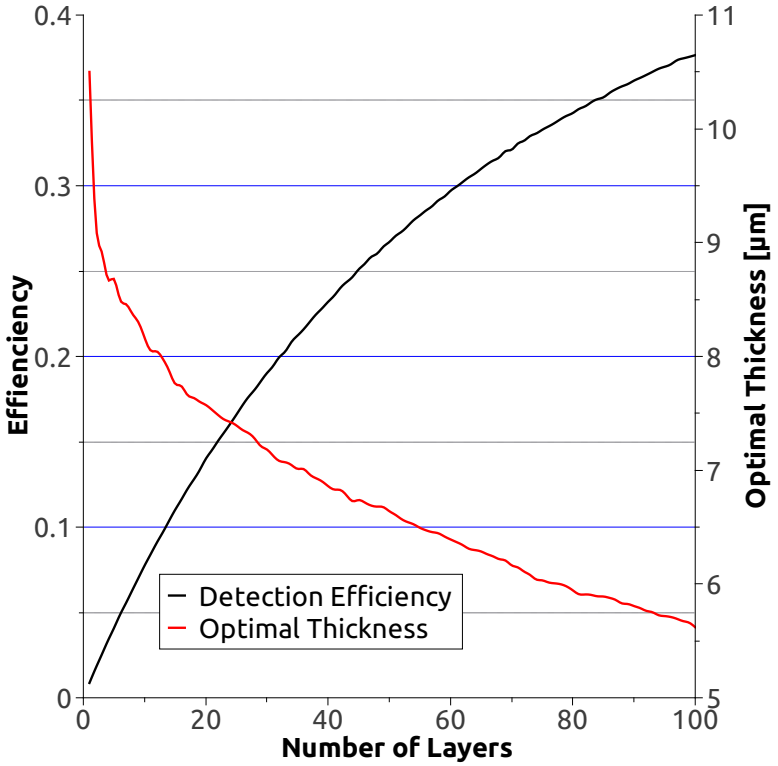

Figure 4.13: The detection efficiency of a uranium-based multi-layer detector is shown.

A lower detection efficiency was found in this case. A value of 19.02% was reached for a 30-layer detector. As seen before, increasing the number of layers implies higher efficiencies. However only a 37.65% was reached with 100 layers. As it was seen in Section 2.2.1, uranium-based neutron detectors are mainly used for beam-monitoring. The values of the optimal thickness move from 7.18 μm to 5.62 μm for 30 and 100 layers respectively.

4.4 Detector Geometry

The ionisation process in the gas due to the escaping reaction fragments is stopped when fragments collide with one of the walls of the voxel. If the energy deposited in the gas did not reach the threshold value the event will not be recorded. This is known as the *wall-effect* and strongly depends on two parameters: the geometry of the voxel and the pressure and composition of the gas.

4.4.1 Geometry of the Voxel

Properties of the Multi-Grid voxel will be fully discussed in Chapter 5. Dimensions however are given here for a better understanding of this effect. They are 2 cm $\times$ 1 cm $\times$ 1 cm. The maximum track length of the reaction fragments were shown in Table 4.2. For CF_4 @ 1 bar they are approximately 2 and 4 mm respectively. Under these conditions, collisions will only be possible with side-walls and therefore close to the corners.

The wall-effect can be estimated by simulating a collimated neutron beam while scanning the X-axis of the voxel. For a 30-layer detector different PHS as a function of the distance to the wall are shown in Figure 4.14.

The PHS distributions change when the collimated beam approaches the wall. High energy fragments are the first to collide with the wall due to their longer track. For events produced directly at the corner, the PHS has the same distribution that the one produced in the middle of the cell but just half the number of counts. Only fragments escaping this point towards the centre of the cell can be measured, the rest are lost.

Detection efficiency is computed along the X-axis and it is shown in Figure 4.15. As seen above, the changes in the PHS start at distances to the wall shorter than the maximal track length. The detection efficiency however is not modified until a distance $\approx$ 1 mm when it starts dropping. At the corner of the voxel it has a value corresponding to half its value at the center of the cell. This can be explained by looking at the PHS in Figure 4.14. The distributions below the applied threshold value (set at 100 keV) do not change for distances further than 1 mm. No neutron events are lost under these conditions. When the beam is closer to the wall than this distance more events of the energy distributions cross the energy threshold lowering the counting which leads to a lower efficiency. This effect results in a 2.54% drop in the efficiency when integrating along the length of the voxel. A value of 50.93% for the absolute efficiency is found.

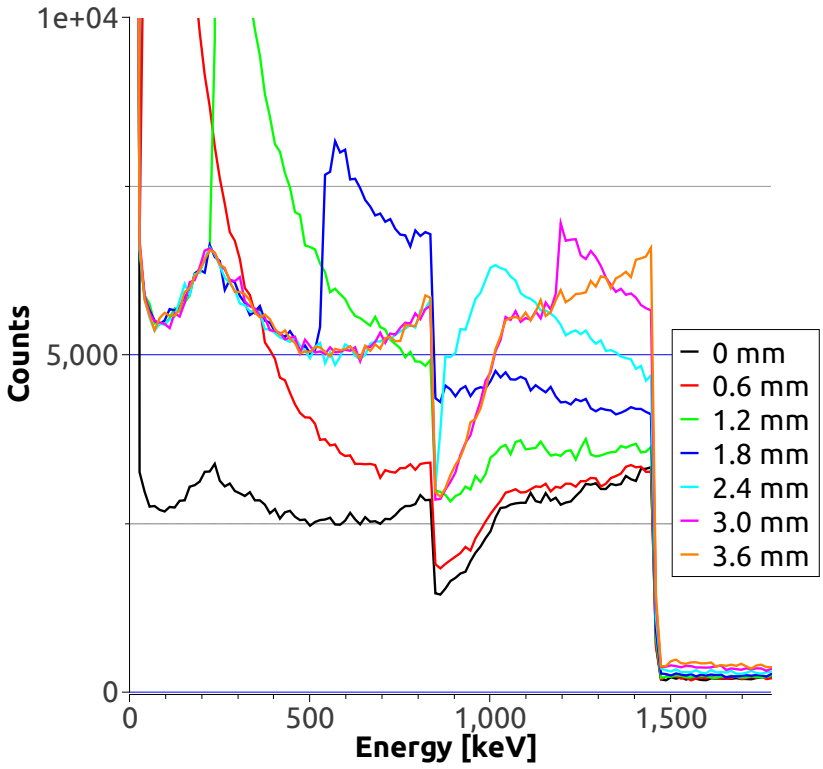

Figure 4.14: PHS for different positions of the collimated beam along the X-axis of the voxel. A shift in the distribution towards lower energies can be seen when approaching the wall. At the corner the PHS has the same distribution but half the number of counts than in the middle of the voxel.

4.4.2 Pressure

The range of the reaction fragments in the gas linearly scales with the pressure. The use of similar pressures in the detector than in the environment where it is to be installed is preferred. If a lower pressure difference is to be maintain, thinner walls can be used. This will reduce the neutron scattering background and maximise the detection efficiency. As seen in Section 1.2.1, the IN5 chamber is which the PSDs are placed is in vacuum. Lower pressures than atmospheric are therefore more suitable. An analysis of the detection efficiency as a function of the gas pressure is presented in Figure 4.16.

For low pressures the wall effect, already discussed above, becomes important. Due to the longer tracks of the fission fragments encounters with all the walls are possible. Low values of detection efficiencies are found in this region. There is a value of the gas pressure around 50 mbar from which the efficiency

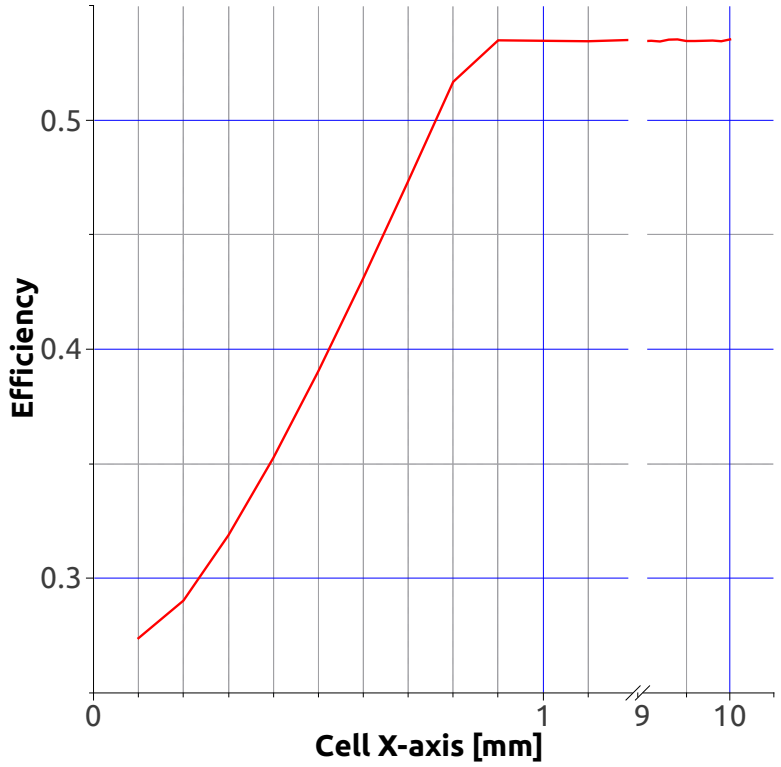

Figure 4.15: The wall-effect decreases by half the efficiency at the corners of the cell. The overall efficiency is 2.54% lower than the intrinsic when integrated along the X-axis.

dramatically raises. This pressure corresponds with a certain track length of the reaction fragments which allow them to deposit an energy in the gas higher than the energy threshold. Beyond this point the detection efficiency continues to increase and it reaches the 50.93% @ 1 bar. This value corresponds to the absolute detection efficiency already discussed in Section 4.3.1 but integrated along the X-axis of the voxel.

4.5 Conclusion

The basics elements of the MC simulation were studied. Special attention was paid to its limitations. Rather than a complete detector simulation it is more an optimisation study of several parameters of the Multi-Grid detector design, specially the optimal layer thickness.

A mono-layer approach was first studied. Maximum efficiencies for B_4C

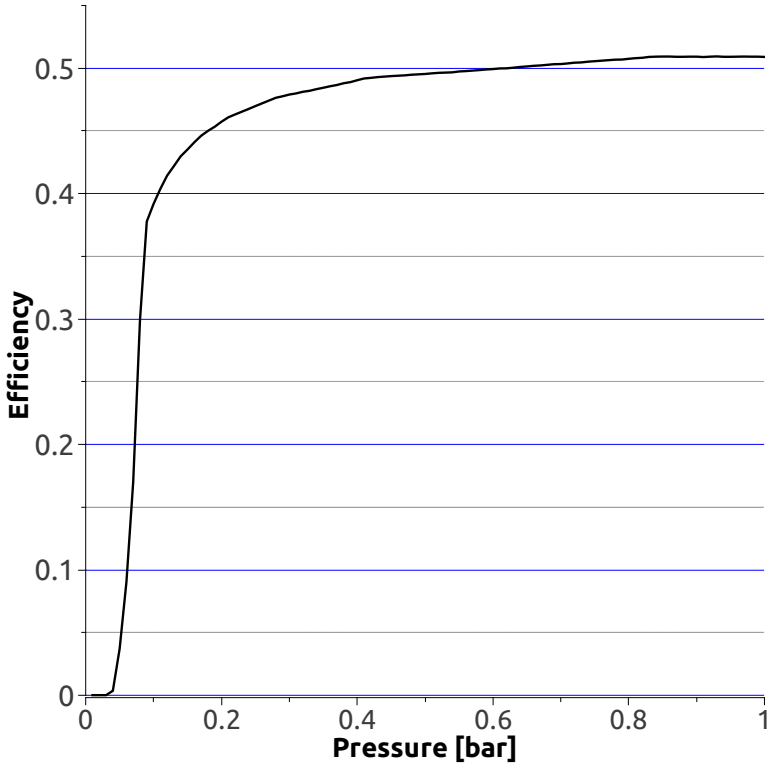

Figure 4.16: The absolute detection efficiency as a function of the gas pressure is shown. Decreasing the pressure leads to longer track lengths of the fragments and therefore a more important wall effect.

were found to be far from detector requirements discussed in Chapter 1. Typical solid converters in radiation detection were also simulated: Lithium Fluoride and UO_2. Enriched B_4C was chosen due to its higher detection performances and other properties to be studied in Chapter 6. A detection efficiency higher than 50% can be reached with a 30-layer configuration. The individual thickness that optimises the efficiency for this number of layers was found to be ≈ 1.0 μm.

The interaction of neutrons in aluminium has been studied and causes a drop in the detection efficiency of $\approx 6\%$ at its maximum. Minimising the use of this element would increase the detector performance. Special attention needs to be paid to the scattering interaction, that represents $\sim 90\%$ of the total interaction, which can provoke and increment in the neutron background within the detector.

As a consequence of higher interaction probabilities for longer wavelengths a higher detection efficiency was found for high values of λ. Interaction in the

aluminium however starts reducing the efficiency when λ reaches 15 Å.

The wall-effect was analysed. It depends on the length of the reaction fragment tracks. Therefore, it varies with the gas species and its pressure. For CF_4 @ 1 bar, the absolute efficiency was estimated in 50.93% over the length of the Multi-Grid detector voxel. If lower pressures are used longer tracks, and therefore larger wall-effect, is expected.

Chapter 5

Multi-Grid Detector

5.1 Introduction

Principal requirements of a detector for a ToF instrument in NSS were described in Section 1.2.1. The coverage of tenths of m^2 active areas at relatively high efficiencies (80% at 5 Å) is needed. The ^{3}He shortage, studied in Section 1.3, requires the development of a new technique based on alternatives neutron converters.

Results of the MC simulation studied in Chapter 4 have optimised a few important parameters for the design of a neutron detector based on $^{10}B_4C$ converters. The Multi-Grid concept is introduced in Section 5.2. For incoming neutrons of $\lambda = 2.5$ Å and using $^{10}B_4C$ as the converter, 30 layers are needed to reach a 53.47% detection efficiency. The optimal individual layer thickness was found to be ≈ 1.0 μm.

Different detector prototypes were designed and built during this study. Specifications of each one of them (size, number of readout channels, etc.) are reviewed in Section 5.3.

The front-end electronic system used for the Multi-Grid detector is explained in Section 5.4. A possible improvement of the counting rate capability by reducing the detector dead time is explained. Different methods used to reduce the number of readout channels are reviewed. The Centre-of-Gravity (CoG) algorithm used to improve the spatial resolution is studied.

5.2 Concept

The Multi-Grid detector is formed by several layers of rectangular counter tubes with neutron converter coated on the inner side. Counters are made of juxtaposed sections, called grids. The most important advantages of the Multi-Grid design are listed below.

- It matches the requirements of ToF instruments: large active areas (tenths of m^2) and relatively low spatial resolution (2 cm $\times$ 2 cm).
- It allows to achieve high coating uniformity inside relatively long ($\geq$ 2 m) tubes in a simple way.
- The readout method is well adapted to achieve good position and time resolution.

The detector is composed of a gas vessel filled with grids electrically insulated one from another and stacked to make rectangular counters [40]. Each grid is made of a frame in which blades coated with a neutron converter film, are inserted. Both the frame and the blades are made of aluminium which has a low cross section for thermal neutrons as it was shown in Section 2.2. A grid filled with coated blades is shown in Figure 5.1.

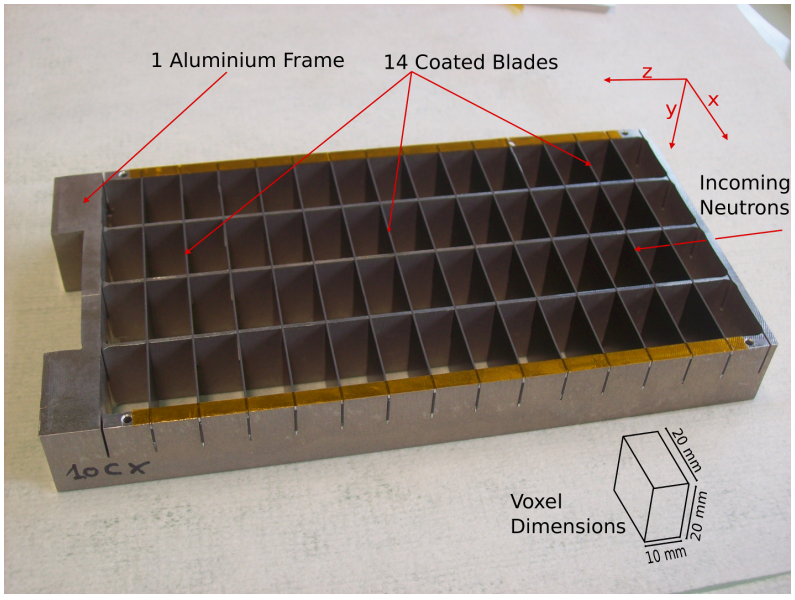

Figure 5.1: One grid once filled with 14 coated aluminium blades. The dimensions of the voxel are also presented.

Blades are placed 1 cm away from each other which defines the depth of the rectangular tubes. As it was shown in Chapter 1, the time resolution of the detector is related with the depth of the tubes. In the case of the Multi-Grid a 40% thinner tube depth is used compared to the present IN5 PSD. A higher detector time resolution can therefore be achieved if needed.

If an individual readout system is implemented, the position resolution will be defined by the voxel dimensions: 2 cm × 2 cm × 1 cm. The achieved pixel-size is therefore 2 cm × 2 cm. This value is smaller than for the present IN5 PSD (2.5 cm × 2.5 cm).

Grids are biased at 0 V. Each counter has a wire centred in it, biased at positive high voltage to amplify the signal of the primary charge. The resulting signal generated on the anode wires and on the cathode grids is read out either individually or via a resistive network. As a trade off between position and time resolution needed and number of readout channels, it is possible to connect several anode wires together, as well as several cathode grids together.

The grids are inserted in an aluminium vessel which is closed by a flange to contain the stopping gas. The flange is equipped with gas-tight feed-through for signal readout. The front-end electronics is mounted outside the gas vessel. By flushing the gas in the detector vessel continuously, it is possible to use materials without out-gassing constraints, making the production of gas-based LANDs economically viable.

5.2.1 Dead Zones

As seen in Section 3.4.2, dead zones on a detector active area decrease the absolute efficiency. In order to reduce these zones, the distance between grids needs to be minimise. This is achieved by the use of 0.5 mm thick Teflon spacers. The close packing of the grids can however provoke two undesired effects: short circuits and capacitive coupling.

- In the first case, the presence of a relatively small conducting speck of dust could short-circuited two of the grids with the lost of these two channels as a consequence. Controlled environments during the mounting are needed to minimise this risk.
- The second effect is the capacitive coupling between two grids when one of them is fired, and therefore charged, compared to the other. This coupling generates cross-talk between grids. When an event is produced in a grid, signals in the neighbouring grids can be measured. This effect will be further studied in Section 7.2.2. This phenomenon will make more complicated to readout real induction signals at neighbouring grids. This

idea, to be further studied in Section 7.2.2, could be used to increase the position resolution of the Multi-Grid detector along the direction of the wires.

For the MG-IN6 detector, to be studied in Section 5.3.3, the angular dead zones between the columns of the need to be taken into account for absolute efficiency calculations. If the total active area of the detector (1382,4 cm^2) is divided by the total coverage (1588 cm^2) the percentage total coverage area that can be accessed is found to be 87.5%. The major part of this loss ($\approx$ a 75%) is due to the relatively thick external walls of the grids. Further designs need to take the dead zones into account and minimise the walls thickness to increase absolute efficiency.

5.3 Prototypes

The different Multi-Grid prototypes designed are described individually in this section. Each detector was conceived for a particular set of experiments which is also recalled. The characterisation presented in Chapter 7 is based on results of prototypes MG-12 and MG-96.

5.3.1 MG-12

Grids were mounted using coated aluminium blades as described above. For this particular detector 12 grids were employed. Thirty $^{10}B_4C$ layers were used: 14 double-side coated blades and 2 (corresponding to the first and last slits in Figure 5.1) single-coated blades were inserted in each aluminium frame. Different film thickness were used in different grids. The coating thickness of each specific grid is shown in Table 5.1.

Grid Number	G1 - G6	G7	G8	G9	G10	G11	G12
Thickness [μm]	1.0	0.0	0.5	0.75	1.5	2.0	2.5

Table 5.1: Different thickness's used in the MG-12. 6 grids using 1 μm-thick coating and 5 grids using different coating thickness were separated by a blank grid (filled with uncoated blades).

The MG-12 detector is shown in Figure 5.2. Two types of Kapton circuits were used. The first one is placed underneath the grids and it keeps them electrically insulated from each other and from the aluminium back-bone used to hold the structure. The second one is place at the end of each row of wires

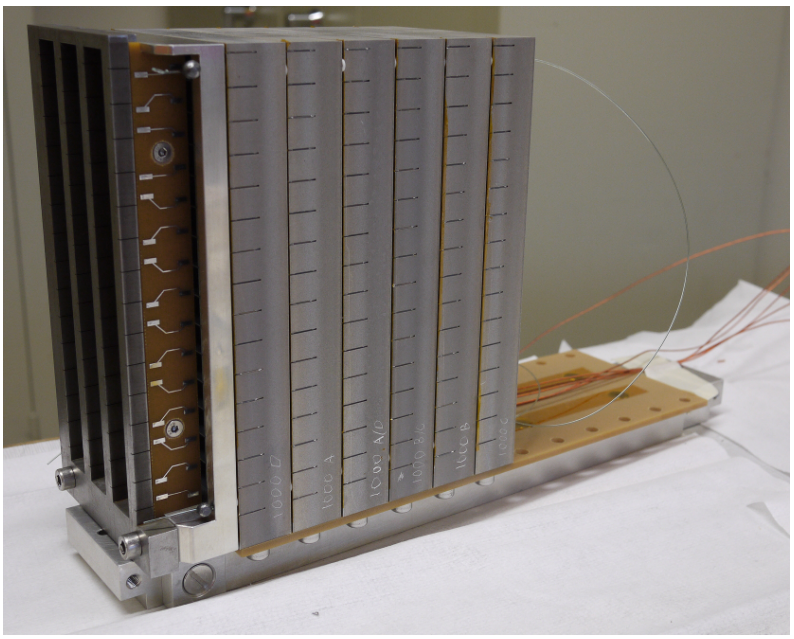

Figure 5.2: Mounting of the MG-12 detector. The two types of Kapton circuits used can be seen: underneath the grids and on the left end of the detector.

to which they are connected. Readout cables are connected from this circuit to the feed-through.

A total of 72 signals are read out in this detector: 60 corresponding to each anode wire (4 rows $\times$ 15 wires each) and 12 to each grid. Individual readout was implemented in this detector.

Cross-talk and wall-effect, efficiency measurements, stability and ageing for different stopping gases, among some other test were performed with this prototype.

5.3.2 MG-96

To verify parameters such as the mechanical mounting for large scale detectors or the detection efficiency uniformity, a larger detector than MG-12 was needed. A longer version of the Multi-Grid concept was designed and built: the MG-96 (shown in Figure 5.3). Together with it γ-sensitivity measurements were performed with this prototype. As it was shown for MG-12, grids are stacked one after the other forming rectangular tubes. In this case, 96 grids were used achieving a detection active area of 8 cm $\times$ 200 cm.

Twenty eight layers were used in this prototype which implies that more

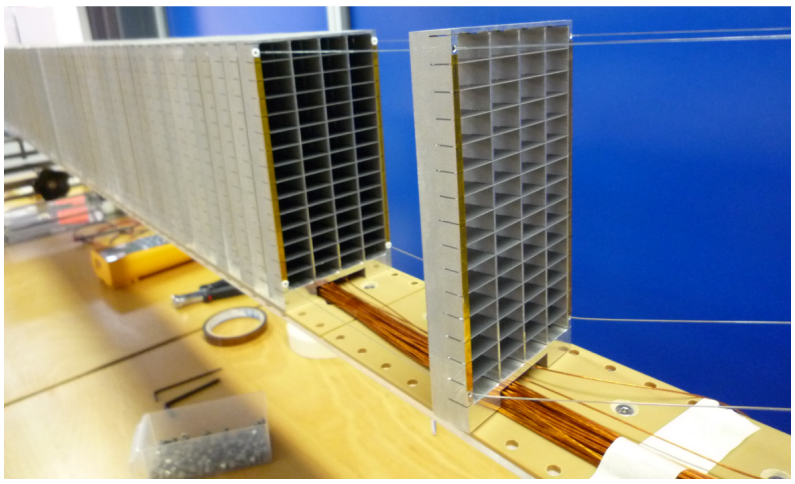

Figure 5.3: Grids of the MG-96 detector during mounting. Teflon spacers 0.5 mm thick, used to keep constant the distance between grids and avoid any short-circuit, are place at the corners of the grids.

than 4.3 m^2 of ^{10}B-enriched B_4C film was coated onto 1344 double-side aluminium blades. As shown in Section 4.3.3, 1.0 μm was found to be the thickness that maximises the detection efficiency. Small variations on the coating thickness were measured using thin film characterisation techniques and are reported in Section 6.3.3. As a consequence of this non-uniformity a variation in the neutron detection efficiency was also measured and is shown in Section 7.4.

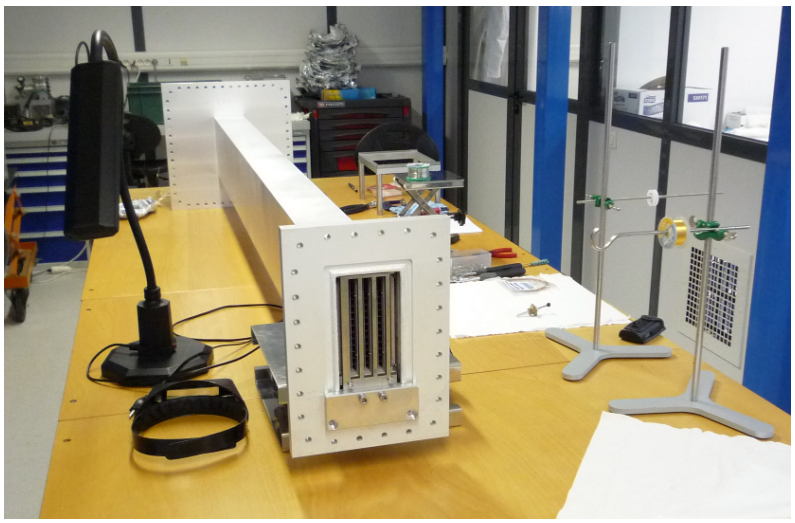

Figure 5.4: The gas-tight vessel used to contain the stopping gas is shown after the MG-96 was inserted.

The individual readout of each of the signals of the MG-96 detector implies the use of 156 channels: a total of 60 for the anode wires and 96 corresponding to each grid.

5.3.3 MG-IN6

A further step in the project requires the integration of a Multi-Grid detector in a real NSS instrument. Measurements such as the detection efficiency versus the wavelength, the estimation of the neutron background or the time resolution can be performed. The chosen machine was the cold neutron time-focussing ToF spectrometer IN6 [41].

Figure 5.5: The MG-IN6 uses the 96 grids of the MG-96 mounted in a different geometry.

IN6 present detector is formed by 337 ^{3}He gas counters covering an active area of 4 m^2. The partial replacement of this detector is made thanks to the modularity of the Multi-Grid concept.

The previously shown MG-96 was decommissioned after the different tests mentioned above were completed. The same grids were used but with a different geometry as shown in Figure 5.5. Instead of linearly stack the 96 grids they were distributed into 6 columns, 16 grids each. As a consequence, the number of anode wires also increases: 360 are used instead of 60. If an individual readout was to be implemented, a total of 456 readout channels (360 wires + 96 grids) would be needed. A reduction in this number was considered at this point.

Grids from different columns but with the same position along the column

axis are grouped three by three. When an event takes place in any of these three grids a coincidence with one of the 180 wires crossing them is found and the event is accounted. By using this method the number of readout channels for the grids decreases from 96 to 32.

The anode wires are connected in a resistive network (studied in Subsection 5.4.2) formed by 30 wires or 2 rows. Two signals per resistive network are readout. 24 channels instead of 360 are needed to readout all the anode wires.

With the mentioned plan the MG-IN6 detector would reduce the readout channels from 456 to 32 + 24 = 56. A further study on the channel reduction consequences is given in Section 5.4.2.

5.3.4 MG-IN5

As a result of the previous work, a preliminary study has been made on a larger PSD. An IN5 module, already studied in Section 1.2.1, was used as a model. If this detector would have to be replaced by the Multi-Grid technology, several parameters will need to be taken into account: minimisation of dead zones, reduction of readout channels, available volume for the PSD at the instrument vacuum chamber, etc.

For this analysis some parameters need to be defined, their values are however not fixed. Further studies of the MG-IN6 prototype need to be accomplished to properly design the MG-IN5. In this contexts, in order to fit the Multi-Grid detector within a IN5 present module, the dimensions of the grids and blades need to be modify: the width has increased from 2 to 2.35 cm. The number of boron-containing layers was kept in 30. A total of 8 columns composed by 128 grids will be needed co to cover an equivalent active area of a present IN5 module (shown in Figure 5.6). The B_4C surface to be coated will raise to ≈ 58 m^2 per module.

If the whole IN5 PSD was to be replaced, 12 modules would be needed. This means 12 modules $\times$ 8 columns = 96 Multi-Grid detectors or 12288 grids. The B_4C coated surface will rise to ~ 693 m^2. A scheme of the twelve IN5 modules using Multi-Grid detectors is shown in Figure 5.7.

Present IN5 PSD uses 768 channels to readout 384 charge division lines (one per tube). If the MG-IN5 was to be installed with an individual readout a total of 18048 channels would be needed. As previously discussed for the MG-IN6 a reduction on the number of channels needs to be considered.

Grids of the same vertical position (defined as X in Figure 5.7) can be connected together in each module. A total of 128 grids in vertical $\times$ 12 modules makes: 1536 channels readout by a pulse heigh discrimination system.

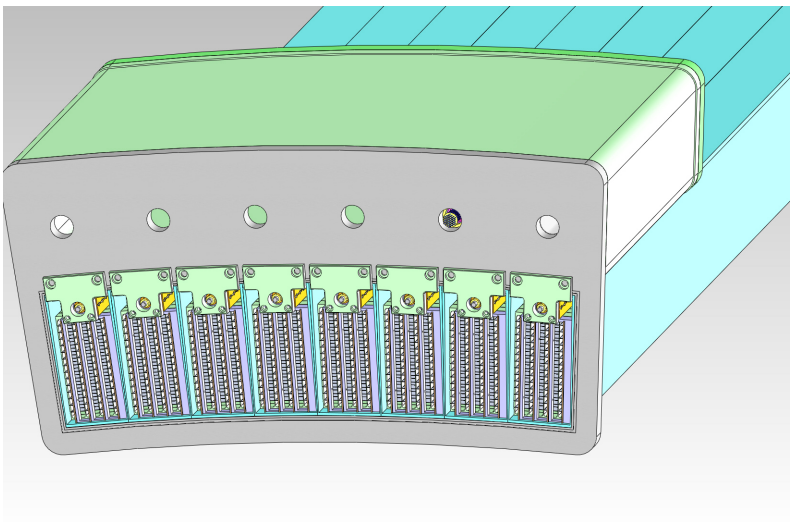

Figure 5.6: Eight Multi-Grid detector filling a vessel of the same size that the present IN5 PSD module. Almost 60 m^2 of boron coating are needed for one module.

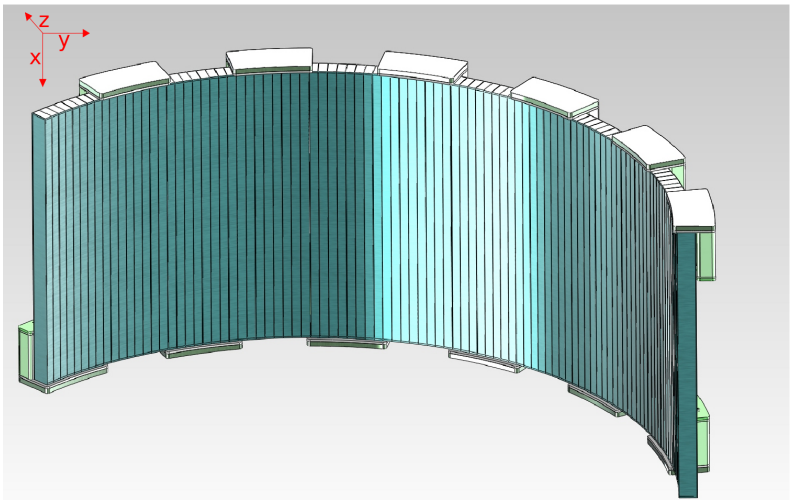

Figure 5.7: A scheme of the Multi-Grid concept replacing the present IN5 PSD. A total of 1728 channels are needed to readout the whole detector.

The position resolution in the horizontal dimension (defined as Y in Figure 5.7) can be reduce to 4 cm instead of the 2 cm of the present voxel size grouping two anode row of wires. Moreover a resistive network can be implemented in depth. Two channels are then needed to read out the resistive network formed by all the wires (60) of a Multi-Grid column. For the whole IN5 PSD, this means 2 channels $\times$ 8 Multi-Grid columns per module $\times$ 12

modules = 192 channels. These channels are read out by a charge division system.

A total of 1728 channels are needed to readout the whole detector which is 2.25 times more than for the present ^{3}He-based one. Approximately 90% of the channels would use a discrimination system which is simpler than the charge division one. With this readout channel reduction the spatial resolution has become: 4 cm in the horizontal dimension, 2.35 cm in the vertical one and 1 cm in depth.

5.4 Electronics

The electronics used in the Multi-Grid detector is now treated. The front-end circuit is studied in Section 5.4.1. Possible optimisation are described. The different solutions proposed to reduce the large number of readout channels in the MG-IN6 and MG-IN5 prototypes are studied in Section 5.4.2. .

5.4.1 Front-End Electronics

An scheme with the front-end electronics used for the individual read out of the Multi-Grid detector (MG-12 and MG-96) is shown in Figure 5.8.

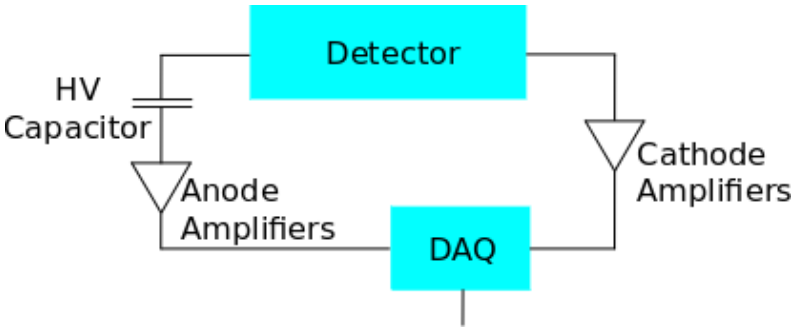

Figure 5.8: A scheme of the Multi-Grid concept replacing the present IN5 PSD. A total of 1728 channels are needed to readout the whole detector.

Signals from the anode wires are decoupled from the HV voltage used to create the gas amplification through a HV capacitor. After that process, they are individually amplified and collected by a Data Acquisition System (DAQ). For the cathode signals the decoupling is not necessary and they are directly amplified. Specifications for both anode and cathode amplifiers can be found in Table 5.2. The DAQ used depends on the experiment:

- It can be a signal digitiser, to study the signal shape.

- A Multi-Channel Analyser (MCA), used to produce PHS.
- Finally a Multi-Channel Controller (MCC) which is used to create images of the active area by looking at the time coincidences between anode and cathode signals.

	τ [μs]	Gain [V/pC]
Cathodes	2	32
Anodes	2	9

Table 5.2: Specifications of both anode wires and cathode grids amplifiers are shown.

As it was in Section 3.4.1, when the pulse mode is used and the time constant of the amplifier is larger than the charge collection time of the detector ($\tau \gg t_c$), the energy deposited in the detector (which is proportional to Q) can be accessed directly reading the amplitude of the generated signals. The energy distribution of the Multi-Grid detector was obtained with a signal digitiser and it is shown in Figure 5.9a. Two are the main reasons to know the energy distribution in a detector:

- As previously studied in Section 2.4, the main γ-rejection method is based on the energy difference between neutron and γ-events.
- As it will be shown below, data treatment algorithms such as the CoG need as inputs the total energy deposit in the gas.

CoG

As said above, the CoG is a data treatment algorithm that allows to increase the spatial resolution of detection systems. This is done by studying the quantity of charge (or equivalently the energy) read in each channel. The spatial position of an event, x_p is then defined as:

$$x_p = \frac{\Sigma_i E_i \cdot x_i}{\Sigma_i E_i}, \tag{5.1}$$

where x_i is the each one of the readout channels and E_i the energy collected in each channel. As said above, position resolutions beyond the wire pitch in a MWPC can be achieved. As it will be studied in Section 7.2.2, in the case of the Multi-Grid detector the CoG is applied to the cathode channels. An increment of the spatial resolution along the wire dimension is expected.

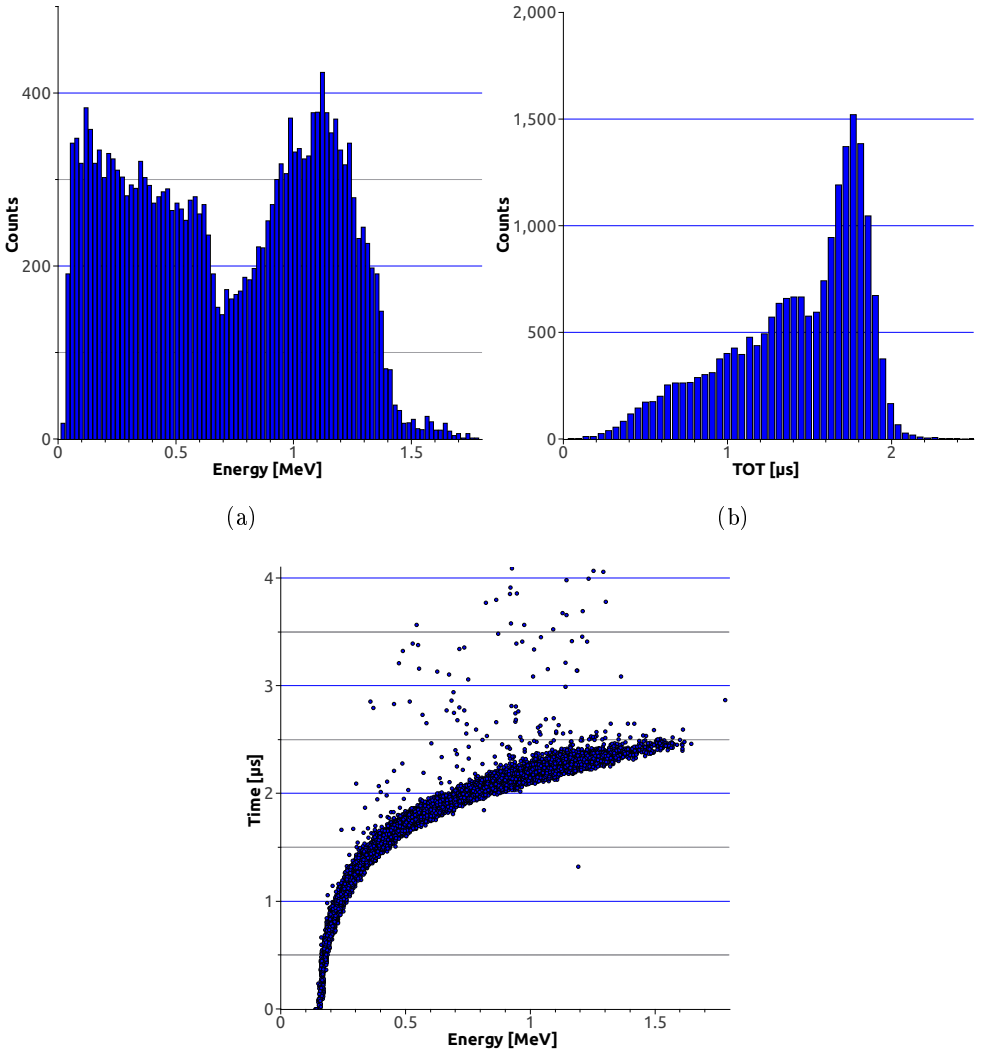

Figure 5.9: **(a)** The obtained PHS on an anode wire for a Multi-Grid tube. Distribution of the most common branch ratio of the boron capture can be seen. **(b)** The two peaks shown in the ToT distribution are also produced by the two most common reaction fragments. **(c)** The relation between the ToT of the signal and the energy of the event is shown for the typical measurement conditions of the Multi-Grid detector.

A typical way to implement the CoG algorithm is by measuring the ToT of the readout signals rather than the signal amplitude. For the Multi-Grid detector the ToT distribution is shown in Figure 5.9b. The relation between the pulse amplitude (or energy deposit in the pulse mode) and the ToT value

is well known and, for the Multi-Grid detector is found in Figure 5.9c.

As can be seen in Figure 5.9b, the signal length (which can be defined as the mean value of the ToT distribution $\approx$ 1.84 μs) is entirely defined by the amplifier time constant, τ. As it was seen in Section 3.4.3, τ has a critical role in the dead time calculations. A reduction of its value would decrease dead time and therefore increase the counting rate capability of the Multi-Grid detector.

Counting Rate Optimisation

As it was studied in Section 3.4.1, the time constant of the front-end circuit working in the pulse mode, τ, needs to be larger than the detector collection time ($\tau \gg t_c$). However, if it is too large, higher levels of noise will be integrated decreasing the γ-discrimination. Moreover neutrons arriving within the period τ after a previous event will not be counted. An optimisation of this parameter is therefore needed to increase the counting rate performances of the detector. To study this phenomenon, a faster pre-amplifier was used (τ = 2.54 ns). Energy and ToT results can be found in Figures 5.10a and 5.10b respectively.

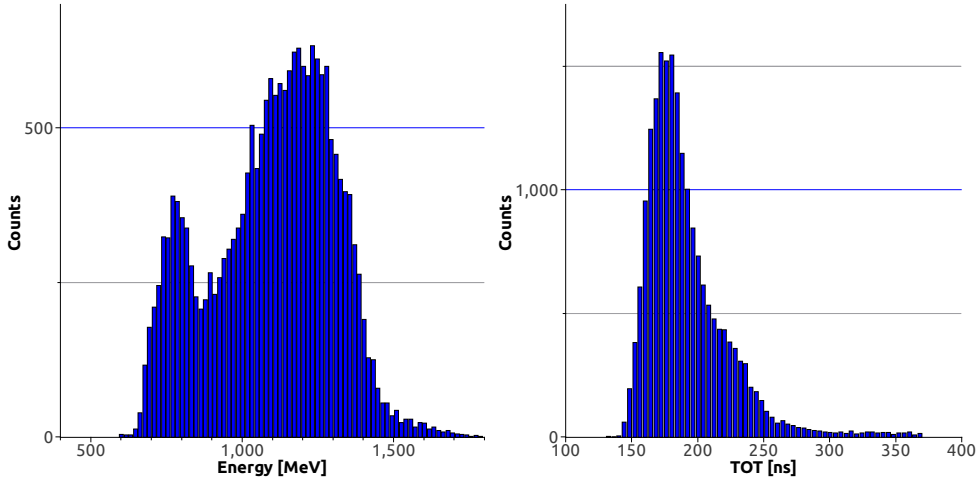

(a) (b)

Figure 5.10: **(a)** Energy spectrum calculated integrating the charge collected in the Multi-Grid detector with a fast pre-amplifier (τ = 2.4 ns). **(b)** The ToT distribution acquired with the same pre-amplifier.

As it is shown in Figure 5.10a, the major part of the lithium fragments are lost. The reason is that the signal-to-noise ratio of this measurement was relatively low. The α-fragments however are clearly distinguishable. Conse-

quently, the ToT distribution shown in Figure 5.10b only shows the longer component. This is however not an issue because the aim of this measurement is to estimate the charge collection time of the detector at nominal voltage, t_c. In this sense, $t_c \ll 400$ ns seems a good estimation.

If an amplifier with a time constant of $\tau \approx 250$ ns was used in the Multi-Grid detector, the whole charge will be collected. Moreover, this value is 8 times shorter than the 2 μs seen in Table 5.2. Faster amplifiers are proposed to reduce the dead time of the Multi-Grid detector and increase its counting rate capabilities.

5.4.2 Readout Channels Reduction

As explained above, if an individual readout system is installed in prototypes MG-IN6 and MG-IN5 a large number of channels will need to be treated. In the case of MG-IN5, 16 times more channels than the present IN5 PSD are required. In this context a reduction in the number of readout channels is necessary to reduce the complexity of the detector but also to keep this technology affordable.

Two different methods are used. On one hand to connect several grids of the same vertical position together. On the other hand, a resistive network has been proposed to read either 15 wires in depth of the Multi-Grid detector. The latter method is studied in Section 5.4.2.

In the first case the main effect on the detector performance is the reduction on the Multi-Grid global counting rate capability. If a grid is fired somewhere in the same line a coincidence with the wires is done. However, if a second neutron arrives within the amplifier integration time τ, to any of the grids connected together it will not be counted. In this sense, the optimisation of τ previously discussed could be applicable to reduce this effect.

Charge Division This technique originally consisted in using a resistive wire for the gas amplification. By reading the two ends of the wire, the ratio between the amplitudes in both ends could be used to estimate the point where the avalanche took place along the wire. This can be seen from Equation 5.2:

$$\frac{Q_R}{Q_L} = \frac{x}{x - L}, \tag{5.2}$$

where L is the length of the wire, x the point where the avalanche took place and Q_R and Q_L are the charge readout on the right and left end of the wire.

In the Multi-Grid detector a different approach is taken. Charge division is not implemented to determine the interaction position along the wire length. This is done reading out the grids. Alternatively, the 15 wires in depth (axis Z in Figure 5.7) are connected trough a resistive line by placing a resistor, R, between each wire. Two signals are read out at both ends of the resistive line. In the same way that what it was seen in Equation 5.2, the fired wire is estimated through the ratio between charge collected on the left and right side of the line. Alternatively, a charge division readout was applied to the cathode signals. However, due to the capacitive coupling between the grids already discussed in Section 5.2.1, not a proper localisation could be achieved by this method.

As a drawback higher applied voltages are needed to properly set an acceptable signal-to-noise ratio which decreases the quality of the energy spectrum. Besides, the electronics needed for the read out are more complicated than the rather simple pulse amplitude threshold used in the rest of the channels.

5.5 Conclusion

Detector requirements of a ToF instrument were discussed in Section 1.2.1. Also, the results of the MC simulation were seen in Chapter 4. These two sources were used to develop the Multi-Grid concept. This boron-lined detector is based on several layer of neutron converters ($^{10}B_4C$ in this case). The coating of this compound is made onto planar blades that are thereafter inserted in aluminium frames forming grids. Grids are stacked and can form relatively large ($\geq$ 2 m) rectangular tubes.

Several types of Multi-Grid detectors were design and built. Specifications of each one of them were studied in this chapter. MG-12 and MG-96 were built and tested. Measurements on detection efficiency, γ-discrimination, long-term stability, ageing, wall-effect and cross-talk were performed. MG-IN6 was built after decommissioning MG-96 using the same grids but mounted in a different geometry. It will be used in a real ToF instrument. A preliminary study was done to built a detector able to replace an IN5 module. Future results of the MG-IN6 will undoubtedly change many of the design details of this prototype. An important number of problems however can be already address with the mentioned study.

Different aspects of the front-end electronics were treated. Special attention was paid to the minimisation on the number of readout channels. The aim is to reduce the detector complexity. Several ways to achieve this reduction were studied. How these methods affect the ToF resolution or the counting rate

capability were studied. Based on the ToT calculus, the CoG algorithm was study as a method to improve the spatial resolution of the detector along the wire dimension. This will be further studied in Section 7.2.2.

Chapter 6

Boron Converters

6.1 Introduction

The need of boron-containing films as neutron converters for the Multi-Grid detector has been discussed in Chapter 1. Moreover, a MC simulation was performed in order to optimised a number of important parameters for the design of the detector. Its results, shown in Chapter 4, set the optimal thickness of the $^{10}B_4C$ layer in 1.0 μm.

The choice of $^{10}B_4C$ was made according to the long-term properties (chemical, mechanical and electrical) of this compound compared to pure boron. Different deposition techniques were studied. A production method that warranties large scale production capability is to be found.

A complete characterisation of the films is required. A better knowledge of the converter properties will help to understand the exact performance of the Multi-Grid detector. Thin film characterisation techniques together with neutrography and direct neutron absorption were performed. Values obtained from these analyses, such as mass density, atomic concentration of the different elements, etc. were used as inputs for the MC simulation. This software was also use to estimate the incidence on the detection efficiency of the different contaminants.

6.2 Coating Techniques

A maximisation of the ^{10}B-concentration in the converter is needed for a maximal detection efficiency of the Multi-Grid detector. Pure ^{10}B layers were first considered. However, several properties of $^{10}B_4C$ make it a more suitable can-

didate: it presents high thermal and chemical stability [42]. In this sense, the long operation time of neutron detectors requires the stability of the coating over time. Moreover, it is easier to handle in a deposition chamber and it has a lower bulk resistivity, which enhance the charge extraction in the detector. The main disadvantage comes from the 20% lower ^{10}B-concentration of $^{10}B_4C$ compared to pure boron.

Despite some works done about the implementations of Chemical Vapour Deposition (CVD) for the B_4C coating [43], the usual technique used is the magnetron sputtering [44]. Reasons for this rely on the lower impurities concentration – specially hydrogen – achieved with magnetron deposition. A review of the chosen technique for the the neutron converter coating of the Multi-Grid detector is made.

6.2.1 DC Magnetron Sputtering

Magnetron sputtering belongs to the wider family of Physical Vapour Deposition (PVD) techniques by which the deposition material is vaporised and condensates on a substrate forming films. Due to the relatively low pressures ($\sim 10^{-4}$ Pa) used during the process, chemical reactions are ignored. During the sputtering process atoms are ejected from the sputtering target by bombarding the surface with energetic ions [45]. The scheme of a DC magnetron sputtering machine is shown in Figure 6.1.

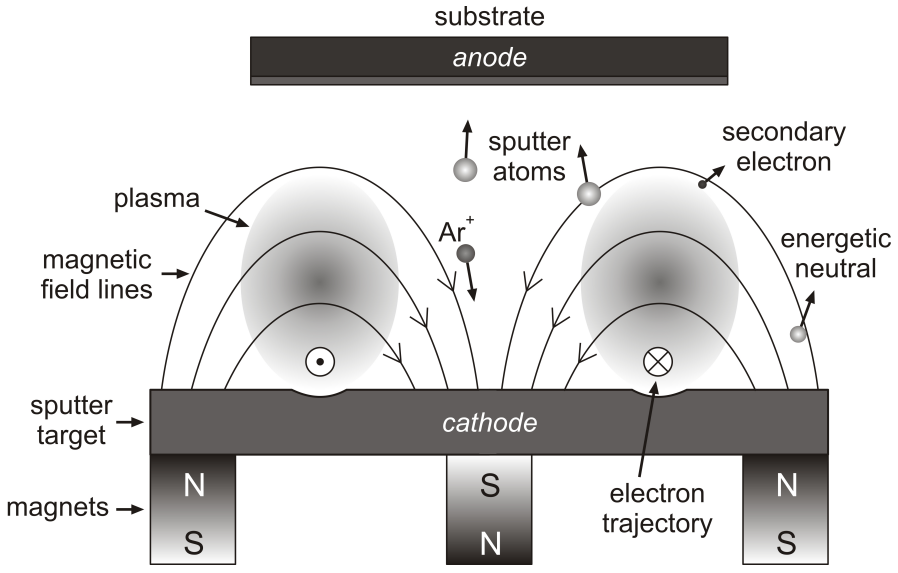

Figure 6.1: Scheme of a DC magnetron sputtering machine. The principal components are shown: the substrate, the sputtering target and the magnets [45].

An inert gas, typically argon, is added to the system and acts as the sputtering gas. The target is mounted in a negatively charged magnetron, and operates as the cathode in the deposition chamber. When high voltage is applied to the target, a discharge provokes the gas ionisation. The target is then bombarded with highly energetic gas ions. If the energy of these ions is higher than the binding energy of the atoms on the surface of the target they are sputtered. These atoms, together with the gas ions, form a plasma which is confined due to the magnetic field created by the magnetron. Secondary electrons are also created during collisions. They maintain the process by colliding with the atoms in the plasma and ionising them. Electrons are also confined by the magnetic field increasing the interaction probability. The sputtered atoms – electrically neutral – cross the chamber and condensate on the chamber walls and on the substrate.

The deposition chamber

The deposition took place at the IFM - Thin Film Division of the Linköping University in an industrial CC800/9 deposition system manufactured by CemeCon AG, shown in Figure 6.2a. Prior to deposition, the system was evacuated at full pumping speed for 3 hours and the substrates degassed at temperatures up to 500 $^{\circ}C$. The base pressure reached was $2.5 \cdot 10^{-4}$ Pa. During the deposition the argon partial pressure was kept at ≈ 0.8 Pa.

There are two main control parameters for the coating process. On one hand the magnetic field: the number of magnetrons used and their power. On the other hand, the substrates: their relative movement with respect to the targets and their temperature. Effects of these two parameters were studied.

Substrates Aluminium blades (20 mm x 80 mm x 0.5 mm) from the alloy AL-5083 – already introduced in Chapter 5 – were used as substrates. After being cleaned, blades were mounted onto a carousel-like sample holder which allows 2-axis planetary rotation and double-side depositions. The inner part of the deposition machine together with the blades mounted on the sample holder are shown in Figure 6.2b.

As discussed in Chapter 5, the double-side deposition approach for the boron coating is used for the Multi-Grid detector. Furthermore, from the deposition point of view it is also advantageous. Internal stresses in the B_4C limit the thickness of the coating [46, 47, 48] and bend the substrate on which the coating is done. This problem is reduced when the carousel rotation is activated: coating on both sides at the same time compensates the stresses and relatively thick layers (up to 3 μm) without bending the substrate are

(a) (b)

Figure 6.2: **(a)** The CemeCon AG CC800/9 semi-industrial deposition system. It can achieved ultra-high pressures and relatively high substrate temperatures. **(b)** Inside the deposition chamber. The carousel-like sample holder allows 2-axis planetary rotation for double-side coating. 96 blades can be coated in the same run.

achieved. However, the lower deposition rate of this method induces a higher impurity content in the coating. To reduce this effect, the substrates are heated up to 400 $°C$. Under these conditions, low impurity content and good adhesion are possible in the rotational mode.

As seen in Figure 6.2b, 4 blades can be mounted along the height of the deposition chamber in each position of the sample holder. There are 4 sample holders per axis and six axis in total. Up to96 blades can be coated in one run of the deposition machine. Blades are labelled according to their position in the coating chamber, from the bottom to the top: A, B, C and D. Differences on the coating thickness depending on the position of the blade were found and will be studied in Section 6.3.1.

A complete run took around 12 hours. This number together with the coating surface which can be covered during a run give the total film surface coated per day ≈ 0.62 m^2. This number was obtained when minimising the number of operator interventions in the machine out of working hours. The process is therefore not optimised and a faster coating process could be implemented.

Magnetron Four sputtering targets (88 mm × 500 mm × 5 mm) can be mounted simultaneously on the cathodes of the sputtering machine. These targets are bonded to Cu-plates necessary to cool down the magnetrons. After some preliminary tests performed with natural B_4C, ^{10}B-enriched B_4C targets were used.

The power of the magnetrons has an influence on the plasma density. The higher the power the denser the plasma. A denser plasma yields a higher deposition rate. It has been proven that the faster the boron layers are grown the lower contaminant concentration is found to be presented in the coating [49].

Other parameters such as the pressure of the sputtering gas and the bias potential of the substrates were studied. No significant difference in the quality of the coating was found when varying these parameters.

6.3 Thin Film Characterisation Techniques

To study several coating properties such as its structure, isotopic composition, film thickness or mass density, etc. different thin film characterisation techniques were used.

6.3.1 SEM

The Scanning Electron Microscopy (SEM) is a type of electron microscopy in which the electron beam images the sample while performing a scan. The electrons interact with the atoms that make up the sample producing signals that contain information about the sample's surface topography. A LEO 1550 instrument operated at 5 kV working at 4 mm from the sample was used. Only samples coated on silicon wafers were measured. Results for aluminium substrates are expected to be similar.

A 3 μm-thick coating is shown in Figure 6.3. The B_4C layer was found to be dense with columnar structure and smooth surface. Accurate thickness measurements were performed using image analyses.

Yet another requirement of the boron coating is the uniformity over large areas. Several SEM measurements were made at several points of the deposition chamber. Results can be found in Figure 6.4.

An important non-uniformity in the coating along the height of the deposition chamber was found. Measured thickness goes from 0.85 μm at the centre to 0.5 μm at the edge of the sputtering chamber. This implies an overall gradient of $\approx 40\%$. However, the blades used for the Multi-Grid detector

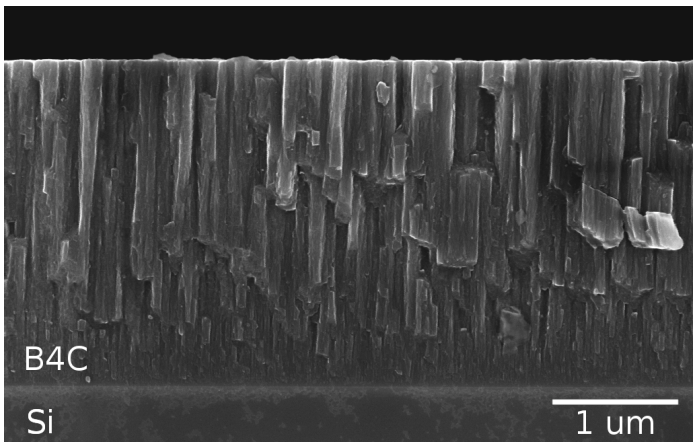

Figure 6.3: An image obtained with SEM of a 3 μm-thick B_4C film. The columnar structure and the smooth surface are visible.

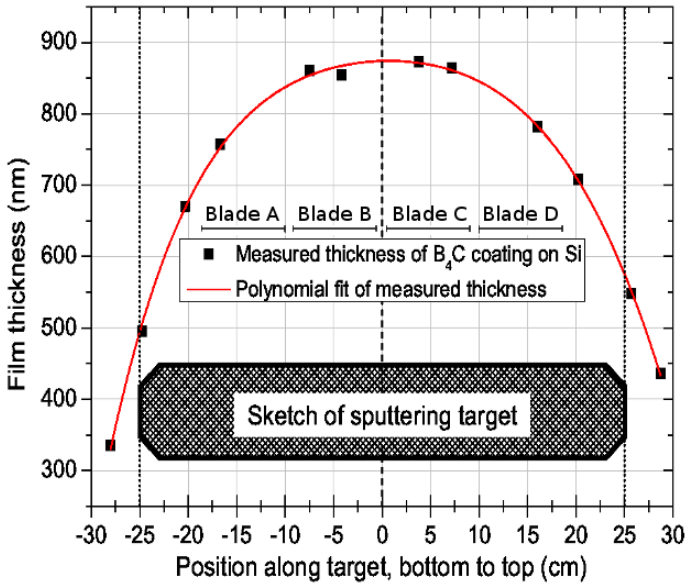

Figure 6.4: A typical variation of the sputtering yield in the deposition machine measured with SEM on silicon wafers placed in different points along the chamber heigh. [49].

were placed between positions -18 cm and +18 cm. This yields a maximum variation of $\approx 13\%$ on the coating thickness for the blades placed in the outer part of the chamber (regions A and D). A much smaller variation ($\approx 5\%$) was measured for the blades placed in the centre of the chamber (regions B and C).

6.3.2 X-Ray Reflectivity

X-Ray Reflectivity (XRR) is a surface-sensitive analytical technique used to characterise surfaces, thin films and multi-layers. It is related to the complementary technique of neutron reflectometry. The basic idea is to reflect a beam of X-rays from a flat surface and to measure the intensity of X-rays reflected in the specular direction. The analysis of the reflected beam allows the estimation of several parameters of the film such as its mass density.

An X-ray Cu-tube was used for this measurement. Within the Cu-tube, charged particles are accelerated onto a Cu-plate from where the X-rays are emitted. A Ni-filter prevents the emission of other radiation except the Cu K_α which corresponds to a wavelength of 1.54 Å.

As seen in Section 6.3.1, the coating thickness can be precisely studied with SEM. Knowing this parameter, the density of the coating can be estimated. Results show a $\approx 90\%$ of the bulk density of B_4C for the coating: $\rho_{B_4C} = 2.242$ g/cm^3.

6.3.3 ERDA

Ion beam analyses were used to determine the concentration of specific elements. This parameter can also be studied along the coating depth. Elastic Recoil Detection Analysis (ERDA) is based on the elastic scattering of incident ions with the atoms that make up the sample. The incident ions knock out lighter target atoms which escape the layer and are detected as a function of their energies and/or masses. Good depth profiling can be achieved for elements lighter than the incident ions. Sensitivities are in the order of 0.1 at. %.

A specific detection set-up is needed to simultaneously obtain information on both the energy and the mass of the recoil atoms: the Time-of-Flight Energy ERDA (ToF-E). Atoms of different masses and same energy can be distinguished using the kinetic energy relationship:

$$E = \frac{mv^2}{2}. \tag{6.1}$$

By measuring the time, t, that the knocked out atoms take to travel the known distance, l, the mass of the atom is calculated:

$$m = \frac{2E\ t^2}{l^2}. \tag{6.2}$$

The found composition is shown in Table 6.1.

Isotope	^{10}B	^{11}B	^{12}C	^{1}H	^{16}O	^{14}N
Percentage [at. %]	79.3	2.4	17.1	0.7	0.4	0.1

Table 6.1: Isotopic composition measured with ERDA of the $^{10}B_4C$ used for the Multi-Grid detector.

Results of the depth profile are shown in Figure 6.5. Quantities are roughly constant along depth. Only at the surface the concentration of some of the contaminants – specially oxygen – becomes important. This oxidation process is well known in thin film science and does not seem to affect the detector performance.

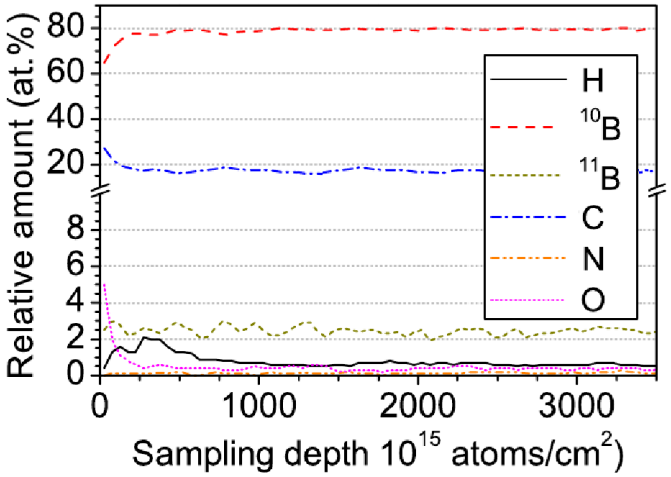

Figure 6.5: ToF-ERDA depth profile of a $^{10}B_4C$ coating on silicon. A higher concentration of impurities due to oxidation is found at the interface [49].

Effect of the Contaminants on the Efficiency As seen above, the overall atomic percentage of the contaminants in the studied coatings accounts for $\approx$ 1.2%. Elements more likely to be found as contaminants are hydrogen, oxygen and nitrogen. Besides these three, a concentration of carbon higher than the stoichiometric is considered as a contaminant. The sputter gas used, argon in this case, is also studied. An analysis on the decrease in detection efficiency due to the presence of these contaminants in the coating is made.

The MC simulation already seen in Chapter 4 was used. The idea is to quantify the effect of the different contaminants seen before to the stopping power of the coating. To do so the density of ^{10}B-atoms, $n_{^{10}B}$, is kept equal for all cases. A 10% higher concentration of the contaminant is added. As a result a denser coating is obtained and therefore a lower detection efficiency.

This new density is largely dependent on the atomic mass of the different contaminants as can be seen in Figure 6.6.

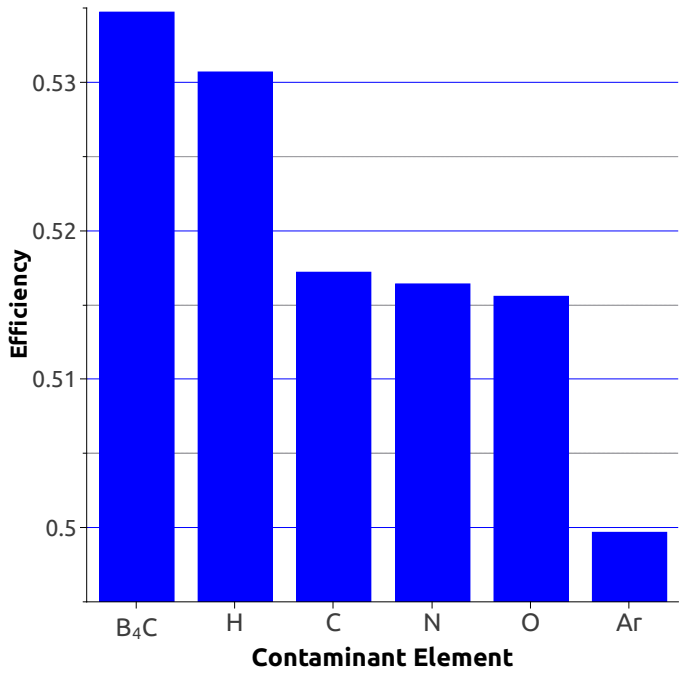

Figure 6.6: Detection efficiency obtained with the MC simulation when adding a 10% contaminant concentration to the studied boron-film.

The first value corresponds with the $^{10}B_4C$ layer studied above. A detection efficiency of $\epsilon = 53.47\%$ was obtained in Chapter 4. When adding a 10% of a contaminant the detection efficiency decreases. This reduction is related with the higher density of the film. Therefore the higher mass number the higher stopping power, as seen in Section 2.3. For hydrogen a small decrease was measured, $\epsilon = 53.07\%$. Carbon, oxygen and nitrogen show similar values due to their similar masses. In the case of a 10% argon contamination the detection efficiency would drop to $\epsilon = 49.97$ %.

6.4 Neutron Characterisation Techniques

Complementary to thin film techniques, neutrons can be used for the characterisation of the coatings. No direct information on the thickness or the density of the layers can be accessed. However, it provides a direct measure of the ^{10}B-concentration per unit area. A theoretical calculation of the $\Sigma_{tot}^{^{10}B}$ is presented. Two types of measurements were performed to experimentally

estimate its value: neutrography and direct neutron absorption.

Theoretical Calculation

As it was studied in Section 2.2, when a collimated neutron beam crosses a medium its intensity reduction follows the attenuation law. In the case of $^{10}B_4C$ we have:

$$N(d) = N_0 \; e^{-(\Sigma_{tot}^{^{10}B} \; \cdot \; d)} \tag{6.3}$$

where N_0 is the incoming neutron flux onto the boron-containing film, N(d) is the attenuated flux after crossing the film and d the film thickness. The ^{10}B total macroscopic cross section $\Sigma_{tot}^{^{10}B} = n_{^{10}B} \cdot \sigma_{tot}^{^{10}B}$, is defined as a function of the ^{10}B atomic density and the ^{10}B total neutron cross section respectively.

Contributions from other elements – specially carbon – have been neglected due to their lower cross sections. Also, since $\sigma_{capt}^{^{10}B} \gg \sigma_{scat}^{^{10}B}$, we can ignore the latter contribution and $\sigma_{tot}^{^{10}B} \simeq \sigma_{capt}^{^{10}B}$. The energy dependence for $\sigma_{capt}^{^{10}B}$ has already been shown in Figure 2.1. In the region of interest for NSS (1 - 10 Å), a linear dependence is found between σ_{capt} and λ. For ^{10}B this relation can be written as:

$$\sigma_{capt}^{^{10}B} \simeq 3835 \cdot \frac{\lambda[\mathring{A}]}{1.8} \; barn. \tag{6.4}$$

To determine $n_{^{10}B}$, results shown in Table 6.1 are used. Knowing the isotopic masses, M_i, and the atomic percentage, P_i, of each element, the film atomic weight can be calculated:

$$M_{film} = \Sigma_i \; M_i \cdot P_i = 10.33 \; [g/mol]. \tag{6.5}$$

Using this value together with the measured mass density, the film atomic density, n_{film}, can be estimated:

$$n_{film} = 2.224 \; \frac{g}{cm^3} \; \cdot \; \frac{1 \; mol}{10.33 \; g} \; \cdot \; \frac{N_A}{1 \; mol} = 1.31 \cdot 10^{23} \; cm^{-3}. \tag{6.6}$$

When multiplying n_{film} by the ^{10}B-concentration present in the coating, $n_{^{10}B}$ is obtained:

$$n_{^{10}B} = n_{film} \cdot 0.793 = 1.04 \cdot 10^{23} \; cm^{-3}. \tag{6.7}$$

With this value, the wavelength-dependent $\Sigma_{capt}^{^{10}B}$ can be calculated:

$$\Sigma_{tot}^{^{10}B} = n_{^{10}B} \cdot \sigma_{capt}^{^{10}B} \simeq 2.22 \cdot 10^{-2} \cdot \lambda[\mathring{A}] \; \mu m^{-1}. \tag{6.8}$$

A direct access to $\Sigma_{tot}^{^{10}B}$ can be achieved by measuring N_0 and $N(x)$ for different layer thickness's. From Equation 6.3, it follows:

$$-ln\left(\frac{N(d)}{N_0}\right) = \Sigma_{tot}^{^{10}B} \cdot x. \tag{6.9}$$

6.4.1 Neutrography

This method allows the measurement of $\Sigma_{tot}^{^{10}B}$ of relative large samples (as large as the active area of the PSD used) at once. A complete cartography of the sample is obtained in relatively simple measurements. The Bidim-26 was the ^{3}He-based multi-wire PSD used for this measurement. Its active area covers 26 cm $\times$ 26 cm and has a pixel size of 2 mm $\times$ 2 mm.

Set-Up

This experiment was entirely performed at the CT2 beam-line. In order to uniformly illuminate the entire active area of the Bidim-26 the neutron beam must be widen. After the monochromator the beam is approximately 5 cm $\times$ 6 cm. Neutrons can be isotropically scattered using a hydrogen-containing material such as Poly(Methyl Methacrylate) (PMMA). A diverging flux is thus, obtained.

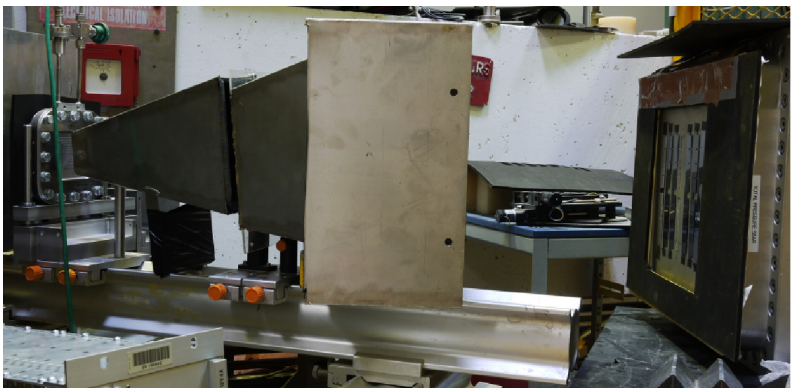

Figure 6.7: The Neutrography set-up. After the low-efficiency neutron detector used as a beam-monitor, the scatter is placed inside a B_4C shielding to minimise the background. The scattered beam impinges the window of the Bidim-26 detector where the blades are placed onto the slits of a cadmium mask.

The scatterer is placed at $\approx$ 1 m from the detector, as can be seen in Figure 6.7. A homogeneous beam impinges the detector window. Blades are placed directly on the window in order to minimise parallax errors due to the

divergence of the beam. A cadmium mask was attached to the window of the detector. It hides any material used to attach the blades to the detector and reduces the background.

A calibration measurement was done in which the non-coated substrates were placed onto the slits of the cadmium mask. This is equivalent to measure N_0. Due to the small size of the pixel in the Bidim-26 detector a long exposition time (2 days) is needed to reach good statistics. A second measurement is performed after replacing the aluminium blades for the coated ones. N(d) is then measured per each pixel. The resulting image of this measurement is shown in Figure 6.8.

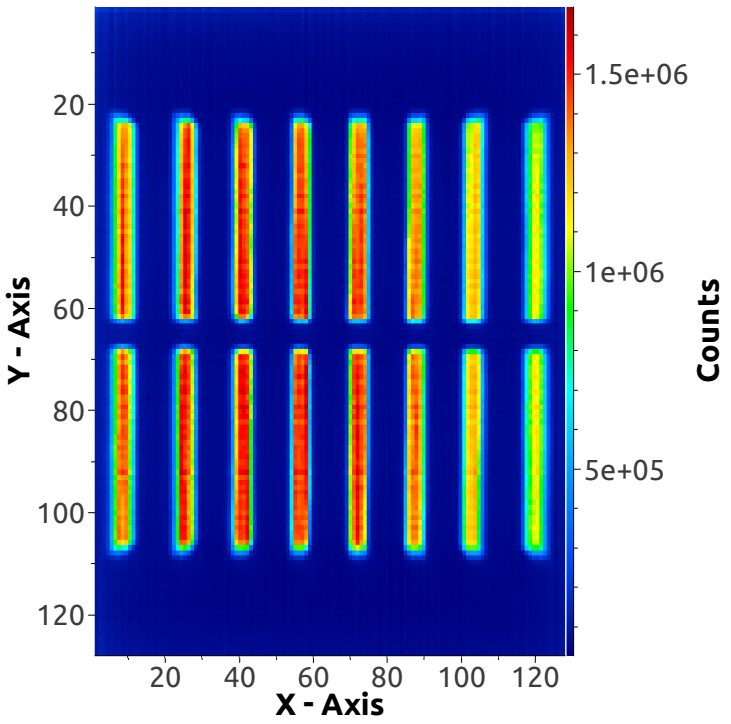

Figure 6.8: An image of the Bidim-26 detector used for neutrography. The 16 slits of the cadmium mask are visible. Boron coated blades were placed onto them.

Due to the divergence of the scattered beam the edges of the slits show a halo. Information coming from these areas could induce to an error. Region-of-Interests (ROIs) are created within each slit. $\Sigma_{tot}^{^{10}B}$ is calculated in these areas. Its value, as a function of the position of the blade in the deposition chamber is shown in Figure 6.9.

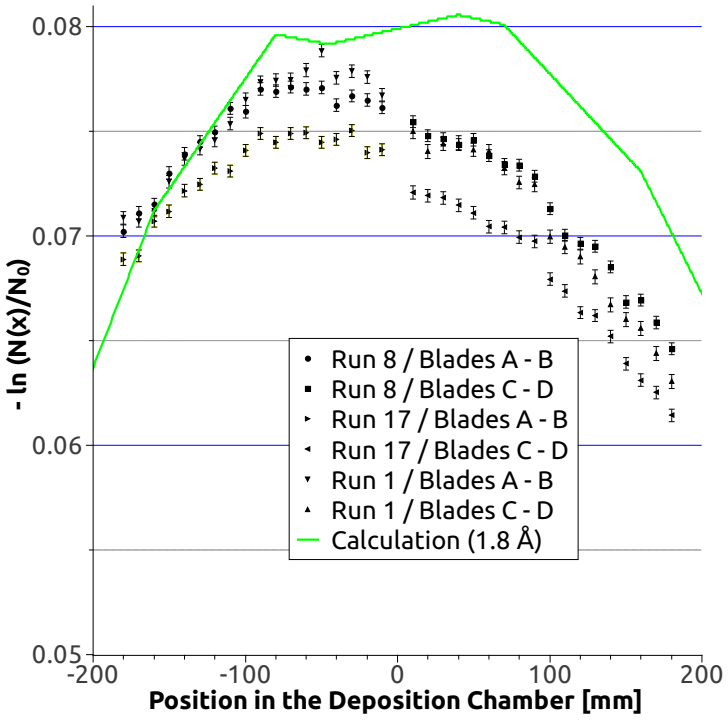

Figure 6.9: $\Sigma_{tot}^{^{10}B}$ is plotted for several boron-coated blades as a function of the position in the deposition chamber. A lower absorption than expected was discovered. Also, an important asymmetry was found compare to previous results.

Results

The use of the scatterer to get a widen beam provokes a thermalisation of the incoming neutrons. After a number of collisions with the hydrogen atoms of the PMMA their energy is modified. In this case, they gain some energy (or equivalently reduce their wavelength, λ). In Figure 6.9, the theoretical calculation for $\lambda = 1.8$ Å, the corresponding λ for room temperature neutrons instead of $\lambda = 2.5$ Å, is shown.

Blades from three different runs – 1st, 8th and 17th – were measured. For each of them, blades coated on the different regions were studied. The results for the lower part of the chamber (negative values of the X-axis in Figure 6.9) are consistent with what was previously seen in Section 6.3.3. The outer blades, corresponding to region A, shows a gradient in absorption related with the thickness gradient. In the centre of the chamber, represented by blades from region B, the behaviour is more stable.

An important asymmetry was found in the upper part of the deposition

chamber (positive values of the X-axis). In this case values for the outer, corresponding with region D, and centred blades, region C, show a lower absorption than the lower half of the deposition chamber. This behaviour was not observed in the SEM measurement.

A non completely homogeneous scattered beam could explain the non-asymmetry found in Figure 6.9. This inhomogeneity could also affect the wavelength of the incoming neutrons which is function of the number of collisions that they undergo within the scatter. Present results of neutrography can only be used to analyse uniformity within each deposition region. No reliable information on $\Sigma_{tot}^{^{10}B}$ can be extracted from it. Improvements in the set-up need to be accomplished to warranty a homogeneous – in both, size and wavelength – neutron beam.

6.4.2 Direct Neutron Absorption

Due to the problems observed with the Neutrography a simpler measurement was performed. Instead of a PSD covering a relatively large area a ^{3}He-counter was used. A wide beam is not longer needed and a collimated neutron beam can be used.

Set-Up

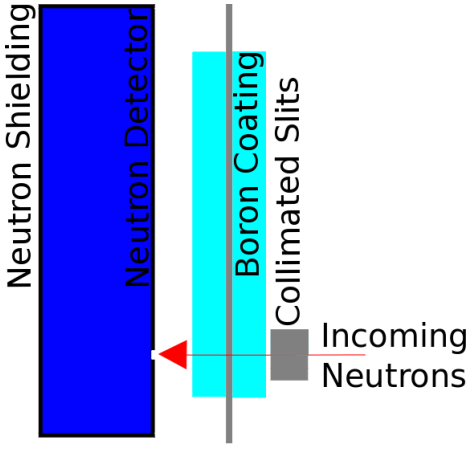

Figure 6.10: Scheme of the Direct Neutron Absorption measurement. A collimated neutron beam impinges the coated blades. Transmitted neutrons are detected with a standard ^{3}He-tube. Instruments CT2 (λ = 2.5 Å) and T3 (λ = 7.5 Å) were used.

For this measurement the T3 instrument (λ = 7.5 Å) and the CT2 beam-

line (λ = 2.5 Å) at the ILL were used. An scheme of the standard set-up is shown in Figure 6.10. A collimated monochromatic neutron beam (0.5 mm × 2 mm) impinges the sample. Transmitted neutrons are measured with a ^{3}He-based counter. Background due to scattering processes within the blades is minimised with the neutron counter shielding.

Transmitted neutrons for a blank blade, $N_0 = N(d = 0)$, and several boron thickness's, N(d), were measured.

Following Equation 6.9, - ln $(N(d)/N_0)$ versus the thickness of the boron coatings is plotted. The trend-line corresponds to $\Sigma_{tot}^{^{10}B}$. Results can be found in Figure 6.11. Double-side coated blades were used for this experiment.

Results

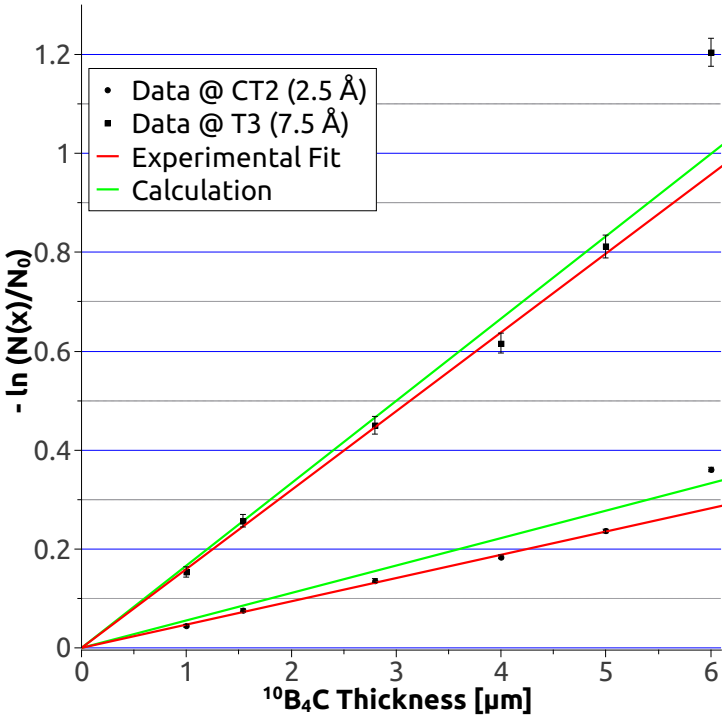

Figure 6.11: $\Sigma_{tot}^{^{10}B}$ is plotted as a function of the film thickness for several double-side coated blades. A linear behaviour was found for both wavelengths.

As expected, a linear behaviour for $\Sigma_{tot}^{^{10}B}$ was found for both wavelengths. The last point, corresponding with a double-side boron layer of 6 μm, was found to be more absorbing than foreseen in both instruments. Such a response could be explained by a slightly thicker coating on this sample. This point

was therefore not used for the trend-line calculations. Lower values for the absorption were found in both cases. For $\lambda = 7.5$ Å the disagreement was found to be 4.32%. In the case of $\lambda = 2.5$ Å a larger discrepancy 17.58% was measured.

A possible explanation for the four times lower absorption found in CT2 compare to T3 could come from a non-entirely monochromatic neutron beam. It is possible that an important percentage of the neutron distribution coming out of the graphite monochromator has a lower wavelength than 2.5 Å. The only possible value of this harmonic contamination is $\lambda = 1.25$ Å (3rd harmonic cannot be transported by the neutron guide). This would imply the measurement of a lower $\Sigma_{tot}^{^{10}B}$ as it is the case. A 30% contamination of this component would be necessary to match the results.

Uniformity

A variation in the neutron absorption is expected due to the non-uniformity of the coating thickness seen in Section 6.3.1. Direct neutron absorption is now used to confirm this result. Several points were measured along the blade length. Any variation in the coating thickness will yield a fluctuation in the transmission profile. Scans were performed with a pitch of 1.2 mm for the four different types of blades according to their position in the deposition chamber. Results can be found in Figure 6.12.

The gradient in thickness previously discussed can be seen. For coating regions in the outer part of the deposition chamber, a lower absorption close to the edges is found. Blades placed in central regions show a more stable response. The same behaviour is found at CT2 with $\lambda = 2.5$ Å.

To achieve a high uniformity over large areas for the Multi-Grid detector this phenomenon has to be taken into account during the mounting of the blades. A specific mounting conceived to improve the uniformity will be explained and discussed in Section 7.4.

6.5 Conclusion

As a boron-containing compound $^{10}B_4C$ was chosen over pure ^{10}B due to its higher reliability (thermal, chemical, etc.) which makes easier the deposition process. Long-term stability, high film quality, low impurities and high ^{10}B concentration, were achieved with the chosen deposition technique: DC magnetron sputtering.

Layer thickness's were measured using SEM. With this parameter known,

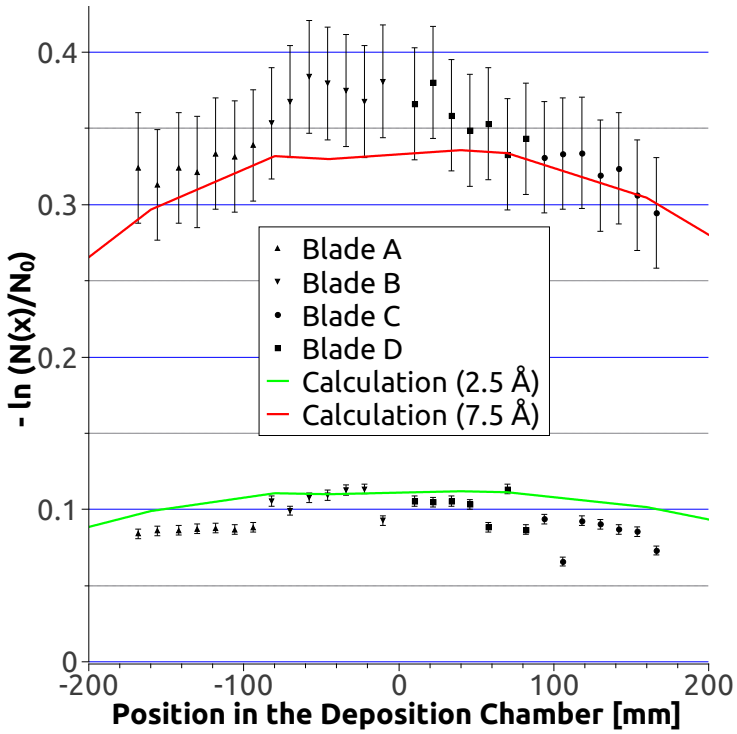

Figure 6.12: $\Sigma_{tot}^{^{10}B}$ measured at different positions corresponding to the four different regions in the deposition chamber: A, B, C and D. Results were obtained at two different instruments with two different wavelengths.

the film density was estimated by the use of XRR. Its value was found to be $\rho_{B_4C} = 2.24$ g/cm^3. Film isotopic composition was determined as a function of depth with ERDA. MC simulation were performed to estimated the reduction in the efficiency due to the presence of contaminants in the films.

Neutrography and direct neutron absorption measurements were performed in two different instruments (T3 @ $\lambda = 7.5$ Å and CT2 @ $\lambda = 2.5$ Å) were used to validate the previous results. $\Sigma_{tot}^{^{10}B}$ was measured as a function of the layer thickness. As expected, an linear behaviour was found. Experimental values were found to be close to theoretical expectations at T3. At CT2 however, a lower absorption than predicted was measured. The idea of non monochromatic neutrons at this beam-line has been proposed as an explanation. A 30 % 1st harmonic contamination produced in the monochromator would be enough to match the experimental results.

A thickness gradient within the deposition chamber was measured with SEM and confirmed with the Direct Neutron Absorption measurement. Four different types of blades were defined according to the coating profile. The

outer sections of the chamber showed a higher gradient (13 % along the blade length) than the central regions (only a 5 %). This information is taken into account for the Multi-Grid detector mounting as it will be explained in Section 7.4.

Neutrography shows a non-asymmetry not detected with SEM or Direct Neutron Absorption. Also, values found for $\Sigma_{tot}^{^{10}B}$ are lower than expected. A reason could be the non-homogeneity of the scattered neutron beam impinging the detector. Improvements in the set-up should be implemented to correct these effects probably coming from a non-homogeneous (neither in shape nor in wavelength) scattered beam.

Chapter 7

Detector Characterisation

7.1 Introduction

The characterisation of the Multi-Grid detector was accomplished by a set of different experiments. Parameters such as detection efficiency, uniformity, γ-sensitivity, stability, ageing, etc. were measured.

Few preliminary tests were made to estimate the influence of the cross-talk and the wall-effect. Plateau measurements were performed and operational voltages were set for two different stopping gases used.

A new method to accurately measure the neutron detection efficiency was developed. It was used to measured the Multi-Grid efficiency for incoming neutrons of $\lambda = 2.5$ Å as a function of the detector depth and the thickness of the individual layer. The exponential attenuation of the neutron beam was found and compared with the expected value. Other results of the MC simualtion seen in Chapter 4 were used and compared to the measurements.

Results of the thin film characterisation analysed shown a thickness gradient in the the boron-containing layer coated onto the aluminium blades. This information was used for a optimised mounting of the blades in the grids.

Another important requirement of PSD in NSS is the γ-sensitivity. It was measured for a broad range of energies with two different γ-sources.

Long-term stability of the detector was study under two different types of incoming neutron fluxes: moderate and extreme. Results of these measurements show the stability of the detector and the ageing. The two different gas species (CF_4 and Ar-CO_2) were studied.

7.2 General Characterisation

Plateau measurements are needed to set the operational voltage of the detector for the two different gas species used. Several PHS and signal shapes are studied to properly understand phenomena such as the cross-talk between grids or the wall-effect.

7.2.1 Plateau

As it was seen in Section 3.2, when plotting the counting of a gas detector as a function of the applied voltage the different regions of operation can be distinguished. The region where the counting is constant for a range of electric field values is called plateau. Due to the small gain variation, the operational voltage of the detector is commonly placed in this zone.

The already studied MG-12 detector was used for this experiment. It was filled with two different gas species @ 1 bar: CF_4 and Ar-CO_2 (90-10 %). A coincidence set-up is used: events are accounted when signals are detected simultaneously in a grid and one of the 15 wires in depth. Results are shown in Figures 7.1a and 7.1b respectively.

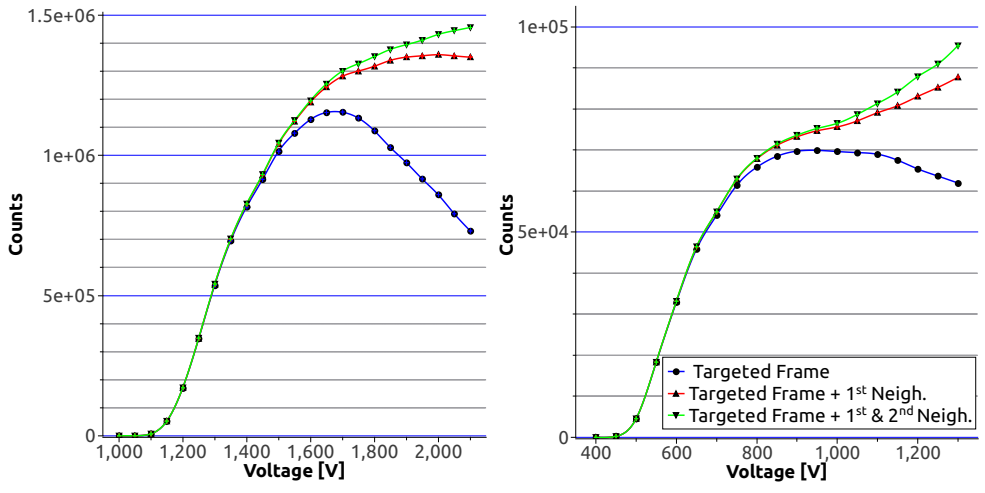

(a) (b)

Figure 7.1: **(a)** Plateau measurement of the MG-12 prototype filled with CF_4 @ 1 bar. **(b)** The same measurement was performed using Ar-CO_2 @ 1 bar.

Three curves are plotted:

1. On blue, the counting on the targeted grid (beam placed at the middle

of the voxel).

2. On red, 1. + first neighbouring grids (± 1).

3. On green, 2. + second neighbouring grids (± 2).

The plateau for CF_4 is shown in Figure 7.1a. The counting at the targeted grid shows a rapidly increment until 1600 V. At that point it reaches a maximum and decreases for higher values of the applied potential. The curves of the neighbouring grids continue to increase and reach a saturation region around 2000 V. This phenomenon is due to the cross-talk between grids already discussed in Section 5. At high values of the applied voltage, the capacity coupling between grids creates signals in the neighbouring grids. In some cases, when an event takes place these signals show a faster rising edge than the primary signals in the targeted grid as it is shown in Figure 7.2b. The acquisition system misaddresses the event assigning it to the neighbouring grid.

A similar behaviour is found for Ar-CO_2 in Figure 7.1b. The main difference is related with the applied voltage. As studied in Section 3.2.2 Ar-CO_2 has a lower gas amplification threshold. Lower applied voltage is needed to start the gas amplification. Operational voltages were set at 800 and 1600 V for Ar-CO_2 and CF_4 respectively. For these numbers the counting on the first and second neighbours over the targeted grid is shown in Table 7.1.

Gas	**Voltage [V]**	**1st. N./T. [%]**	**2nd. N./T. [%]**
Ar-CO_2	800	3.09	3.33
CF_4	1600	5.54	6.02

Table 7.1: Percentage of the counting measured in the first and the second neighbour grids divided by the counts in the targeted grid for different voltages.

7.2.2 Cross-Talk

As seen above, an important percentage of events is detected in the neighbouring grids. With an appropriate algorithm this effect can be used to increase the position resolution along the dimension of the wires.

Pulse shapes of different grids for a standard event are shown in Figure 7.2a. The collimated beam was targeting at the center of grid G6. The pulse with highest amplitude corresponds to this grid. First neighbouring grids (G5 and G7) also show a similar pulse shape but with a lower amplitude and higher signal-to-undershoot ratio. Second neighbouring grids (G4 and G8) are further away from the interaction point. As explained in Section 5.2, the main contribution to these signals comes from the capacity coupling between frames.

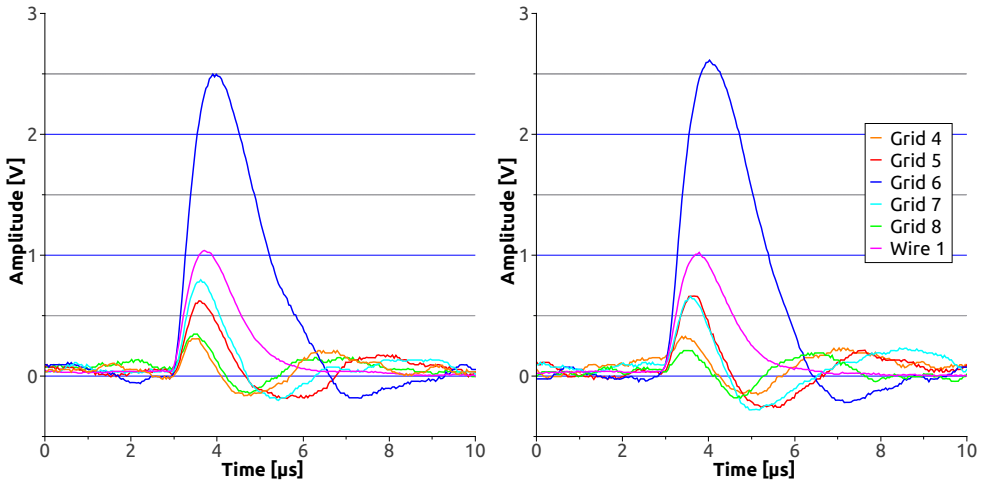

(a) (b)

Figure 7.2: Pulse shape of the different grids in the Multi-Grid detector during an neutron event.

In Figure 7.2b however a different type of event can be seen. Signals from the neighbouring grids (specially G4) show a relatively high noise level. At the moment when the rising edge at the wire channel crosses the threshold (80 mV), the amplitude in G4 is higher than on G6 and has already crossed the threshold (240 mV). Since in the coincidence mode is the time between the X and Y signals once they have crossed the threshold, which defines a positive event, in this case the event will be accounted on G4 instead of G6. A higher threshold value on the grids would help to reduce this effect. In

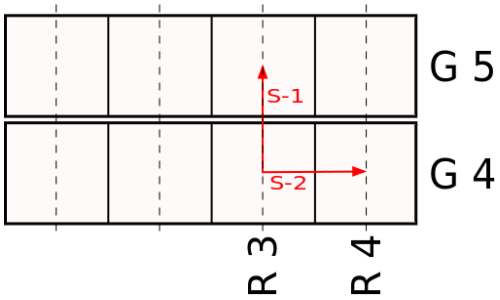

Figure 7.3: Scheme of the two fine scans performed on the MG-12 detector. Scan 1 is performed along the direction of the wire while Scan 2 is done along the same grid.

order to quantify the cross-talk, a set of measurements was performed at the CT2 beam-line. The MG-12 filled with CF_4 @ 1 bar was used. The middle

of one voxel was targeted with a collimated beam (1.5 mm × 1.5 mm). A fine scan was performed along the direction of the wire until the edge of the cell, corresponding with the neighbouring grid, was reached. A scheme of the scan is shown in Figure 7.3. PHS obtained for Scan 1 are plotted for both, the targeted (G4) and the neighbouring grid (G5) in Figures 7.4a and 7.4b, respectively.

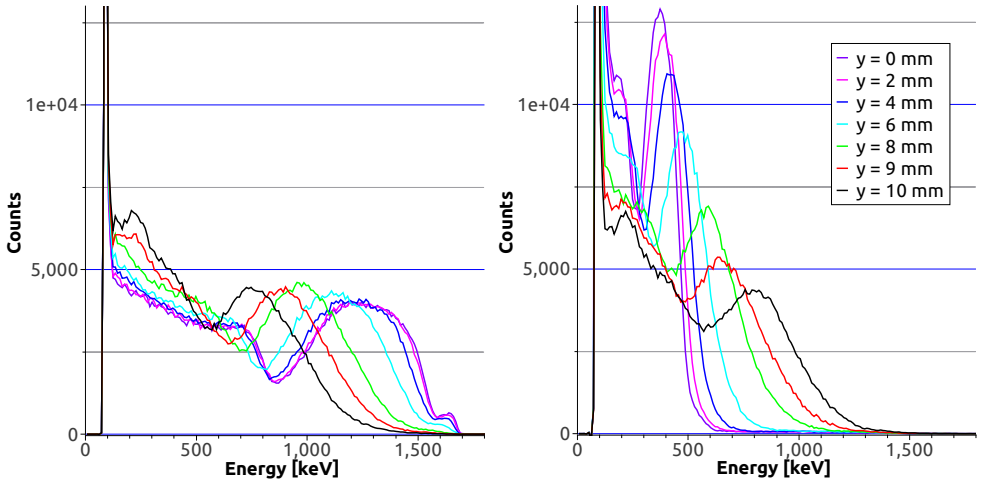

(a) (b)

Figure 7.4: **(a)** PHS obtained for several points of the scan in the targeted grid. **(b)** For the same points, the PHS measured in the neighbour grid are shown.

For the targeted grid, Scan 1 positions y = 0 and y = 2 show a standard PHS behaviour already discussed in Section 1.3. As the collimated beam moves away from the middle of the cell a shift towards lower energies is found. In the extreme case of y = 10, the beam is placed at the edge of the cell, the distribution has further compressed and a lower number of events have been recorded.

For the neighbouring grid, the distributions in Figure 7.4b show a different behaviour. A much sharper peak centred at ∼ 400 keV is found for y = 0 and y = 2. Together with it another peak is placed at lower energies (≈ 200 keV). When moving towards the edge, the mentioned peaks get wider while moving towards higher energies. The two distribution of the reaction fragments produced in the most probable branch ratio can be distinguished for y = 8. The same distribution that was seen in the targeted grid for y = 10 is found in this grid for the same position.

The relation between signals measured on one grid or the other can also be presented in a different way. The amplitude measured on the targeted grid

is plotted against the amplitude on the neighbouring grid for several points along Scan 1 in Figure 7.5.

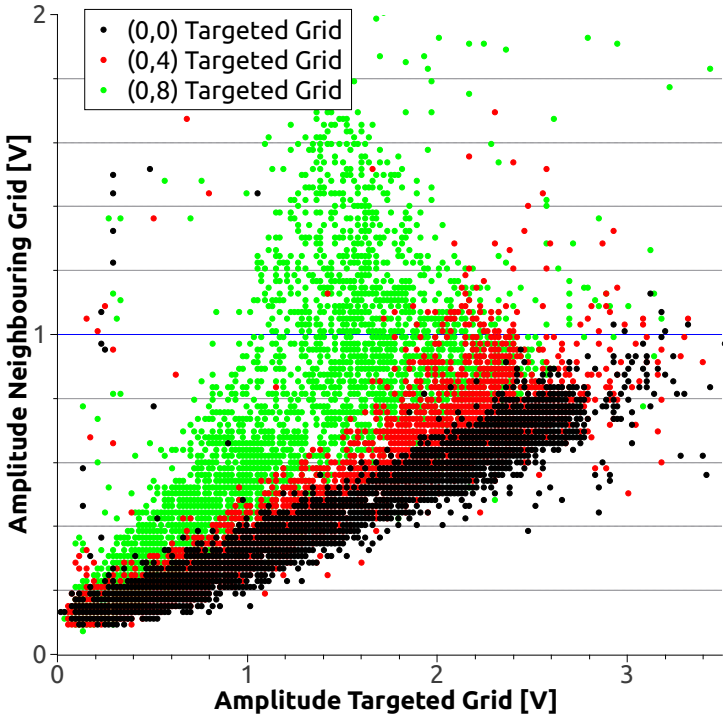

Figure 7.5: The maximum amplitude of the targeted grid versus the neighbouring is plotted for three different positions of the Scan 1.

When placed at the center of the cell on the targeted grid, a linear relation between the events measured on G4 and the ones G5 is found. Either a capacitive coupling or the direct induction created by the moving charge could be the cause of these signals on the neighbouring grids. When moving the beam towards the edge (y = 4) the major part of the events remain on a linear distribution. However at high amplitudes a small shift towards higher neighbouring amplitudes can be seen. Finally, at y = 8, two different distributions are found. The first one at low amplitudes which approximately follows a linear behaviour. Then at medium and high amplitudes a much more spread distribution is measured. Note that the distance to the edge is shorter than range of some of the fragments. Events splitting their charge between the two grids are possible. At could partially explain this behaviour.

Efficiency measurement is fully explained in Section 7.3. However, the detection efficiency was measured per each point of the Scan 1. Results are presented in Figure 7.6.

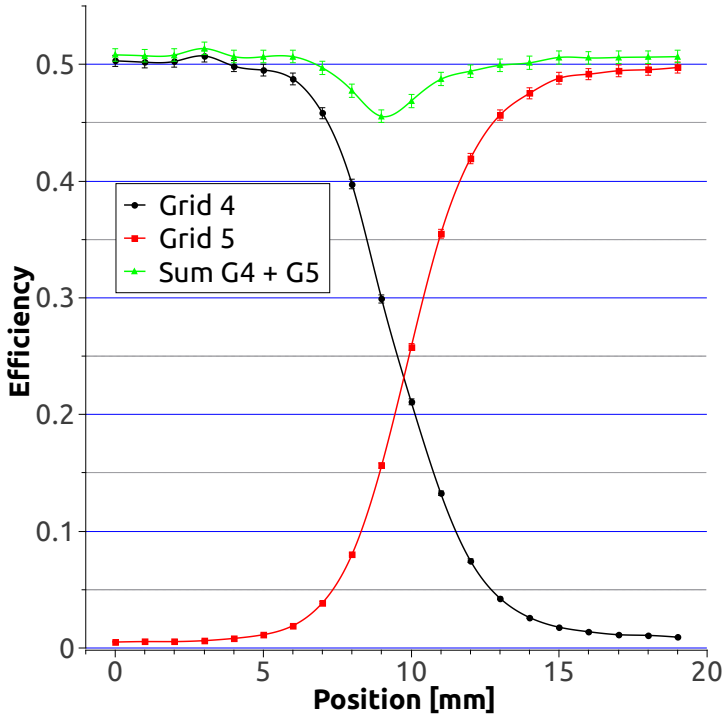

Figure 7.6: Detection efficiency was measured simultaneously for targeted and neighbour grids at every point of the Scan 1.

Values in the middle of the studied voxels are maximal and similar in both grids. However when travelling from the centre of the cell towards the other grid a drop in efficiency is produced. It starts at approximately 4 mm from the edge. This distance corresponds with the maximum range of the α-particle travelling in CF_4 @ 1 bar (as seen in Figure 4.3b).

The sum of both efficiencies is also shown in Figure 7.6. When the collimated beam is far from the edge its value does not differs from the value of the targeted grid. However, when the beam targets positions close to the edge the cross-talk between grids attenuates the drop in the detection efficiency and the value for the sum only decreases by $\sim 5\%$.

Spatial Resolution Improvement

After what it was seen in Figure 7.5 the idea of using this cross-talk between grids as an advantage of the Multi-Grid geometry came up. In Figure 7.7, the amplitude measured on the targeted grid plus first and second neighbouring grids is plotted versus wire amplitude.

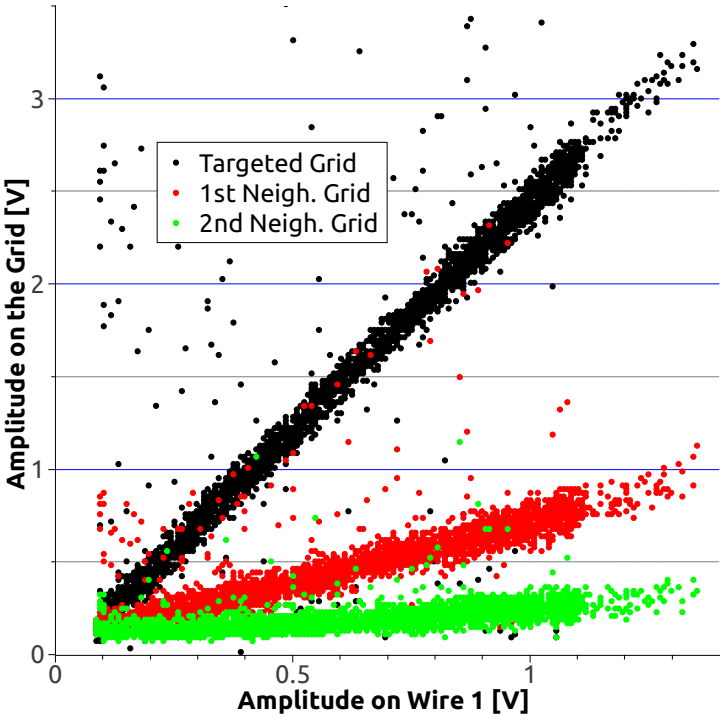

Figure 7.7: Maximum amplitude measured on the targeted and 1st and 2nd grids versus maximum amplitude on the Wire 1.

This signal multiplicity for a single event seen in Figure 7.7, can be used to improve the Multi-Grid spatial resolution along the wire dimension. As it was studied in Section 1.2.1, the pixel size of IN5 is 2.5 cm × 2.5 cm which is already slightly larger than the Multi-Grid (2 cm × 2 cm). This improvement however could lead to the construction of thicker grids (and therefore wider aluminium blades) and therefore a reduction in the number of grids to be used to cover the same active area. Using a simple localisation algorithm, based on the center of gravity between different frames, some preliminary results were found and are shown in Figure 7.8.

For the two points plotted in Figure 7.8 and improvement in the resolution is obtained. In the case of the position x = 4 mm, although the broad distribution found, the estimated Full Width Half Maximum (FWHM) was found to be 1.01 cm. This is half of the detector spatial resolution (which is defined by the cell dimension for an individual readout). When the beam targets the edge of the cell at x = 10 mm, a greater improvement in the spatial resolution is obtained: it was found to be 0.3892. This is a factor of 5 better resolution that before.

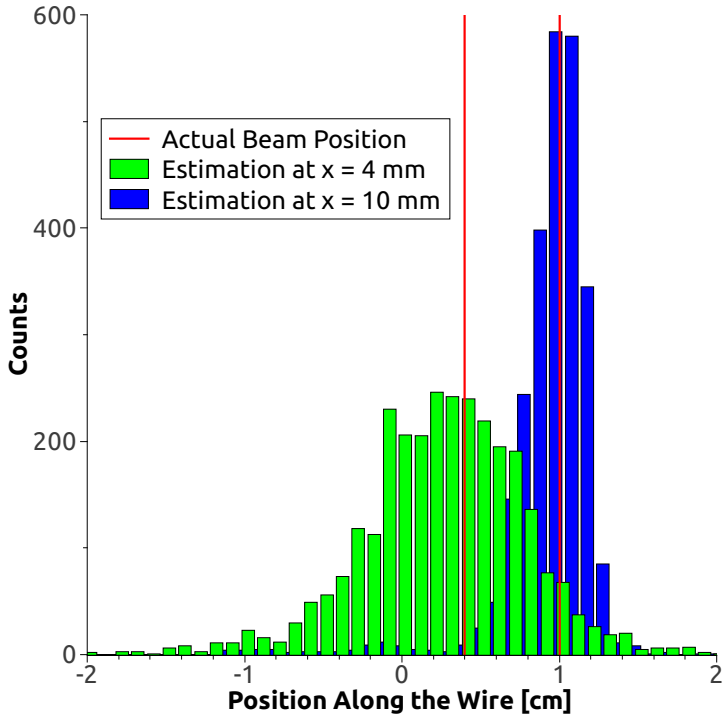

Figure 7.8: Two different distributions estimated for x = 4 and 10 mm from the center of the cell respectively.

7.2.3 Wall-Effect

When scanning along the same grid a different phenomenon can be studied: the wall-effect. The path of Scan 2 was shown in Figure 7.3. The targeted grid was G4. PHS measured while moving from the targeted row (R3) to the neighbouring one (R4) are shown in Figures 7.9a and 7.9b respectively.

The PHS obtained for the three first points at the targeted row (x = 0, 2 and 4) are similar: no effect of the wall can be seen. However, when the collimated beam moves further towards the corner, higher amplitude signals start getting lost at x = 6. This effect increases for positions closer to the wall. At the edge, x = 10, the MC simulation shown in Figure 4.14 estimated a PHS corresponding to approximately half of the one obtained at the middle of the cell. This effect is seen in Figure 7.9a for the lithium fragments which show amplitudes at the border which are $\approx$ half of the ones at the middle of the cell. For the more energetic α-particles however the ratio between this two positions seems to be closer to 30% than to 50%.

Neighbouring grid shows the same PHS than the targeted one at the corner

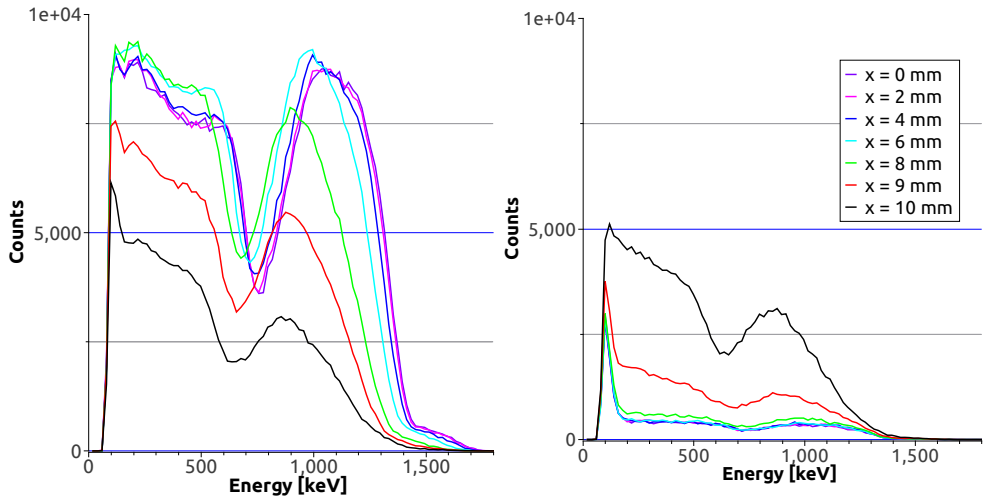

(a) (b)

Figure 7.9: **(a)** PHS obtained at the targeted row for different points of Scan 2. **(b)** For the same points, the PHS measured in the neighbouring row.

of the cell (x = 10). The events produce here are split into both rows due to the size of the neutron beam. This also applies for x = 9 which shows a higher counting than other positions. The rest of the measured positions show a measurable PHS due to the fact that the wire is collecting signals all along its length which covers 12 grids. This effect is completely suppressed for the detection measurement studied below which used a coincidence set-up.

In the same way that for the cross-talk, the detection efficiency is measured per each point of the Scan 2. Results can be found in Figure 7.10.

Detection efficiency at the center of the cell shows a relatively uniform distribution. It starts dropping at approximately 2 mm from the wall. At x = 10 the value for the sum of efficiencies is minimal ($\sim$ 33 %).

This result is in relatively good agreement with the MC simulation studied in Section 4.4. The drop in detection efficiency was however expected to start at positions closer to the wall. In this case and due to the size of the neutron beam the wall-effect can be seen from more than 2 mm apart. Another effect of the relatively large size of the beam is the lower drop in the efficiency compared with the expected value.

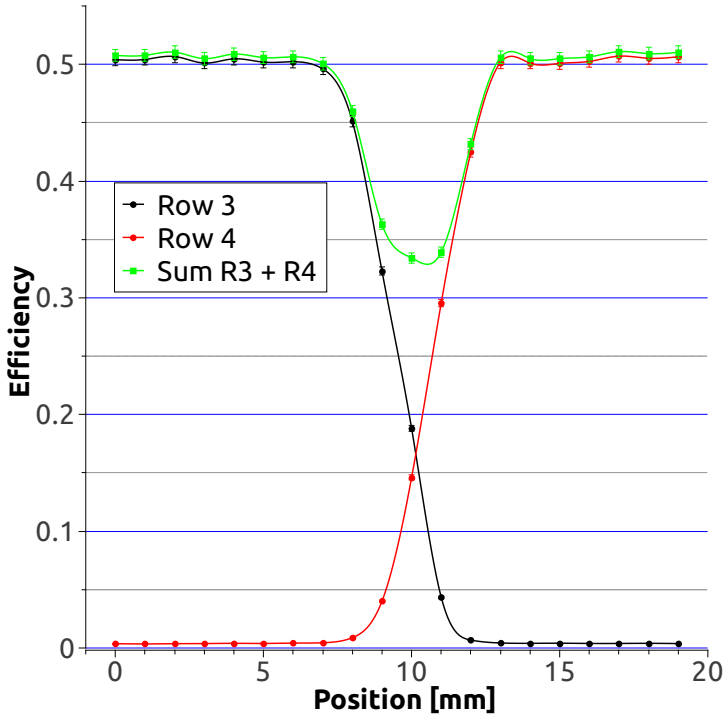

Figure 7.10: Detection efficiency measured simultaneously for the targeted and neighbouring row along the points of Scan 2.

7.3 Efficiency

Experiments took place at CT1 and CT2 beam-lines. Three X-Y slits were used to collimate the neutron beam which impinges the detectors to a size of 2 mm × 2 mm. A beam-monitor was placed before the slits to control the stability of the neutron flux provided by the nuclear reactor.

7.3.1 Reference Measurement

The ^{3}He-based detector shown in Figure 7.11a was used to estimate the neutron flux for the efficiency measurements. Its internal structure consists in 37 hexagonal tubes (8 mm diameter). The gas mixture of the detector was set in 3.5 bar of ^{3}He and 1.25 bar of CF_4 acting as a gas quencher.

Measurements are done by targeting the center of the middle row of tubes. When plotting the cumulative counts as a function of the number of tubes in depth (i.e. along the z axis), the behaviour shown in Figure 7.11b is found. By applying a fitting curve to the data, an experimental estimation of the total

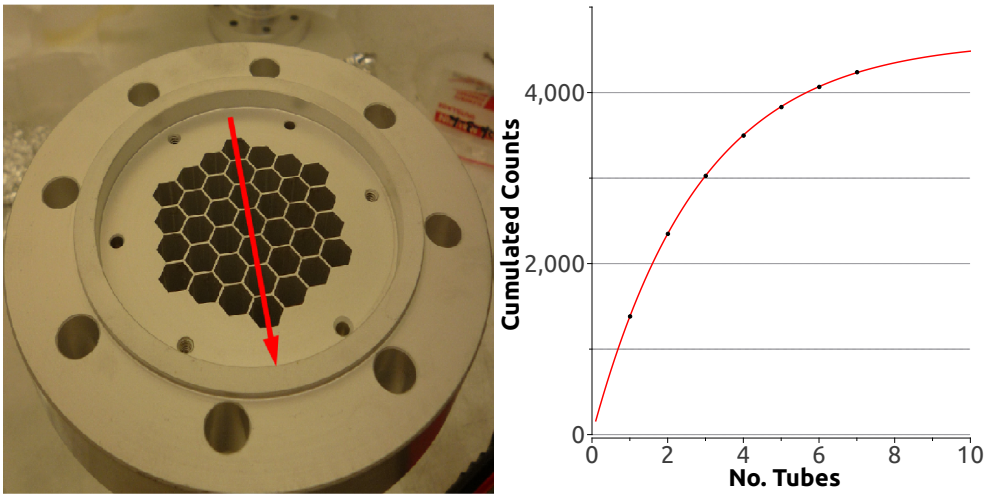

(a) (b)

Figure 7.11: **(a)** The ^{3}He-based reference detector. The 37 hexagonal tubes, 8 mm diameter can be seen. The neutron beam impinges on the central row of tubes. **(b)** Flux estimation - the seven points are cumulative counts in depth for the reference detector. The exponential fit gives an experimental estimation of the total flux.

neutron flux, F_{est}, can be determined. The fitting curve is defined as:

$$y = a \cdot (1 - e^{-(x \cdot b)}), \tag{7.1}$$

where a = $4.62 \cdot 10^3$ and b = 0.3554, are the fitting parameters.

The flux for the first tube, the most exposed one, is 1387 neutrons/s (over the size of the collimated neutron beam). The effect of the dead time in this detector reduces the neutron flux by less than 0.1%.

7.3.2 Multi-Grid detector

The same set-up as described previously is used. The reference detector is removed. Neutrons now impinge on the middle of a voxel row of the Multi-Grid prototype filled with 1 bar of CF_4. B_4C shielding is used to reduce the neutron background. Thresholds are set above the electronic noise level. Events are recorded when two signals, one from the fired grid and the other from any of the 15 wires, are measured in coincidence. Total counting per wire, N_{wire}, is then compared to the total flux estimated by the reference detector,

F_{est}, over the same acquisition time.

$$\varepsilon_{wire} = N_{wire}/F_{est}. \tag{7.2}$$

Efficiency per wire can be determined and is shown in Figure 7.12. The exponential attenuation of the neutron beam in the detector is observed.

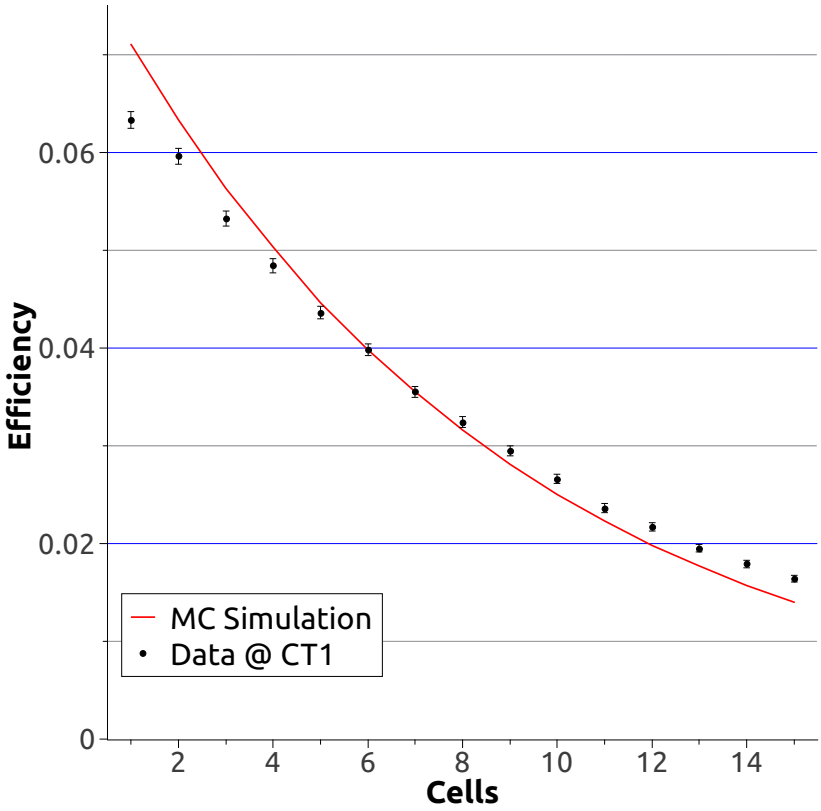

Figure 7.12: The efficiency per cell in depth. The exponential attenuation of the neutron flux is clearly visible. As expected, the first and last tubes, with only one boron layer, show a lower efficiency than the rest. The overall efficiency is calculated as the sum of individual wire efficiencies.

The overall efficiency is obtained as the sum of each wire: $\varepsilon_n = \Sigma_1^{15}\varepsilon_{wire}$. A value of $\varepsilon_n = 53.09\% \pm 0.77\%$ (stat.) was found. This result is to be compared with the 53.47% efficiency found for the MC simulation shown in Figure 4.6.

Although the maximum efficiency is found to be in good agreement with the expected value from the MC simulation the shape of both exponential attenuation show an important discrepancy. Possible reasons for this are discussed now.

7.3.3 Layer Thickness

As shown in Chapter 5, grids using six different layer thickness were used for the MG-12 detector.

The experimental results are shown in Figure 7.13 together with the simulated curve seen in Figure 4.9. When plotting the detection efficiency versus the layer thickness the maximum of the distribution is found around 1 μm.

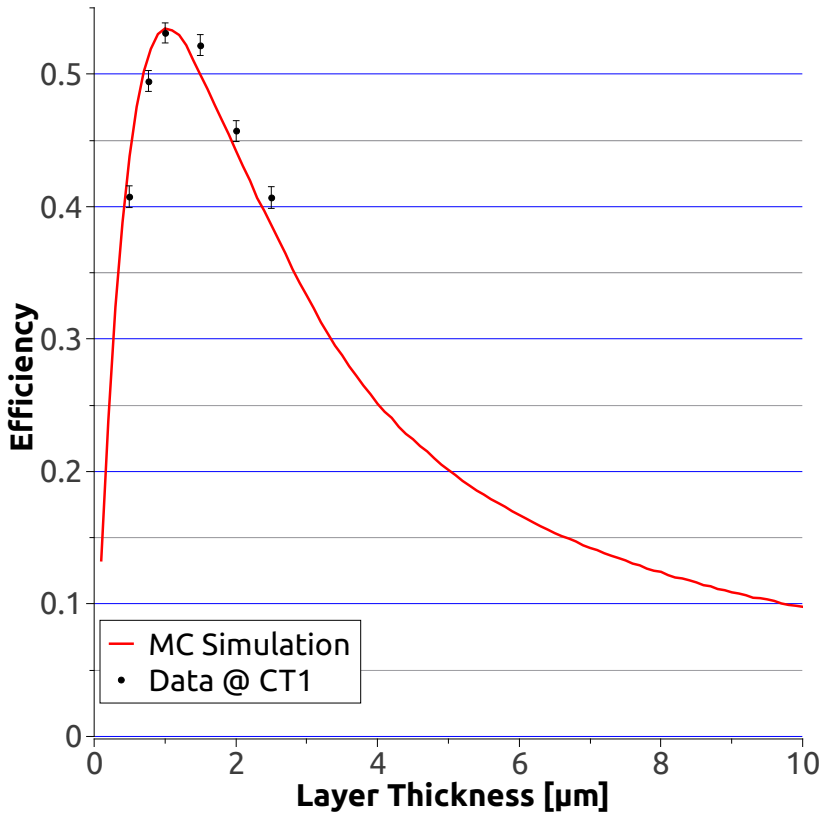

Figure 7.13: Detection efficiency as a function of the individual layer thickness for the MG-12. Five different coating thickness were used. For comparison, the MC simulation shown in Figure 4.9 is replotted here.

A discrepancy was found between the measured values and the MC simulation. Possible explanations are studied.

7.4 Uniformity

The variation of coating thickness among the various blades used is measured using Si wafers mounted in different positions on the sample holder within the sputtering chamber. A 13% gradient in the coating thickness along the length of the blade was measured using thin-film characterization techniques, as seen in Section 6.3.1.

7.4.1 Variation measurement

Based on the results shown in Figure 6.4, several different types of frames were assembled based on the maximum gradient expected in the blades used. In some frames, blade orientation was alternated, so that for each detector cell, the thickness (and, therefore, efficiency) varies in opposite directions in the front and rear coating. This largely cancels the overall effect on efficiency across that frame. In a number of the frames, however, this compensation was deliberately not implemented. Also the blades with the greater gradient were used in these frames. Therefore a 13% variation in total amount of ^{10}B from one side of these frames to the other is expected.

MC simulations show that varying the coating thickness by up to 13% around its optimal value (1.0 μm) yields an efficiency variation of $\sim \pm$ 1%. To verify this effect, a uniform scan of the detector was performed. An Am-Be neutron source was translated along the detector at a constant rate over a long time (several days). The number of counts in each voxel was recorded as a function of time. Each grid is read out by an individual amplifier, and a signal recorded when coincident with a wire signal. A constant threshold was used in all amplifiers and therefore grid-to-grid count variation is dominated by the effect of the amplifier gain. This, however, is not an issue when comparing the rates in different voxels of the same grid. A count normalization was performed for each grid to the mean value. A deviation from a uniform response was found from one side of the frame to the other in grids where the blade orientation was not alternated (grids 59 to 72). This variation was found to be $\Delta_{uni}^{59-72} = \pm$ 1%, as is shown in Figure 7.14, in good agreement with the expected value based on the coating gradient and the efficiency simulation described above.

Using the simple idea of alternating blade direction (frames 30 to 58) a variation of $\Delta_{uni}^{30-58} = \pm$ 0.2% along the frames was achieved. The effect of the gradient in the boron carbide coating was reduced by a factor of 5. It should be noted that the effect of the electronics is excluded from this analysis.

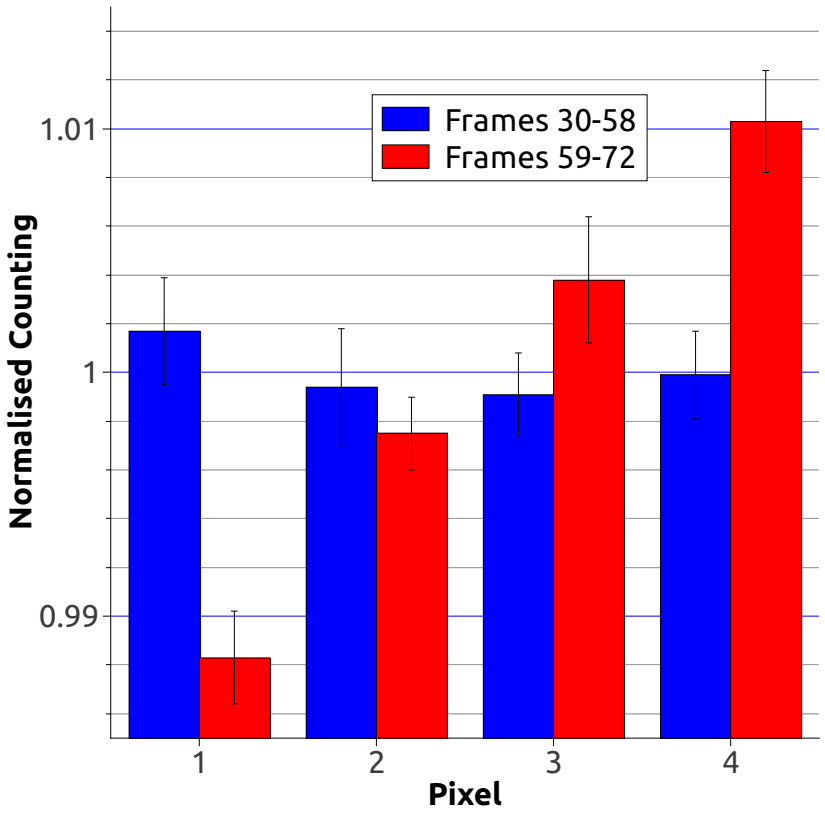

Figure 7.14: To suppress the gain differences between grids, a normalization was performed. Variation in the efficiency along each grid was measured. Variation clearly improved when the blade direction was alternated: $\Delta_{uni}^{30-58} = \pm 0.2\%$.

7.5 Gamma sensitivity

The γ-ray sensitivity of the Multi-Grid detector was measured using two different γ-ray test sources. They were placed 1.2 cm away from the square single voxel surface (2 cm $\times$ 2 cm). The solid angle coverage, Ω, was $\sim$ 13% of the unit-sphere surface. For each specific γ-ray source, the flux, ϕ, at the surface of the voxel is given by:

$$\phi = A \cdot I \cdot \Omega \tag{7.3}$$

where A is the activity $[Bq]$ of the source and I the intensity of the specific γ-ray under study. As an example, for the 81 keV γ-ray present in the ^{133}Ba source with an activity of $1.8 \cdot 10^5$ Bq and an intensity of 32.9% [50], its flux at the voxel surface is given by: $\phi = 1.8 \cdot 10^5$ Bq $\cdot\, 0.329 \cdot 0.13 = 7.7 \cdot 10^3$ Bq. Two γ-ray test sources (^{133}Ba and ^{60}Co) covering a wide energy range (from tens of keV up to the MeV regime) were used to evaluate the γ-ray sensitivity. For a

given value of the bias voltage and energy threshold, the gamma-ray efficiency, ε_γ, can be calculated as the ratio between the number of events detected in the voxel, N, and the incoming γ-ray flux:

$$\varepsilon_\gamma = N/\phi. \tag{7.4}$$

In Figures 7.15a and 7.15b, the single voxel γ-ray efficiency, ε_γ, is shown as a function of the detector bias voltage for both CF_4 and Ar-CO_2.

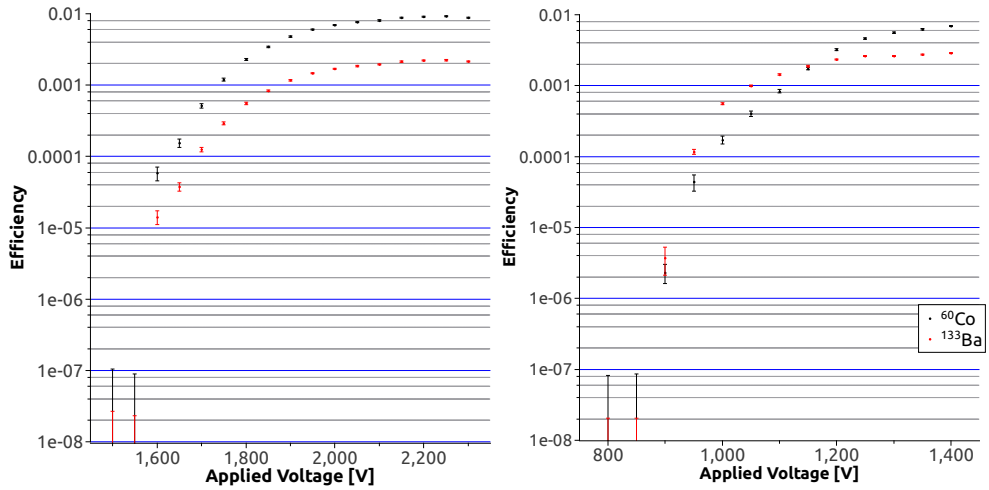

(a) (b)

Figure 7.15: **(a)** γ-ray efficiency as a function of the bias voltage of the Multi-Grid detector filled with CF_4 @ 1 bar. Different energy ranges are studied with two different γ-sources. **(b)** The same set-up was used. The Multi-Grid detector was now filled with Ar-CO_2 @ 1 bar.

The lowest voltage point is an upper limit estimate of the Poissonian error on the background. A 24-hour measurement was performed in order to evaluate the γ-ray sensitivity at this voltage with a consequent statistic inside the background fluctuations. In order to improve this evaluation a better signal-to-background ratio is necessary. For the same gain as that used for the neutron detection efficiency, the gamma sensitivity is found to be: $\varepsilon_\gamma \leq 5 \cdot 10^{-5}$. Note that a higher γ-rejection ($\sim 10^{-7}$) can be achieved at the cost of lower ($\sim 10\%$) neutron efficiency, as can be deduced from the plateaus shown in Figures 7.1a and 7.1b.

7.6 Counting Rate

As it was shown in Section 3.4.3, two different types of behaviour for the dead time are possible for a radiation detector: paralysable and non-paralysable. Theoretical expressions for the expected counting rate were obtained as a function of the detector dead time. As it was discussed in Subsection 5.4.1, the front-end electronics play an important role in the counting rate capability of gaseous detectors in general. The time constant of the amplifier load-circuit is used as the detector dead time. The two values studied (2 μs for the electronics used and the optimal of 250 ns) are used here to estimate the losses for the Multi-Grid detector. Calculations of the expected rate as a function of the real rate are shown in Figure 7.16.

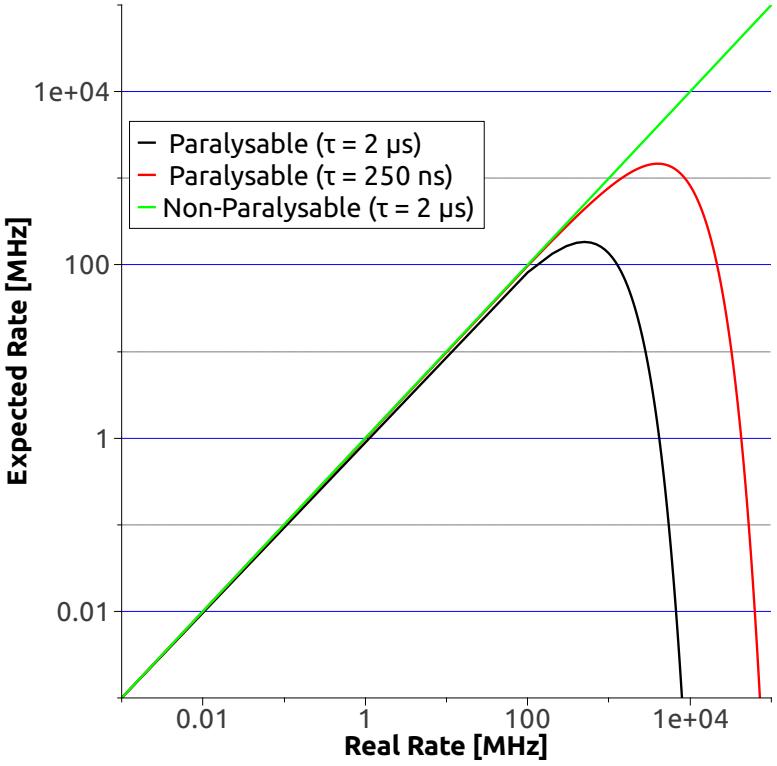

Figure 7.16: Theoretical curves for the expected counting rate as a function of the real rate for 3 different situations: paralysable and non-paralysable for two different dead times.

For relatively low values of the counting rate no significant difference was found between the two behaviours in the theoretical curves. This argument holds until $\approx$ 100 MHz where the paralysable detector with τ = 2 μs starts losing its capabilities.

In the case of the Multi-Grid detector lower counting rates than expected were measured. The relatively low bandwidth of the front-end electronic limited the counting rate capabilities of the detector.

7.7 Time Resolution

Another important requirement for ToF spectrometers is the time resolution of the detectors. As it was seen in Section 1.2.1, the limiting factor is due to the chopper system. Detector time resolution however needs to be optimised in order to match this value.

As seen in Table 2.1, typical velocities for thermal neutrons go from ≈ 1 to 10 km/s. As a first approach to the time uncertainty of the detector the travelling time of the neutron can be used:

$$t_{trav} = \frac{d}{v}, \tag{7.5}$$

where d is the thickness of the detector and v the velocity of the incoming neutron. As seen in Chapter 5, the Multi-Grid detector thickness is split into 15 tubes, each being 1 cm thick. These numbers leads to a t_{trav} between 1 to 10 μs.

Besides that, to the total time the movement of the reaction fragments in the gas has to be added. This contribution however is, on average the same on both sides of the cell. So no time uncertainty is added. Also, the movements of the electrons provoking the first avalanche is, on average, the same on both ends of the cell. In any case these contributions are much smaller than t_{trav}.

7.8 Stability & Ageing

As it was discussed in Section 1.2.1, the long-term stability of the PSD is the principal requirement for the instrument reliability. In this context, to study the behaviour of the Multi-Grid detector under two different rates for relatively long exposition times will show its capacity.

7.8.1 Stability

The stability of the Multi-Grid detector was measured at the CT1 beam-lined using a collimated neutron beam. PHS were taken every 10 minutes over a period of several days. The neutron flux at the detector window was $\approx$

110 s^{-1} cm^{-2}. Variations on the gain of the detector are studied as a function of time, or equivalently as a function of the number of events produced per mm of the wire.

Two different gases were used: CF_4 and Ar-CO_2. Results can be found in Figures 7.17a and 7.17b respectively.

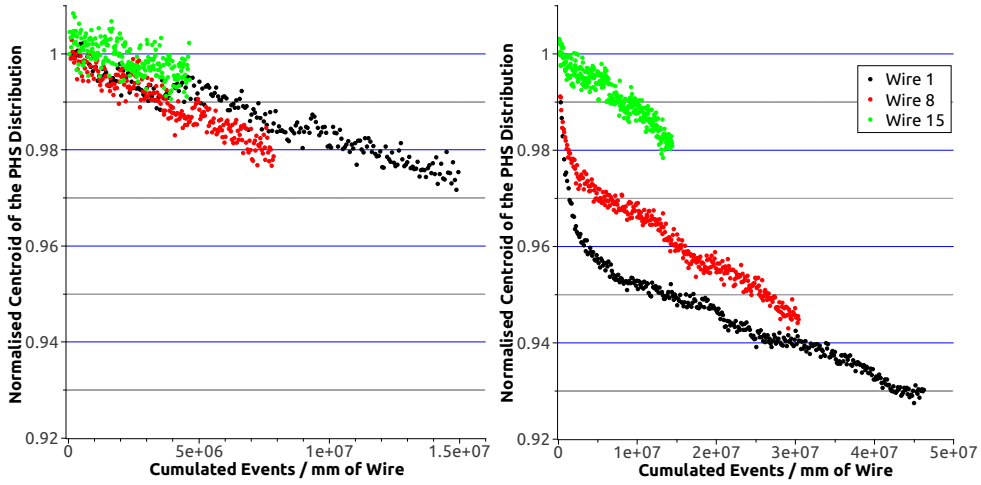

(a) (b)

Figure 7.17: **(a)** The normalised centroid of the PHS distribution plotted against the number of events accounted on the first and the last wire of the detector. The stopping gas was CF_4 @ 1 bar **(b)** In the case of Ar-CO_2 @ 1 bar a longer exposition time was analysed.

According to the results shown, for moderated neutron flux, CF_4 shows a better stability. Three different distributions as a function of the neutron flux are shown corresponding to three different wires. Due to their different position along the depth of the detector, different rates are measured. A decrease of less than 2% after $1.5 \cdot 10^7$ events was measured for the wire under the higher rate.

A similar behaviour is found for Ar-CO_2. Measurements went on for a longer exposition time. A more important effect $\approx$ 7% was measured after $\approx$ $5 \cdot 10^7$ events.

7.8.2 Ageing

Problems related with the ageing of detectors working with CF_4 as filling gas can be found in the literature []. Molecules formed during the gas amplification chemically attack the wire causing a degradation in the signals. As seen in

Section 3.2.2, a typical sign of this ageing is given by a gain reduction in the detector. This was already studied for both stopping gases under a relatively moderated neutron flux in Section 7.8.1. If the neutron flux is increased to $\approx 6 \cdot 10^5$ s^{-1} cm^{-2}, a closer picture to the long-term effects in the detector can be accessed. Results can be found in Figures 7.18a and 7.18b respectively.

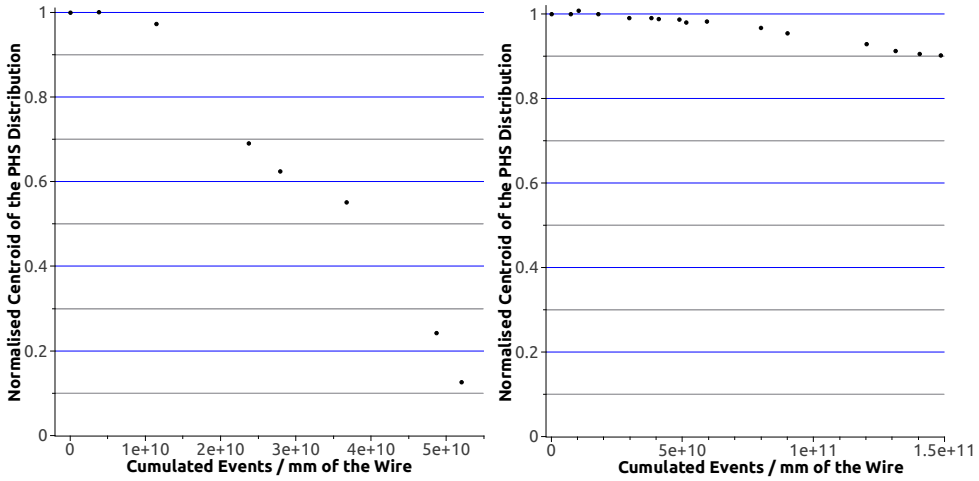

(a) (b)

Figure 7.18: **(a)** The normalised centroid of the PHS distribution is plotted against the number of events. Stopping gas used was CF_4. **(b)** The normalised centroid of the PHS distribution is plotted against the number of events. Stopping gas used was $ArCO_2$.

As it was expected, a clear shift of the PHS distributions towards lower energies is found. Signals from the this wire progressively lose amplitude. A 80% of the detector gain has been lost after $\approx 5 \cdot 10^{10}$ events detected per millimetre of the wire.

When the stopping gas was change to Ar-CO_2 and a similar flux was used for a longer exposition time, the ageing found only decreases the gain by a 10%. The total number of events detected per millimetre of the wire was $\approx 1.5 \cdot 10^{11}$.

7.9 Conclusion

A characterisation study of the Multi-Grid prototype, which included an accurate flux estimation measurement based on a ^{3}He-reference detector, was performed. The detection efficiency was found to be $\epsilon_n = 53.09 \pm 0.54\%$ (stat.)

for incoming monochromatic neutrons of 2.5 Å. This value is in agreement with the MC simulation, which predicted an efficiency of 53.47%.

Thickness variations in the boron coating of up to 13% along the aluminium blades were measured with thin-film characterisation techniques. This result was further confirmed by neutrography, The thickness gradient produced an efficiency variation of $\Delta_{uni} = \pm$ 1% along each grid. By correctly orienting these blades, an improvement was achieved. These results prove that potential constraints regarding the coating uniformity can be overcome.

γ-sensitivity tests were performed for a broad range of energies (from tens of keV to a few MeV). The result obtained at the same gain value as for neutron detection efficiency measurements was $\epsilon_\gamma \leq 5 \cdot 10^{-5}$.

Long-term stability has been pointed out as one of the most important requirements for the detector of a ToF instrument. Two different types of gas species were tested: CF_4 and Ar-CO_2. The Multi-Grid detector was under a moderated neutron flux over a long period of time. Small variations in the gain (measured by the shift of the PHS towards lower energies) were observed. For the moderated neutron rate used, CF_4 shows a better stability than Ar-CO_2.

If the neutron flux is further increased the loss in the detector gain becomes critical. In this sense, a clear difference in the performance of the two gas species is found. For a similar neutron flux, CF_4 shows a decrease in gain of $\approx$ 80% whilst in the case of Ar-CO_2 it only drops by 10%.

Conclusions

The needs of neutron detectors in NSS were defined. Different requirements on detection efficiency, uniformity, γ-sensitivity, long-term stability, etc. were studied. The present ^{3}He shortage prevents the use of this technology for large detector arrays. Due to their specifications, ToF instruments are the most affected by the present situation. Different alternatives pointed out by the scientific community were analysed. Boron-lined converters coupled with gas proportional counters were chosen for this study.

Different types of interactions occurring to the various particles involved in neutron detection (neutrons, electrons, ions and photons) were studied. Basic characteristics of gaseous detectors were reviewed.

A MC simulation was performed in order to optimise several important parameters needed for the design of the proposed detector. One of this parameters was the individual layer thickness. The optimal value was found to be $\approx$ 1.0 μm for a 30-layer configuration and $\lambda = 2.5$ Å. Other effects such as the wavelength dependence of the detection efficiency or the wall-effect for several stopping gas pressures were simulated.

The Multi-Grid concept was introduced. The different prototypes used in this work were study and their specifications reviewed. Front-end electronics were analysed and possible optimisations pointed out.

A complete study of the boron converters was done. Two different complementary approaches were used: thin film characterisation and neutrography. Information on the ^{10}B-concentration, mass density, layer thickness, concentration of contaminants, etc. was obtained. Results helped to understand the performance of the Multi-Grid detector.

A characterisation study of the Multi-Grid prototype, which included an accurate flux estimation measurement based on a ^{3}He-reference detector, was performed. The detection efficiency was found to be $\epsilon_n = 53.09 \pm 0.54\%$ (stat.) for incoming monochromatic neutrons of 2.5 Å. This value is in agreement with the MC simulation, which predicted an efficiency of 53.47%.

Thickness variations in the boron coating of up to 13% along the aluminium blades were measured with thin-film characterisation techniques. This result was further confirmed by neutrography, The thickness gradient produced an efficiency variation of $\Delta_{uni} = \pm$ 1% along each grid. By correctly orienting these blades, an improvement was achieved. These results prove that potential constraints regarding the coating uniformity can be overcome.

γ-sensitivity tests were performed for a broad range of energies (from tens of keV to a few MeV). The result obtained at the same gain value as for neutron detection efficiency measurements was $\epsilon_\gamma \leq 5 \cdot 10^{-5}$.

Long-term stability has been pointed out as one of the most important requirements for the detector of a ToF instrument. Two different types of gas species were tested: CF_4 and Ar-CO_2. The Multi-Grid detector was under a moderated neutron flux over a long period of time. Small variations in the gain (measured by the shift of the PHS towards lower energies) were observed. For the moderated neutron rate used, CF_4 shows a better stability than Ar-CO_2.

If the neutron flux is further increased the loss in the detector gain becomes critical. In this sense, a clear difference in the performance of the two gas species is found. For a similar neutron flux, CF_4 shows a decrease in gain of $\approx$ 80% whilst in the case of Ar-CO_2 it only drops by 10%.

The relatively high efficiency found, together with the high uniformity over large areas, demonstrate the potential of this technique as alternative to ^{3}He-based PSDs in NSS.

Bibliography

[1] K. Zeitelhack. Search for alternative techniques to Helium-3 based detectors for neutron scattering applications. *Neutron News*, 23(4), 2012.

[2] H. Mutka J. Ollivier and L. Didier. The new cold neutron time-of-flight spectrometer IN5. *Neutron News*, 21(2), 2010.

[3] ILL patent application EP 1320119.

[4] A. J. Dianoux and G. Lander. Neutron Data Booklet, 2003.

[5] T. Brückel et al. *Laboratory Course in Neutron Scattering*. Forschungszentrum Jülich GmbH, 2007.

[6] Conceptual design report. Technical report, ESS, 2012.

[7] D. A. Shea and D. Morgan. The Helium-3 shortage: Supply, demand, and options for congress. Technical Report R41419, Congressional Research Service, 2010.

[8] GAO. Neutron detectors: an alternative to using Helium-3. Technical Report 11-753, US Government Accountability Office, 2011.

[9] A. Cho. Helium-3 shortage could put freeze on low-temperature research. *Science*, 326(5954), 2009.

[10] RT. Kouzes. The ^{3}He supply problem. Technical Report 18388, PNNL, 2009.

[11] P. Convert and J. B. Forsyth. *Position Sensitive Detection of Thermal Neutrons*. Academic Press., 1983.

[12] T. Wilpert. Boron Triflouride Detectors. *Neutron News*, 23(4), 2012.

[13] N. G. Rhodes. Scintillation Detectors. *Neutron News*, 23(4), 2012.

[14] T. Nakamura et al. A large-area two-dimensional scintillator detector with a wavelength-shifting fibre readout for a time-of-flight single-crystal neutron diffractometer. *Nucl. Instrum. and Methods A*, 686(0), 2012.

[15] J. Pancin et al. Piccolo Micromegas: First in-core measurements in a nuclear reactor. *Nucl. Instrum. Meth. A*, 592(1–2), 2008.

[16] J.C. Buffet et al. Advances in detectors for single crystal neutron diffraction. *Nucl. Instrum. and Meth. A*, 554(1–3), 2005.

[17] J.L. Lacy et al. Novel neutron detector for high rate imaging applications. In *Nuclear Science Symposium Conference Record, 2002. IEEE*, volume 1, 2002.

[18] A. Athanasiades et al. Straw detector for high rate, high resolution neutron imaging. In *Nuclear Science Symposium Conference Record, 2005. IEEE*, volume 2, 2005.

[19] ANSI - American National Standard Institute. Evaluation and Performance of Radiation Detection Portal Monitors for Use in Homeland Security . Technical report, ANSI, 2004.

[20] CRISP European Project. http://www.crisp-fp7.eu/.

[21] S. Masaoka et al. Optimization of a micro-strip gas chamber as a two-dimensional neutron detector using gadolinium converter. *Nucl. Instrum. Meth. A*, 513(3), 2003.

[22] M. Calviani et al. A fast ionization chamber for fission cross-section measurements at n-TOF. *Nucl. Instrum. Meth. A*, 594(2), 2008.

[23] D. S. McGregor et al. Micro-pocket fission detectors (mpfd) for in-core neutron flux monitoring. *Nucl. Instrum. Meth. A*, 554(1–3), 2005.

[24] M Tardocchi et al. Cadmium–Zinc–Telluride photon detector for epithermal neutron spectroscopy - pulse height response characterisation. *Nucl. Instrum. Meth. A*, 526(3), 2004.

[25] M. Herman. NNDC - SIGMA: Evaluated Nuclear Data File (ENDF).

[26] G. F. Knoll. *Radiation Detection and Measurement*. John Wiley and Sons, Inc., 1999.

[27] J. Ziegler. SRIM - Stopping Range of Ions in Matter.

[28] M.J. Berger et al. NIST - XCOM: Photon Cross Sections Database.

[29] M.J. Berger et al. NIST - ESTAR: Stopping Powers and Range for Electrons.

[30] F. Sauli. *Principles of Operation of Multi-wire Proportional and Drift Chambers*. 1977.

[31] R. Santonico and R. Cardarelli. Development of resistive plate counters. *Nucl. Instrum. Meth. A*, 187(2–3), 1981.

[32] A. Bolozdynya et al. Detection of thermal neutrons in cylindrical ionization chamber filled with high-pressure Xe+3He gas mixture. *Nucl. Instrum. Meth. A*, 522(3), 2004.

[33] A. Morozov et al. Effect of the electric field on the primary scintillation from CF4. *Nucl. Instrum. Meth. A*, 628(1), 2011.

[34] R. Veenhof. Garfield - Simulation of Gaseous Detectors.

[35] W. Shockley. Currents to conductors induced by a moving point charge. *J. Appl. Phys.*, 9(10), 1938.

[36] S. Ramo. Currents induced by electron motion. *Proceedings of the IRE*, 27(9), 1939.

[37] S. Chabod et al. Modelling of fission chambers in current mode—analytical approach. *Nucl. Instrum. Meth. A*, 566(2), 2006.

[38] J.K. Shultis and D.S. McGregor. Design and performance considerations for perforated semiconductor thermal-neutron detectors. *Nucl. Instrum. Meth. A*, 606(3), 2009.

[39] K. A. Nelson et al. Investigation of a lithium foil multi-wire proportional counter for potential ^{3}He replacement. *Nucl. Instrum. Meth. A*, 669(0), 2012.

[40] ILL patent application FR 10/51502.

[41] Y. Blanc. Le spectrometre a temps de vol IN6, characteristiques, techniques at performances. Technical report, ILL, 1986.

[42] O. Knotek, E. Lugscheider, and C.W. Siry. Tribological properties of B-C thin films deposited by magnetron-sputter-ion plating method. *Surface and Coatings Technology*, 91(3), 1997.

[43] Ali O. Sezer and J.I. Brand. Chemical vapor deposition of boron carbide. *Materials Science and Engineering: B*, 79(3), 2001.

[44] E. Pascual et al. Boron carbide thin films deposited by tuned-substrate RF magnetron sputtering. *Diamond and Related Materials*, 8(2–5), 1999.

[45] C. Höglund. *Growth and Phase Stability Studies of Epitaxial Sc-Al-N and Ti-Al-N Thin Films.* PhD thesis, Thin Film Physics Division - IFM - Linköping University, 2010.

[46] M.U Guruz, V.P Dravid, and Y.W Chung. Synthesis and characterization of single and multilayer boron nitride and boron carbide thin films grown by magnetron sputtering of boron carbide. *Thin Solid Films*, 414(1), 2002.

[47] A. Lousa et al. Effect of ion bombardment on the properties of B4C thin films deposited by RF sputtering. *Thin Solid Films*, 355–356(0), 1999.

[48] M.J. Zhou et al. Microstructure and mechanical properties of B4C films deposited by ion beam sputtering. *Thin Solid Films*, 516(2–4), 2007.

[49] C. Höglund et al. B_4C thin films for neutron detection. *J. Appl. Phys.*, 111(104908), 2012.

[50] A. Sonzogni et al. NNDC - BNL: National Nuclear Data Center.